Contributions of Distinct Interneuron Types to Neocortical Dynamics

by

Ulf Knoblich

Dipl.-Inform., Saarland University, 2004

Submitted to the Department of Brain & Cognitive Sciences
in Partial Fulfillment of the Requirements for the Degree of

DOCTOR OF PHILOSOPHY IN NEUROSCIENCE
AT THE
MASSACHUSETTS INSTITUTE OF TECHNOLOGY

FEBRUARY 2011

Author . . . . . .
Department of Brain & Cognitive Sciences
December 7, 2010

Certified by . . . . . .
Christopher I. Moore
Associate Professor of Neuroscience
Thesis Supervisor

Accepted by . . . . . .
Earl K. Miller
Picower Professor of Neuroscience
Director, BCS Graduate Program

Contributions of Distinct Interneuron Types to Neocortical Dynamics

by

Ulf Knoblich

Submitted to the Department of Brain & Cognitive Sciences
on December 7, 2010 in Partial Fulfillment of the Requirements
for the Degree of Doctor of Philosophy in Neuroscience

ABSTRACT

Inhibitory interneurons are thought to play a crucial role in several features of neocortical processing, including dynamics on the timescale of milliseconds. Their anatomical and physiological characteristics are diverse, suggesting that different types regulate distinct aspects of neocortical dynamics. Interneurons expressing parvalbumin (PV) and somatostatin (SOM) form two non-overlapping populations. Here, I describe computational, correlational (neurophysiological) and causal (optogenetic) studies testing the role of PV and SOM neurons in dynamic regulation of sensory processing.

First, by combining extra- and intracellular recordings with optogenetic and sensory stimulation and pharmacology, we have shown that PV cells play a key role in the generation of neocortical gamma oscillations, confirming the predictions of prior theoretical and correlative studies. Following this experimental study, we used a biophysically plausible model, simulating thousands of neurons, to explore mechanisms by which these gamma oscillations shape sensory responses, and how such transformations impact signal relay to downstream neocortical areas. We found that the local increase in spike synchrony of sensory-driven responses, which occurs without decreasing spike rate, can be explained by pre- and post-stimulus inhibition acting on pyramidal and PV cells. This transformation led to increased activity downstream, constituting an increase in gain between the two regions. This putative benefit of PV-mediated inhibition for signal transmission is only realized if the strength and timing of inhibition in the downstream area is matched to the upstream source.

Second, we tested the hypothesis that SOM cells impact a distinct form of dynamics, sensory adaptation, using intracellular recordings, optogenetics and sensory stimulation. In resting neocortex, we found that SOM cell activation generated inhibition in pyramidal neurons that matched that seen in *in vitro* studies. Optical SOM cell activation also transformed sensory-driven responses, decreasing evoked activity. In adapted responses, optical SOM cell inactivation relieved the impact of sustained sensory input, leading to increased membrane potential and spike rate. In contrast, SOM cell inactivation had minimal impact on sensory responses in a non-adapted neocortex, supporting the prediction that this class of interneurons is only recruited when the network is in an activated state. These findings present a previously unappreciated mechanism controlling sensory adaptation.

Thesis Supervisor: Christopher I. Moore

Title: Associate Professor of Neuroscience

Acknowledgments

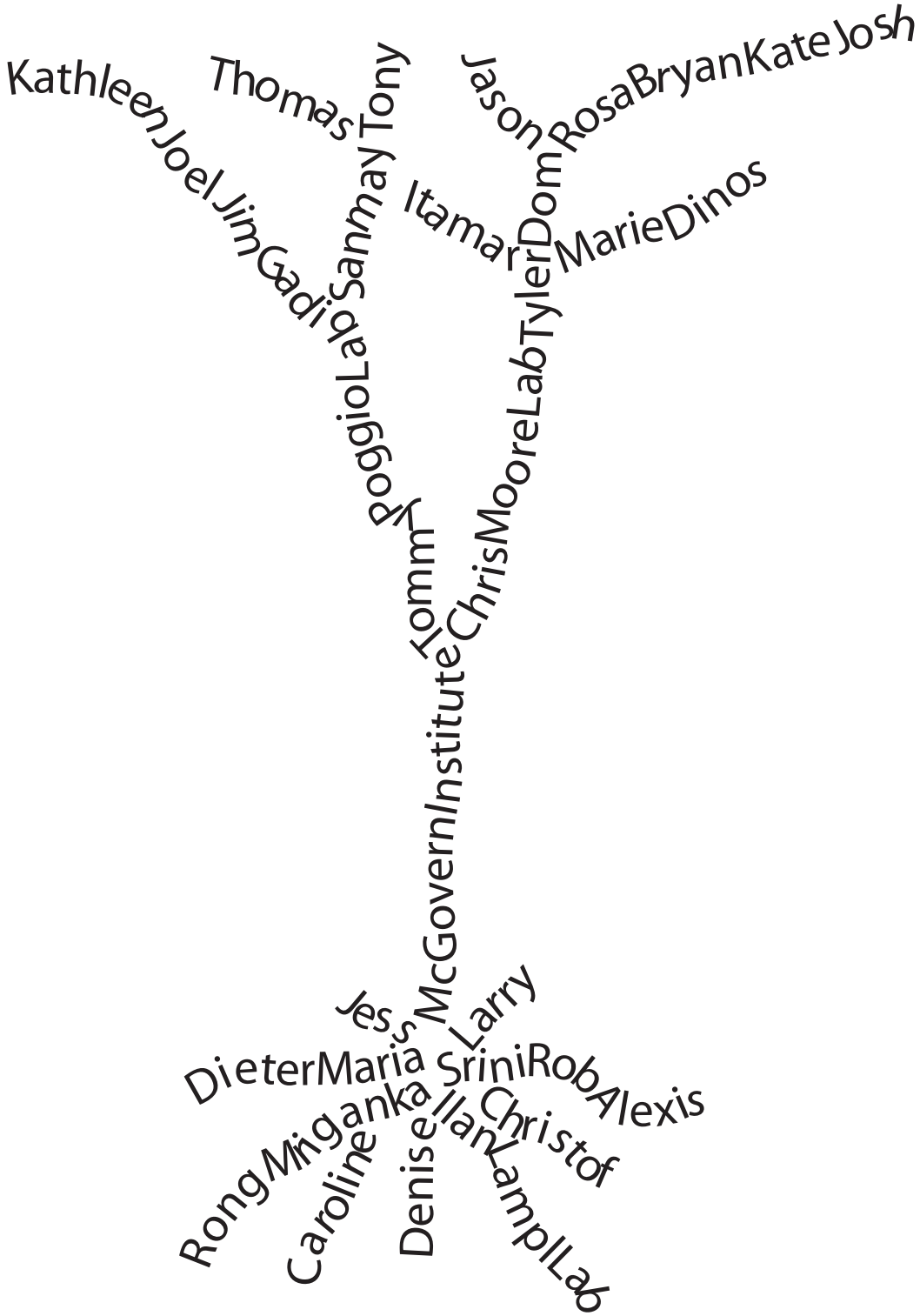

Table of Contents

Preface

Unifying the Dichotomy: Of Models and Experiments

Most neuroscientists can unambiguously identify as either theorists or experimentalists. My world is not that simple. While training in computer science my specialization was artificial intelligence, so studying natural intelligence on a computational level seemed to be a natural next step. Soon I realized that most conclusions in computational neuroscience suffer from a high level of conditionality. Results from modeling studies, no matter how sophisticated, can only tell us how the brain *could* work if all the assumptions are correct, not how it actually *does*. In other words, the outcome of these studies might more appropriately be called predictions rather than conclusions. Computational modeling does not work in a proverbial vacuum, in fact it is highly dependent on experimental data in at least two ways. First, models need to be constrained by data to provide a set of basic assumptions and limit the space of possible models. A model that does not capture the relevant aspects of the available data on a particular phenomenon in systems neuroscience is unlikely to provide any insight into the underlying neural mechanisms. Second, model predictions need to be tested experimentally to evaluate whether the model assumptions were correct, ideally converting a possibility into an assertion. The data collected in the new experiment will provide further constraints for the next version of the model and start a new iteration of this cycle of scientific progress. Since models are that depend on experiments, one could ask why we need any computational models, at all. The wealth and complexity of experimental data available today has grown far beyond what can be captured with simple mental models. Computational simulations provide the possibility of integrating a wide range of information at different levels, from channel biophysics to behavioral states, and require rigorous quantification. An important result of this need for specification is guaranteed internal consistency. Many mental “box and arrow” models sound very reasonable, but the lack of explicit quantification makes them more vulnerable to inconsistencies that are difficult to detect on a qualitative level. As Tommy Poggio pointed out to me, all models are wrong. They key is to know what about them is wrong and which are less wrong than others, and experiments are the only way to determine that. This document describes some of my attempts to complete the cycle of progress and bridge the divide between computational and experimental neuroscience.

Chapter 1:

Introduction

1.1 Neocortical Dynamics

Perception, action, and cognition in higher vertebrates all depend crucially on the neocortex. Reflecting these various behavioral demands, neocortical neurons are selective for many different kinds of features and stimuli. Sensory neocortical neurons, for example, can respond preferentially to a specific face, to a specific auditory tone, or to taps on a fingertip. This tuning is robust across a variety of stimulus conditions. The same neuron can respond to the same face presented as a line drawing or in a naturalistic form (Tsao et al., 2006). This sustainability of tuning is believed to be a key to perceptual constancy. We can recognize our grandmother on a rainy day in Illinois, on a sunny day in Arizona, and in a faded grainy photograph.

Neocortical neurons also demonstrate modulation of their sensitivity on the timescale of milliseconds to seconds. These dynamics can be driven by external or internal changes in context. A classic example is the adaptation generated by recurring sensory stimulation. The same neuron gives a much smaller response to the repeated presentation of a stimulus, compared with the initial presentation that occurred only milliseconds earlier. Neuronal sensitivity may also shift to reflect internal changes. For example, during tasks that require focused attention, neurons can show an enhanced response to the attended stimulus. This flexibility of neocortical circuits is thought to underlie our ability to adjust and process information optimally under a wide variety of situations. To attain such flexibility, it seems likely that a variety of processes operating on different time scales is needed. Learning, probably mediated by long-term synaptic plasticity, is a good candidate for changes occurring on the order of minutes and longer, up to years. However, even faster processes exhibit different time scales from milliseconds to seconds.

1.2 Interneuron Diversity

While inhibitory interneurons only comprise approximately 20% of all neurons in neocortex, their morphological, molecular and physiological characteristics are far more diverse than those of the prevalent excitatory (pyramidal and stellate) cells (Cauli et al., 1997; Markram et al., 2004; Burkhalter, 2008), leading to the conjecture that they are more likely to mediate the rich functional diversity found in higher vertebrates (Moore et al., 2010).

Several features have been identified for each of these properties of interneurons, and in most cases there does not seem to be any simple one-to-one mapping between them, making it difficult to find an objective and general framework to identify distinct types of interneurons

(Ascoli et al., 2008). This heterogeneity complicates the ongoing effort to elucidate the functional role of these different interneuron types, in particular because it is difficult to compare and integrate studies using different features for their classification. The predominant method for functional studies has been electrophysiology, and thus it is not surprising that the classification used in these studies was most often based on the spiking pattern of the neurons under investigation. However, with the advent of optogenetics and the growing repertoire of transgenic mouse lines, molecular features have been increasingly used in functional studies utilizing electrophysiology, two-photon imaging or a combination thereof (Cardin et al., 2009; hua Liu et al., 2009).

The molecular markers most commonly used for classification are the calcium-binding proteins calbindin, calretinin and parvalbumin (PV) as well as the neuropeptides cholecystokinin, neuropeptide Y, somatostatin (SOM) and vasoactive intestinal peptide, and most interneurons express more than one of these markers. However, PV and SOM containing cells seem to be two non-overlapping populations across species (Gonchar et al., 2007; Xu et al., 2010), a classification which is supported by other morphological and physiological properties. Most PV containing cells are morphologically classified as basket or chandelier cells and make strong synapses mostly on the soma and axon hillock of their target neurons, while SOM interneurons tend to innervate the dendrites. In addition, most PV cells are characterized as “fast spiking”, in contrast to “regular spiking” pyramidal cells and “low-threshold spiking” SOM interneurons. All these differences seem to point to a network architecture in which soma-targeting PV neurons with their strong peri-somatic synapses preferentially act on the output of a neuron, influencing the generation of a spike and modulating its precise timing, whereas dendrite-targeting non-PV interneurons including SOM cells provide more subtle inhibition on its inputs before they are integrated at the soma, shaping the spatiotemporal integration of multiple post-synaptic potentials in the dendrites.

Neurons containing PV are by far the most numerous, accounting for approximately 40% of GABAergic interneurons in mouse neocortex, followed by neurons expressing SOM or CR with 10-15% each (Xu et al., 2010), making these populations an obvious first choice for the investigation of the functional role of different subtypes of interneurons.

1.3 Parvalbumin-positive interneurons

In part due to their relative abundance and the ability to (putatively) identify fast-spiking neurons based on extracellular spike shape, PV expressing interneurons are the most studied interneuron type. One widely occurring cortical motif featuring these fast-spiking PV interneurons is disynaptic feed-forward inhibition: The incoming axons of excitatory cells synapse onto excitatory and inhibitory cells in a given target area, and the inhibitory cells provide inhibition to the excitatory cells (Swadlow, 2003; Gabernet et al., 2005; Inoue and Imoto, 2006). In this architecture, inputs to an area will elicit excitatory and inhibitory post-synaptic potentials. This parity in sensory drive is a key determinant in generating balanced excitation and inhibition in the neocortex (Moore and Nelson, 1998; Wehr and Zador, 2003; Vogels and Abbott, 2009; Stimberg et al., 2009; Tan and Wehr, 2009; Sun et al., 2010). Because of their synaptic and cell-intrinsic properties, PV+ interneurons spike rapidly, usually before nearby pyramidal cells (Pouille et al., 2009), such that the inhibitory post-synaptic potential they trigger in the excitatory cells interferes with the EPSP, creating a narrow time window in which the cells can fire, often termed “window of integration” or “window of opportunity” (Pinto et al., 2000; Wehr and Zador, 2003; Hasenstaub et al., 2005; Wilent and Contreras, 2005).

PV cells also play an important role in another form of precise temporal gating, as they are crucial to the genesis and impact of oscillations in the gamma range (30-80 Hz). Studies performed *in vitro*, *in vivo*, and *in silico* point to a unifying mechanism for these oscillations: volleys of alternating inhibition and excitation between PV fast-spiking interneurons and pyramidal cells (Freeman, 1968; Wang and Buzsáki, 1996; Fisahn et al., 1998; Whittington et al., 2000; Traub et al., 2005; Bartos et al., 2007; Börgers et al., 2008; Börgers and Kopell, 2008; Atallah and Scanziani, 2009; Cardin et al., 2009; Paik et al., 2009)

Cortical oscillations in the gamma range have been observed in numerous brain regions in a variety of species (Gray and Singer, 1989; Engel et al., 1991; Ribary et al., 1991; Maldonado et al., 2000; Nase et al., 2003), and during a wide range of behavioral states, from attentive wakefulness to REM sleep (Maloney et al., 1997; Gruber et al., 1999). The appearance of gamma at specific times relative to task performance implicates these rhythms in sensory processing, perceptual binding, memory formation, and conscious experience (Tallon-Baudry et al., 1997; Tallon-Baudry and Bertrand, 1999; Fries et al., 2001; Womelsdorf et al., 2006; Jensen et al., 2007; Fries, 2009; Gregoriou et al., 2009). However, the correlation between gamma expression

and enhanced processing is nevertheless a debated issue, particularly in primary sensory neocortex (Chalk et al., 2010).

To move beyond assertions based in correlation and directly test the hypothesis that the precise spike timing brought about by gamma oscillations enhances intracortical communication, it is necessary to bring this oscillation under experimental control. Enforcing temporal precision within a local network will require interventions that are somewhat artificial, but which are essential for understanding the benefits of gamma. In a recent study, we used optical stimulation to drive PV neurons in the gamma frequency range, inducing network effects that mimic physiological gamma. When punctate sensory stimuli (brief vibrissa deflections) were presented, the precise timing of inhibition relative to sensory input altered the evoked neural response. For certain delays, the overall number of spikes was reduced, indicating gamma can change the input gain of a region. For other delays, rhythmic inhibition did not decrease the total number of spikes, but did cause spiking to occur in a more compressed temporal window, increasing the synchrony of the evoked response, in alignment with several previous experimental and computational studies reporting similar effects under conditions of natural, intrinsically generated gamma oscillations *in vitro*, *in vivo* and *in silico* (Burchell et al., 1998; Pouille and Scanziani, 2001; Fries et al., 2001; Börgers et al., 2005; Womelsdorf et al., 2006; Fries et al., 2008).

The computational benefit of gamma has been described as synchronizing spikes within a local population without changing the overall number of spikes, effectively creating a sequence of impactful spike packets interspersed with brief periods of relative silence, in contrast to a continuous stream of spikes without temporal structure. This view implies that each gamma cycle might be viewed as a separate “window of opportunity”, similar to the mechanisms controlling the transient imbalance of excitation and inhibition in response to a brief sensory stimulus. Mechanistic explanations of gamma-related redistribution of spikes have focused on the effect of the rhythmic inhibitory post-synaptic potentials in pyramidal cells suppressing spikes or delaying spiking in response to a sustained stimulus, leading to a compression of spike times into a shorter window and thus increased synchrony (Whittington et al., 2000; Börgers and Kopell, 2003; Tiesinga and Sejnowski, 2009).

In considering dynamics in rate coding, a fundamental question is the value that an action potential (or a fixed number of action potentials) has in generating firing in a downstream area.

Central to this question of gain modulation is whether the same number of spikes in a local area can generate a greater number of spikes in a target area, enhancing the *efficacy* of signal transmission. Synchrony is often cited as a potential mechanism for increasing the value of a given spike rate in a local area (König et al., 1996; Azouz and Gray, 2000; Pinto et al., 2000; Azouz and Gray, 2003; Börgers and Kopell, 2005; Bruno and Sakmann, 2006; Wang et al., 2010), though relatively little direct experimental evidence has been offered for this idea. Taking into account the correlation between attention and gamma band activity (Fries et al., 2001; Börgers et al., 2005; Womelsdorf et al., 2006; Roy et al., 2007; Börgers et al., 2008; Fries et al., 2008), these findings support the view that attention might act by increasing synchrony among local ensembles of neurons and thus selectively enhancing their impact on a target area, effectively increasing signal-to-noise without large increases in average spike rate (Steinmetz et al., 2000; Fries et al., 2001; Buia and Tiesinga, 2006; Fries et al., 2008).

Presuming efficacy can be modulated, we can begin to explore the boundaries on this improvement in transmission. For example, it is important to know the limit beyond which firing in the local area cannot be further optimized, leading to diminishing returns when more local spikes are added. We refer to this as the *efficiency* of transmission, as additional, less useful spikes would reflect "wasted" effort of the pre-synaptic area.

1.4 Somatostatin-positive interneurons

Interneurons expressing SOM are found throughout layers 2-6 in rat, mouse and primate neocortex (Hendry et al., 1984; Melchitzky and Lewis, 2008; Xu et al., 2010) and preferentially target dendrites of non-GABAergic cells (Kawaguchi and Kubota, 1998; Melchitzky and Lewis, 2008). Despite these commonalities, however, SOM+ interneurons form a more heterogeneous group than PV+ cells. In rat cerebral neocortex there is no overlap between CR, PV and SOM expressing neurons (Kubota et al., 1994; Gonchar and Burkhalter, 1997; Kawaguchi and Kubota, 1997), however there is considerable overlap between SOM and CR populations in mouse neocortex, and in addition a subset of SOM+ neurons expresses calbindin or CR, while others do not (Cauli et al., 1997; Halabisky et al., 2006; Ma et al., 2006; Xu et al., 2006; Gonchar et al., 2007; Xu et al., 2010).

In terms of physiological features, there is converging evidence that the populations of low-threshold spiking (LTS) cells and SOM cells are highly overlapping (Kawaguchi and Kubota,

1996; Reyes et al., 1998; Gibson et al., 1999; Amitai et al., 2002; Beierlein et al., 2003; Ma et al., 2006). LTS interneurons in layer 4 display distinct activation dynamics in comparison to fast-spiking PV cells. While synapses from regular spiking excitatory cells onto fast-spiking interneurons undergo short-term synaptic depression in response to incoming spike trains, synapses onto LTS cells show strong short-term facilitation (Beierlein et al., 2003). This finding has been replicated using thalamocortical stimulation, leading to the proposal that while PV cells are the main source of inhibition early during a sensory response, this balance shifts over time due to the different synaptic short-term dynamics and LTS/SOM cells provide the majority of late inhibition (Tan et al., 2008; Moore et al., 2010). In addition, a similar circuit has been identified in hippocampus, also involving SOM cells, in this case oriens-lacunosum-molecolare interneurons, and PV cells (Pouille and Scanziani, 2004).

Morphologically, a subset of SOM cells have a main axon ascending towards and ramifying in layer 1 characteristic of Martinotti cells (Kawaguchi and Kubota, 1996; McGarry et al., 2010). Further, it has been found that all Martinotti cells express SOM (Wang et al., 2004). Functionally, SOM Martinotti cells have been shown to mediate a phenomenon termed frequency-dependent disynaptic inhibition (FDDI) between pyramidal cells in layers 2/3 (Silberberg and Markram, 2007) as well as layer 5 (Kapfer et al., 2007). Activating a single pyramidal cell at high frequencies activates Martinotti cells, which in turn inhibit other pyramidal cells (and often the activated cell, as well), and this disynaptic inhibition increases supra-linearly with the number of activated pyramidal cells. It was also found that the probability of observing this disynaptic inhibition between two pyramidal cells was twice as high as the probability of a monosynaptic excitatory connection (Kapfer et al., 2007), indicating a net divergence of inhibition (Silberberg and Markram, 2007). While these initial reports were based on recordings in primary somatosensory cortex in rats, recently FDDI has also been shown to occur in a variety of other cortical areas including primary motor cortex, secondary visual cortex, primary auditory cortex and medial prefrontal cortex of the rat (Berger et al., 2009).

Using calcium imaging of apical dendrites of layer 5 pyramidal neurons in combination with pharmacology targeted to either upper or deep layers, it has been shown that disrupting synaptic transmission in layer 5 increased the calcium signal in superficial dendrites in response to hind limb stimulations. In addition, blocking GABAergic synaptic transmission near the cortical surface drastically increased responses (Murayama et al., 2009). From these manipulations, the

authors inferred that the inhibition they observed was most likely mediated by layer 5 Martinotti cells. However, this hypothesis has not directly been tested.

1.5 Outline

In the following chapters, I describe correlational (neurophysiological), causal (optogenetic) and computational studies testing the role of PV and SOM neurons in dynamic regulation of sensory processing.

In chapter 2 I present a study I contributed to, in which, by combining extra- and intracellular recordings with optogenetic and sensory stimulation and pharmacology, we have shown that PV cells play a key role in the generation of neocortical gamma oscillations, confirming the predictions of prior theoretical and correlative studies. We have also investigated the impact of an ongoing gamma oscillation on a punctuate sensory stimulus, providing new data towards the impact of gamma on sensory processing.

Following this experimental study, we used a biophysically plausible model, simulating thousands of neurons, to explore mechanisms by which these gamma oscillations shape sensory responses, and how such transformations impact signal relay to downstream neocortical areas, which is described in chapter 3.

In chapter 4, we tested the hypothesis that SOM cells impact a distinct form of dynamics, sensory adaptation, using intracellular recordings, optogenetics and sensory stimulation. Even though the role of interneurons in sensory adaptation has thus far largely been dismissed, *in vitro* studies have shown that SOM cells are well positioned to contribute to this phenomenon. Our findings confirm the previous findings *in vivo* and present a previously unappreciated mechanism for controlling sensory adaptation.

1.6 References

Amitai, Y., Gibson, J. R., Beierlein, M., Patrick, S. L., Ho, A. M., Connors, B. W., Golomb, D., 2002. The spatial dimensions of electrically coupled networks of interneurons in the neocortex. J. Neurosci. 22 (10), 4142–4152.

Ascoli, G. A., Alonso-Nanclares, L., Anderson, S. A., Barrionuevo, G., Benavides-Piccione, R., Burkhalter, A., Buzsáki, G., Cauli, B., DeFelipe, J., Fairén, A., Feldmeyer, D., Fishell, G., Frégnac, Y., Freund, T. F., Gardner, D., Gardner, E. P., Goldberg, J. H., Helmstaedter, M., Hestrin, S., Karube, F., Kisvárday, Z. F., Lambolez, B., Lewis, D. A., Marin, O., Markram, H., Muñoz, A., Packer, A. M., Petersen, C. C. H., Rockland, K. S., Rossier, J., Rudy, B., Somogyi,

P., 2008. Petilla terminology: nomenclature of features of GABAergic interneurons of the cerebral cortex. Nat. Rev. Neurosci. 9 (7), 557–568.

Atallah, B. V., Scanziani, M., 2009. Instantaneous modulation of gamma oscillation frequency by balancing excitation with inhibition. Neuron 62 (4), 566–577.

Azouz, R., Gray, C. M., 2000. Dynamic spike threshold reveals a mechanism for synaptic coincidence detection in cortical neurons in vivo. Proc. Natl. Acad. Sci. U.S.A. 97 (14), 8110–8115.

Azouz, R., Gray, C. M., 2003. Adaptive coincidence detection and dynamic gain control in visual cortical neurons in vivo. Neuron 37 (3), 513–523.

Börgers, C., Epstein, S., Kopell, N. J., 2005. Background gamma rhythmicity and attention in cortical local circuits: a computational study. Proc. Natl. Acad. Sci. U.S.A. 102 (19), 7002–7007.

Börgers, C., Epstein, S., Kopell, N. J., 2008. Gamma oscillations mediate stimulus competition and attentional selection in a cortical network model. Proc. Natl. Acad. Sci. U.S.A. 105 (46), 18023–18028.

Börgers, C., Kopell, N. J., 2003. Synchronization in networks of excitatory and inhibitory neurons with sparse, random connectivity. Neural Comput. 15 (3), 509–538.

Börgers, C., Kopell, N. J., 2005. Effects of noisy drive on rhythms in networks of excitatory and inhibitory neurons. Neural Comput. 17 (3), 557–608.

Börgers, C., Kopell, N. J., 2008. Gamma oscillations and stimulus selection. Neural Comput. 20 (2), 383–414.

Bartos, M., Vida, I., Jonas, P., 2007. Synaptic mechanisms of synchronized gamma oscillations in inhibitory interneuron networks. Nat. Rev. Neurosci. 8 (1), 45–56.

Beierlein, M., Gibson, J. R., Connors, B. W., 2003. Two dynamically distinct inhibitory networks in layer 4 of the neocortex. J. Neurophysiol. 90 (5), 2987–3000.

Berger, T. K., Perin, R., Silberberg, G., Markram, H., 2009. Frequency-dependent disynaptic inhibition in the pyramidal network: a ubiquitous pathway in the developing rat neocortex. J. Physiol. (Lond.) 587 (22), 5411–5425.

Bruno, R. M., Sakmann, B., 2006. Cortex is driven by weak but synchronously active thalamocortical synapses. Science 312 (5780), 1622–1627.

Buia, C. I., Tiesinga, P. H., 2006. Attentional modulation of firing rate and synchrony in a model cortical network. J. Comput. Neurosci. 20 (3), 247–264.

Burchell, T. R., Faulkner, H. J., Whittington, M. A., 1998. Gamma frequency oscillations gate temporally coded afferent inputs in the rat hippocampal slice. Neurosci. Lett. 255 (3), 151–154.

Burkhalter, A., 2008. Many specialists for suppressing cortical excitation. Front Neurosci. 2 (2), 155–167.

Cardin, J. A., Carlén, M., Meletis, K., Knoblich, U., Zhang, F., Deisseroth, K., Tsai, L.-H., Moore, C. I., 2009. Driving fast-spiking cells induces gamma rhythm and controls sensory responses. Nature 459 (7247), 663–667.

Cauli, B., Audinat, E., Lambolez, B., Angulo, M. C., Ropert, N., Tsuzuki, K., Hestrin, S., Rossier, J., 1997. Molecular and physiological diversity of cortical nonpyramidal cells. J. Neurosci. 17 (10), 3894–3906.

Chalk, M., Herrero, J. L., Gieselmann, M. A., Delicato, L. S., Gotthardt, S., Thiele, A., 2010. Attention reduces stimulus-driven gamma frequency oscillations and spike field coherence in V1. Neuron 66 (1), 114–125.

Engel, A. K., König, P., Kreiter, A. K., Singer, W., 1991. Interhemispheric synchronization of oscillatory neuronal responses in cat visual cortex. Science 252 (5010), 1177–1179.

Fisahn, A., Pike, F. G., Buhl, E. H., Paulsen, O., 1998. Cholinergic induction of network oscillations at 40 Hz in the hippocampus in vitro. Nature 394 (6689), 186–189.

Freeman, W. J., 1968. Relations between unit activity and evoked potentials in prepyriform cortex of cats. J. Neurophysiol. 31 (3), 337–348.

Fries, P., 2009. Neuronal gamma-band synchronization as a fundamental process in cortical computation. Annu. Rev. Neurosci. 32, 209–224.

Fries, P., Reynolds, J. H., Rorie, A. E., Desimone, R., 2001. Modulation of oscillatory neuronal synchronization by selective visual attention. Science 291 (5508), 1560–1563.

Fries, P., Womelsdorf, T., Oostenveld, R., Desimone, R., 2008. The effects of visual stimulation and selective visual attention on rhythmic neuronal synchronization in macaque area V4. J. Neurosci. 28 (18), 4823–4835.

Gabernet, L., Jadhav, S. P., Feldman, D. E., Carandini, M., Scanziani, M., 2005. Somatosensory integration controlled by dynamic thalamocortical feed-forward inhibition. Neuron 48 (2), 315–327.

Gibson, J. R., Beierlein, M., Connors, B. W., 1999. Two networks of electrically coupled inhibitory neurons in neocortex. Nature 402 (6757), 75–79.

Gonchar, Y., Burkhalter, A., 1997. Three distinct families of GABAergic neurons in rat visual cortex. Cereb. Cortex 7 (4), 347–358.

Gonchar, Y., Wang, Q., Burkhalter, A., 2007. Multiple distinct subtypes of GABAergic neurons in mouse visual cortex identified by triple immunostaining. Front. Neuroanat. 1.

Gray, C. M., Singer, W., 1989. Stimulus-specific neuronal oscillations in orientation columns of cat visual cortex. Proc. Natl. Acad. Sci. U.S.A. 86 (5), 1698–1702.

Gregoriou, G. G., Gotts, S. J., Zhou, H.-H., Desimone, R., 2009. High-frequency, long-range coupling between prefrontal and visual cortex during attention. Science 324 (5931), 1207–1210.

Gruber, T., Müller, M. M., Keil, A., Elbert, T., 1999. Selective visual-spatial attention alters induced gamma band responses in the human EEG. Clin Neurophysiol 110 (12), 2074–2085.

Halabisky, B., Shen, F., Huguenard, J. R., Prince, D. A., 2006. Electrophysiological classification of somatostatin-positive interneurons in mouse sensorimotor cortex. J. Neurophysiol. 96 (2), 834–845.

Hasenstaub, A. R., Shu, Y., Haider, B., Kraushaar, U., Duque, A., McCormick, D. A., 2005. Inhibitory postsynaptic potentials carry synchronized frequency information in active cortical networks. Neuron 47 (3), 423–435.

Hendry, S. H., Jones, E. G., Emson, P. C., 1984. Morphology, distribution, and synaptic relations of somatostatin- and neuropeptide Y-immunoreactive neurons in rat and monkey neocortex. J. Neurosci. 4 (10), 2497–2517.

hua Liu, B., Li, P., tang Li, Y., Sun, Y. J., Yanagawa, Y., Obata, K., Zhang, L. I., Tao, H. W., 2009. Visual receptive field structure of cortical inhibitory neurons revealed by two-photon imaging guided recording. J. Neurosci. 29 (34), 10520–10532.

Inoue, T., Imoto, K., 2006. Feedforward inhibitory connections from multiple thalamic cells to multiple regular-spiking cells in layer 4 of the somatosensory cortex. J. Neurophysiol. 96 (4), 1746–1754.

Jensen, O., Kaiser, J., Lachaux, J.-P., 2007. Human gamma-frequency oscillations associated with attention and memory. Trends Neurosci. 30 (7), 317–324.

König, P., Engel, A. K., Singer, W., 1996. Integrator or coincidence detector? The role of the cortical neuron revisited. Trends Neurosci. 19 (4), 130–137.

Kapfer, C., Glickfeld, L. L., Atallah, B. V., Scanziani, M., 2007. Supralinear increase of recurrent inhibition during sparse activity in the somatosensory cortex. Nat. Neurosci. 10 (6), 743–753.

Kawaguchi, Y., Kubota, Y., 1996. Physiological and morphological identification of somatostatin- or vasoactive intestinal polypeptide-containing cells among GABAergic cell subtypes in rat frontal cortex. J. Neurosci. 16 (8), 2701–2715.

Kawaguchi, Y., Kubota, Y., 1997. GABAergic cell subtypes and their synaptic connections in rat frontal cortex. Cereb. Cortex 7 (6), 476–486.

Kawaguchi, Y., Kubota, Y., 1998. Neurochemical features and synaptic connections of large physiologically-identified GABAergic cells in the rat frontal cortex. Neuroscience 85 (3), 677–701.

Kubota, Y., Hattori, R., Yui, Y., 1994. Three distinct subpopulations of GABAergic neurons in rat frontal agranular cortex. Brain Res. 649 (1), 159–173.

Ma, Y., Hu, H., Berrebi, A. S., Mathers, P. H., Agmon, A., 2006. Distinct subtypes of somatostatin-containing neocortical interneurons revealed in transgenic mice. J. Neurosci. 26 (19), 5069–5082.

Maldonado, P. E., Friedman-Hill, S., Gray, C. M., 2000. Dynamics of striate cortical activity in the alert macaque: II. Fast time scale synchronization. Cereb. Cortex 10 (11), 1117–1131.

Maloney, K. J., Cape, E. G., Gotman, J., Jones, B. E., 1997. High-frequency gamma electroencephalogram activity in association with sleep-wake states and spontaneous behaviors in the rat. Neuroscience 76 (2), 541–555.

Markram, H., Toledo-Rodriguez, M., Wang, Y., Gupta, A., Silberberg, G., Wu, C., 2004. Interneurons of the neocortical inhibitory system. Nat. Rev. Neurosci. 5 (10), 793–807.

McGarry, L. M., Packer, A. M., Fino, E., Nikolenko, V., Sippy, T., Yuste, R., 2010. Quantitative classification of somatostatin-positive neocortical interneurons identifies three interneuron subtypes. Front Neural Circuits 4.

Melchitzky, D. S., Lewis, D. A., 2008. Dendritic-targeting GABA neurons in monkey prefrontal cortex: comparison of somatostatin- and calretinin-immunoreactive axon terminals. Synapse 62 (6), 456–465.

Moore, C. I., Carlén, M., Knoblich, U., Cardin, J. A., 2010. Neocortical interneurons: from diversity, strength. Cell 142 (2), 189–193.

Moore, C. I., Nelson, S. B., 1998. Spatio-temporal subthreshold receptive fields in the vibrissa representation of rat primary somatosensory cortex. J. Neurophysiol. 80 (6), 2882–2892.

Murayama, M., Pérez-Garci, E., Nevian, T., Bock, T., Senn, W., Larkum, M. E., 2009. Dendritic encoding of sensory stimuli controlled by deep cortical interneurons. Nature 457 (7233), 1137–1141.

Nase, G., Singer, W., Monyer, H., Engel, A. K., 2003. Features of neuronal synchrony in mouse visual cortex. J. Neurophysiol. 90 (2), 1115–1123.

Paik, S.-B., Kumar, T., Glaser, D. A., 2009. Spontaneous local gamma oscillation selectively enhances neural network responsiveness. PLoS Comput. Biol. 5 (3).

Pinto, D. J., Brumberg, J. C., Simons, D. J., 2000. Circuit dynamics and coding strategies in rodent somatosensory cortex. J. Neurophysiol. 83 (3), 1158–1166.

Pouille, F., Marin-Burgin, A., Adesnik, H., Atallah, B. V., Scanziani, M., 2009. Input normalization by global feedforward inhibition expands cortical dynamic range. Nat. Neurosci. 12 (12), 1577–1585.

Pouille, F., Scanziani, M., 2001. Enforcement of temporal fidelity in pyramidal cells by somatic feed-forward inhibition. Science 293 (5532), 1159–1163.

Pouille, F., Scanziani, M., 2004. Routing of spike series by dynamic circuits in the hippocampus. Nature 429 (6993), 717–723.

Reyes, A. D., Lujan, R., Rozov, A., Burnashev, N., Somogyi, P., Sakmann, B., 1998. Target-cell-specific facilitation and depression in neocortical circuits. Nat. Neurosci. 1 (4), 279–285.

Ribary, U., Ioannides, A. A., Singh, K. D., Hasson, R., Bolton, J. P., Lado, F., Mogilner, A., Llinas, R. R., 1991. Magnetic field tomography of coherent thalamocortical 40-Hz oscillations in humans. Proc. Natl. Acad. Sci. U.S.A. 88 (24), 11037–11041.

Roy, A., Steinmetz, P. N., Hsiao, S. S., Johnson, K. O., Niebur, E., 2007. Synchrony: a neural correlate of somatosensory attention. J. Neurophysiol. 98 (3), 1645–1661.

Silberberg, G., Markram, H., 2007. Disynaptic inhibition between neocortical pyramidal cells mediated by Martinotti cells. Neuron 53 (5), 735–746.

Steinmetz, P. N., Roy, A., Fitzgerald, P. J., Hsiao, S. S., Johnson, K. O., Niebur, E., 2000. Attention modulates synchronized neuronal firing in primate somatosensory cortex. Nature 404 (6774), 187–190.

Stimberg, M., Wimmer, K., Martin, R., Schwabe, L., Mariño, J., Schummers, J., Lyon, D. C., Sur, M., Obermayer, K., 2009. The Operating Regime of Local Computations in Primary Visual Cortex. Cereb. Cortex.

Sun, Y. J., Wu, G. K., hua Liu, B., Li, P., Zhou, M., Xiao, Z., Tao, H. W., Zhang, L. I., 2010. Fine-tuning of pre-balanced excitation and inhibition during auditory cortical development. Nature 465 (7300), 927–931.

Swadlow, H. A., 2003. Fast-spike interneurons and feedforward inhibition in awake sensory neocortex. Cereb. Cortex 13 (1), 25–32.

Tallon-Baudry, C., Bertrand, O., 1999. Oscillatory gamma activity in humans and its role in object representation. Trends Cogn. Sci. (Regul. Ed.) 3 (4), 151–162.

Tallon-Baudry, C., Bertrand, O., Delpuech, C., Permier, J., 1997. Oscillatory gamma-band (30-70 Hz) activity induced by a visual search task in humans. J. Neurosci. 17 (2), 722–734.

Tan, A. Y. Y., Wehr, M., 2009. Balanced tone-evoked synaptic excitation and inhibition in mouse auditory cortex. Neuroscience 163 (4), 1302–1315.

Tan, Z., Hu, H., Huang, Z. J., Agmon, A., 2008. Robust but delayed thalamocortical activation of dendritic-targeting inhibitory interneurons. Proc. Natl. Acad. Sci. U.S.A. 105 (6), 2187–2192.

Tiesinga, P. H., Sejnowski, T. J., 2009. Cortical enlightenment: are attentional gamma oscillations driven by ING or PING. Neuron 63 (6), 727–732.

Traub, R. D., Contreras, D., Cunningham, M. O., Murray, H., LeBeau, F. E. N., Roopun, A. K., Bibbig, A., Wilent, W. B., Higley, M. J., Whittington, M. A., 2005. Single-column thalamocortical network model exhibiting gamma oscillations, sleep spindles, and epileptogenic bursts. J. Neurophysiol. 93 (4), 2194–2232.

Tsao, D. Y., Freiwald, W. A., Tootell, R. B. H., Livingstone, M. S., 2006. A cortical region consisting entirely of face-selective cells. Science 311 (5761), 670–674.

Vogels, T. P., Abbott, L. F., 2009. Gating multiple signals through detailed balance of excitation and inhibition in spiking networks. Nat. Neurosci. 12 (4), 483–491.

Wang, H.-P., Spencer, D., Fellous, J.-M., Sejnowski, T. J., 2010. Synchrony of thalamocortical inputs maximizes cortical reliability. Science 328 (5974), 106–109.

Wang, X.-J., Buzsáki, G., 1996. Gamma oscillation by synaptic inhibition in a hippocampal interneuronal network model. J. Neurosci. 16 (20), 6402–6413.

Wang, Y., Toledo-Rodriguez, M., Gupta, A., Wu, C., Silberberg, G., Luo, J., Markram, H., 2004. Anatomical, physiological and molecular properties of Martinotti cells in the somatosensory cortex of the juvenile rat. J. Physiol. (Lond.) 561 (1), 65–90.

Wehr, M., Zador, A. M., 2003. Balanced inhibition underlies tuning and sharpens spike timing in auditory cortex. Nature 426 (6965), 442–446.

Whittington, M. A., Traub, R. D., Kopell, N. J., Ermentrout, G. B., Buhl, E. H., 2000. Inhibition-based rhythms: experimental and mathematical observations on network dynamics. Int J Psychophysiol 38 (3), 315–336.

Wilent, W. B., Contreras, D., 2005. Dynamics of excitation and inhibition underlying stimulus selectivity in rat somatosensory cortex. Nat. Neurosci. 8 (10), 1364–1370.

Womelsdorf, T., Fries, P., Mitra, P. P., Desimone, R., 2006. Gamma-band synchronization in visual cortex predicts speed of change detection. Nature 439 (7077), 733–736.

Xu, X., Roby, K. D., Callaway, E. M., 2006. Mouse cortical inhibitory neuron type that coexpresses somatostatin and calretinin. J. Comp. Neurol. 499 (1), 144–160.

Xu, X., Roby, K. D., Callaway, E. M., 2010. Immunochemical characterization of inhibitory mouse cortical neurons: three chemically distinct classes of inhibitory cells. J. Comp. Neurol. 518 (3), 389–404.

Chapter 2:

Driving fast-spiking cells induces gamma rhythm and controls sensory responses

This chapter has previously been published as:
Jessica A. Cardin[*], Marie Carlén[*], Konstantinos Meletis, Ulf Knoblich, Feng Zhang, Karl Deisseroth, Li-Huei Tsai and Christopher I. Moore (2009). Driving fast-spiking cells induces gamma rhythm and controls sensory responses. Nature 459 (7247), 663–667.

I performed and analyzed the intracellular *in vivo* recordings demonstrating the subthreshold effect in pyramidal neurons of optogenetic activation of PV cells in primary somatosensory cortex, confirming perisomatic inhibitory post-synaptic potentials most likely mediated by $GABA_A$. These results are shown in Figure 2b and 2c of the manuscript.

2.1 Abstract

Gamma oscillations at 20-80Hz in the cortex predict increased attention[1] and are thought to bind sensory representations into coherent percepts[2]. Failed regulation of these oscillations is a hallmark of neurological and psychiatric diseases, including schizophrenia[3-5]. Current theory predicts that gamma oscillations are generated by synchronous activity of fast-spiking (FS) inhibitory interneurons[6-9], with the time course of FS-evoked inhibition leading to selective expression of 20-80 Hz activity in the local network. This synchronous inhibition is further predicted to create a narrow window for effective excitation, creating synchrony in neural ensembles. We causally tested these hypotheses in the *in vivo* barrel cortex (SI) by targeting optogenetic manipulation selectively to FS interneurons. By pulsing light across a broad range of frequencies (8-200 Hz), we directly linked activation of fast spiking inhibition and gamma oscillations (20-80 Hz). In contrast, activation of pyramidal neurons using a parallel approach amplified only lower frequency bands (<24 Hz). This cell type-specific double dissociation provides direct *in vivo* evidence that synchronous FS inhibition generates cortical gamma oscillations. This approach further allowed us to test the prediction that gamma oscillations temporally regulate sensory transmission. In agreement with this hypothesis, we find that the fine timing of sensory input relative to a cycle of gamma determines the amplitude, timing and precision of evoked sensory activity in SI. Our data provide the first causal evidence that a network activity state can be induced *in vivo* by cell-type specific activation, and directly support the FS-gamma hypothesis.

2.2 Main Text

Brain states characterized by rhythmic electrophysiological activity have been studied intensively for over 80 years[10,11]. Because these brain rhythms are believed to be essential to information processing, many theories have been proposed to explain their origin, with several emphasizing the activity of neuronal sub-types. One of the strongest cases yet made for the importance of a specific cell type in rhythm induction is the suggested role of FS interneurons in gamma (γ) oscillations[8,12]. Networks of FS cells connected by gap junctions[13,14] provide large, synchronous inhibitory postsynaptic potentials (IPSPs) to local excitatory neurons[15]. Computational modeling suggests that this synchronous activity is sufficient to induce 20-80 Hz

oscillations that are stabilized and regulated by fast excitatory feedback from pyramidal neurons[16,17]. Cortical recordings *in vivo* show sensory-evoked γ oscillations in the local field potential (LFP) and phase-locked firing of excitatory pyramidal cells, suggesting entrainment of excitatory neurons to rhythmic inhibitory activity[15,18]. Despite considerable study of cortical oscillations, and the importance of understanding their origins, induction of a given network state by stimulation of specific neural cell types *in vivo* has not previously been possible.

To directly test the hypothesis that FS interneuron activity in an in vivo cortical circuit is sufficient to induce γ oscillations, we used the light-sensitive bacteriorhodopsin Chlamydomonas reinhardtii Channelrhodopsin-2 (ChR2), a cation channel activated by ~ 470 nm blue light[19,20]. We targeted expression of ChR2 specifically to parvalbumin-positive fast-spiking (FS-PV+) interneurons by injecting the adeno-associated viral vector AAV Double-floxed Inverted Open reading frame-ChR2-mCherry (AAV DIO ChR2-mCherry), with Cre-dependent expression of ChR2, into PV-Cre knock-in mice (Fig. 1a; Supplementary Fig. 1-2 and Methods)[21,22]. Six days after virus injection into barrel cortex of adult PV-Cre mice, ChR2-mCherry expression covered an anterioposterior distance up to 1740 μm (1695 ± 57.4 μm, mean ± SD, n = 3), resulting in robust labeling of PV^+ interneurons across cortical layers (Fig. 1b). The labeling efficiency of AAV DIO ChR2-mCherry varied over distance from the injection site; close to the center of the injection, >97% of the PV^+ interneurons expressed ChR2-mCherry. Immunohistochemistry confirmed that 96.7 ± 1.0% (mean ± SD, n = 4234 ChR2-$mCherry^+$ neurons, 4 animals) of the ChR2-$mCherry^+$ neurons expressed PV (Fig. 1d-e, Supplementary Fig. 2), and almost all expressed the inhibitory neurotransmitter gamma-aminobutyric acid (GABA) (Supplementary Fig. 3)[23,24]. Expression of ChR2-mCherry was not induced after injection of AAV DIO ChR2-mCherry into wild-type mice (data not shown) or *in vitro* in the absence of Cre (see Supplementary Methods; data not shown).

In experiments targeting excitatory neurons, AAV DIO ChR2-mCherry was injected into the barrel cortex of adult CW2 mice[25] that express Cre from the αCamKII promoter ('αCamKII-Cre mice'), inducing recombination in excitatory neurons in cortex[25]. Robust ChR2-mCherry expression was observed in excitatory neurons in a laminar profile corresponding to the Cre expression pattern[25] (Fig. 1c, Supplementary Fig. 4). At least 50% of the $CamKII^+$ neurons in layer 2/3 expressed ChR2-mCherry (913 of 1638 cells in a total area of 8.4 x 10^6 μm^3) close to the injection site, covering an anterioposterior distance of 1560 ± 154.9 μm (mean ± SD, n = 3).

Immunohistochemical analysis revealed that 100 ± 0% (mean ± SD, n = 4024 ChR2-mCherry$^+$ neurons, 4 animals) of the ChR2-mCherry expressing neurons were immuno-negative for PV (Fig. 1f-g, Supplementary Fig. 2), and 100 ± 0% expressed the neuronal marker NeuN (data not shown).

We recorded light-activated FS and regular spiking (RS) single units in layers 2/3 and 4 of barrel cortex (SI) in PV-Cre (n = 64 FS in 15 animals) and αCamKII-Cre (n = 56 RS in 7 animals) mice. We did not observe light activation of layer 5 FS cells (n = 12 sites in 7 animals). Barrel cortex, which processes information from the rodent vibrissae (whiskers), was targeted as a well-defined model of basic sensory cortical function. In agreement with the immunohistological results, the action potential shapes of the neurons activated by light pulses were differentiated into two discrete populations based on mouse type, PV-Cre/FS and αCamKII-Cre/RS ($p < 0.01$; Fig. 2a).

To confirm the activation of inhibitory interneurons and their postsynaptic impact on excitatory neurons, we performed *in vivo* intracellular recordings of RS cells in barrel cortex in PV-Cre mice (n = 5). We found that a 1 ms light pulse was sufficient to evoke large, fast IPSPs, confirming direct synaptic inhibition of RS cells by light-activated FS cells (Fig. 2b). The latencies of the presynaptic light-evoked FS spikes agreed well with the onset times of the postsynaptic IPSPs, with FS spikes preceding IPSP onset by 0.5 to 0.75 ms (Fig. 2c). Both the time to peak and the peak timing variability of the evoked IPSPs decreased with increasing light pulse power (Fig. 2c). Mean IPSP peak amplitude at membrane potentials of -55 to –60 mV was 2.7 ± 1.0 mV. The mean reversal potential of the evoked IPSPs (see Supplementary Methods) was –67.6 ± 1.9 mV, indicating a $GABA_A$-mediated Cl^- conductance characteristic of FS synapses. Consistent with IPSP induction, activation of FS cells blocked vibrissa-evoked responses in neighboring RS cells (Figure 2d-e; n = 6 sites in 5 PV-Cre mice).

A strong prediction of the FS-γ hypothesis is that synchronously active FS cells are sufficient for γ induction. This hypothesis predicts that light pulses presented at a broad range of frequencies should reveal a selective peak in enhancement of the LFP, a measure of synchronous local network activity[26], when FS cells are driven in the γ range.

To test this hypothesis, we drove cortical FS cell spiking in virus-transduced PV-Cre mice at a range of frequencies (8 to 200 Hz) with 1 ms light pulses. Light pulses in the γ range (40 Hz)

resulted in reliable action potential output at 25 ms intervals (Fig. 3a). Across the population, FS and RS cells were driven with equally high reliability by light pulses at low frequencies (Fig. 3b). At higher frequencies, spike probability on each light cycle remained high for FS cells but decreased for RS cells.

Driving FS cells at 40 Hz caused a specific increase in the 35-40 Hz frequency band in the LFP (Fig. 3c, Supplementary Fig. 5-6). We found that activation of FS cells in the 20-80 Hz range resulted in significant amplification of LFP power at those frequencies (n = 14 sites in 6 animals; Fig. 3d). However, activation of FS cells at lower frequencies did not affect LFP power, despite robust evoked FS firing on every light cycle. In contrast, 8-24 Hz light activation of RS cells in αCamKII-Cre mice induced increased LFP power at these frequencies, but RS activation at higher frequencies did not affect LFP power (n = 13 sites in 5 mice; Fig. 3d, Suppl. Fig. 5). Light stimulation in the untransduced contralateral barrel cortex did not affect LFP power at any frequency (n = 6 PV-Cre and 5 αCamKII-Cre animals; Supplementary Fig. 6).

This double dissociation of cell-type specific state induction (γ by FS and lower frequencies by RS) directly supports the prediction that FS-PV^+ interneuron activation is sufficient and specific for induction of γ oscillations. To highlight this distinction, we compared the effects of stimulating the two cell types at 8 and 40 Hz. Stimulation of FS cells at 8 Hz in the PV-Cre mice had no effect on LFP power at 8Hz, but FS stimulation at 40 Hz caused a significant increase in 40 Hz LFP power (paired t-test; $p < 0.001$; Fig. 3e). In contrast, stimulation of RS cells at 8 Hz in the αCamKII-Cre mice caused a significant elevation of LFP power at 8 Hz ($p < 0.001$), whereas RS stimulation at 40 Hz caused only a small, nonsignificant increase in 40 Hz LFP power (Fig. 3f).

One possible explanation for these results is that increased FS firing recruits resonant γ range activity in the surrounding local network as a function of the synaptic and biophysical properties of the cortical circuit. Alternatively, the increase in γ activity may result from the specific level of evoked FS spiking, and changing spiking probability would shift the frequency of the enhanced LFP band. To discriminate between these possibilities, we stimulated FS cells at varying levels of light intensity. We found that FS spike probability changed with light intensity such that the spike probability curve shifted laterally (Fig. 3g). While drive impacted the amplitude of enhancement, LFP power was selectively amplified within the γ range regardless of light intensity or spike probability (Fig. 3h), indicating that the γ oscillations evoked by FS

activity are a resonant circuit property. In addition, randomly patterned light stimulation of FS cells with frequencies evenly distributed across a broad range evoked a significant increase in LFP power specific to the γ range (n = 7 sites in 4 animals; $p < 0.05$; Supplementary Fig. 7), further indicating that FS-evoked γ oscillations are an emergent property of the circuit, and do not require exclusive drive in the γ range.

To test whether intrinsically occurring γ oscillations show a similar dependence on FS activity, we gave single light pulses during epochs of natural γ. We found that brief FS activation shifted the phase of both spontaneously occurring γ oscillations (n = 26 trials, 4 animals; Kruskal-Wallis test with Dunn's post-test; $p < 0.01$; Fig. 3i) and those evoked by midbrain reticular formation stimulation (n = 18 trials, 2 animals; $p< 0.05$; Supplementary Fig. 8). Further, light-induced γ oscillations were largely eliminated by blocking AMPA and NMDA receptors, despite high levels of evoked FS firing (n = 4 sites in 4 animals; $p < 0.01$; Supplementary Fig. 9). These results indicate that induced γ oscillations dependent on rhythmic excitatory synaptic activity, as predicted by computational models of natural γ oscillations and prior experiments [6,15-17,27]. In further agreement, spontaneous RS activity was entrained by 40 Hz FS stimulation, resulting in RS firing during the decay phase of the IPSP and preceding subsequent evoked FS spiking (Supplementary Fig. 10).

Gamma oscillations are thought to have a functional impact on cortical information processing by synchronizing the output of excitatory neurons. This synchrony selects cell assemblies involved in a common task, such as encoding a sensory stimulus, and enhances their impact on downstream targets[2]. The cyclical FS inhibition underlying γ oscillations is believed to cause this synchrony by rhythmically gating synaptic inputs[2,28]. Synaptic inputs arriving at the peak of inhibition should therefore produce a diminished response, but those arriving at the opposite phase in the γ cycle should evoke a large response.

To directly test this hypothesis, we stimulated FS cells at 40 Hz with light pulses to establish γ oscillations, and recorded the responses of RS cells to a single vibrissa deflection presented at one of five phases relative to a single γ cycle (n = 20 cells in 3 animals; Fig. 4a). The timing of vibrissa-induced RS action potentials relative to light-evoked inhibition and the γ cycle had a significant impact on the amplitude, timing and precision of the sensory-evoked responses of RS cells (Fig. 4b-c). The presence of γ oscillations significantly decreased the amplitude of the RS

sensory response at three phase points, consistent with the enhanced level of overall inhibition in this state ($p < 0.05$; 1-way ANOVA with Dunnett's post-test; Fig. 4d)[29]. Gamma phase also modulated the overall timing of the sensory response ($p < 0.01$; Fig. 4e), with spike latency delayed at phases 1-3 and unaffected at phases 4-5[29]. The precision of sensory-evoked spikes was significantly enhanced in a γ phase-dependent manner ($p < 0.01$; Fig. 4f). Our results suggest that the rhythmic, FS-induced IPSP restricts sensory transmission during its peak, and permits transmission after its decay, leading to a temporal sharpening of cortical sensory responses (Fig. 4g).

Our results provide the first causal demonstration of cortical oscillations induced by cell type-specific activation. Synchronous FS-PV^+ interneuron activity driven by periodic stimulation of light-activated channels generated γ oscillations in a cortical network, and these gated sensory processing in a temporally specific manner. These findings also demonstrate a unique application of optogenetic engineering in the *in vivo* brain for the study of discrete neuronal cell types under active network conditions. Future use of these techniques will allow direct testing of the impact of brain states on information processing in the behaving animal[30], and potentially the rescue of functional states in models of brain disease[3,4].

2.3 Methods

AAV DIO ChR2-mCherry was injected into barrel cortex in adult PV-Cre21 and CW225 mice. Six days after injection, a subset of mice was perfused and tissue sectioned for immunohistochemistry to confirm location, transduction efficiency, and cell type specificity of ChR2 expression. Spread and immunohistochemical analysis of ChR2-mCherry expression was scored by hand through examination of every 30 μm coronal section for the presence of mCherry fluorescence. For electrophysiology, mice were anesthetized with isoflurane, and extracellular single-unit and local field potential recordings were made in layers 2/3 and 4 of barrel cortex with tetrodes or stereotrodes. Intracellular recordings were made in the whole-cell configuration. Light pulses were given via an optical fiber positioned at the cortical surface directly above the recording site. For experiments using a broad range of light stimulation frequencies, we stimulated in bouts of 3 sec at each frequency in random order. For each stimulation frequency, we measured relative power in an 8 Hz band centered on that frequency. Relative power was calculated by measuring the ratio of power within the band of interest to total power in the power

spectrum. To illustrate the impact of stimulation on the LFP, we also measured the ratio of power in a band with light stimulation to power in the band under baseline conditions. Vibrissae were stimulated by computer-controlled movements of piezoelectric wafers and consisted of single high-velocity deflections in the dorsal direction. For γ phase experiments, we gave a series of trials each consisting of a 1 sec series of 1 ms light pulses at 40 Hz, with a single whisker deflection after the 30th light pulse. The precise timing of the whisker deflection relative to the light pulses was varied across five phase points. All numbers are given as mean ± SEM, except where otherwise noted.

2.3.1 Animals

All procedures were conducted in accordance with the National Institutes of Health guidelines and with the approval of the Committee on Animal Care at MIT. PV-Cre (n = 21) and CW2 (n = 7) mice were 6-12 weeks of age at time of virus injections. Electrophysiological recordings and immunohistochemical analyses were performed 1-3 weeks after viral injections.

2.3.2 AAV vectors

ChR2 fused to the fluorescent protein mCherry was cloned in antisense direction into pAAV-MCS (Stratagene) to create AAV *D*ouble-floxed *I*nverted *O*pen reading frame-ChR2-mCherry (AAV DIO ChR2-mCherry) (Fig.1a and Supplementary Fig. 1; for vector outline and sequence see www.optogentics.org). ChR2-mCherry was flanked by a pair of canonical loxP sites and a pair of mutated loxP2272 sites. A woodchuck hepatatis B virus post-transcriptional element (WPRE) was placed in sense direction 5' of the poly-A. Adeno-associated viral particles of serotype 2 were produced by the Vector Core Facility at The University of North Carolina at Chapel Hill.

2.3.3 Virus injections

Adult PV-Cre[21] or CW2[25] mice were anesthetized with an intraperitoneal injection of a mixture of ketamine (1.1 mg/kg) and xylazine (0.16 mg/kg). A small craniotomy was made 1.5 mm posterior to bregma and 3.0 mm lateral to the midline. Virus was delivered through a small durotomy by a glass micropipette attached to a Quintessential Stereotaxic Injector (Stoelting). The glass micropipette was lowered to 0.4 mm below the cortical surface. A bolus of 0.5 μl of

virus (AAV DIO ChR2-mCherry; $2x10^{12}$ viral molecules/ml) was injected into barrel cortex at 0.1 µl/min. The pipette was then retracted to a depth of 250 microns below the surface and an additional 0.5 µl virus was injected at the same rate. The pipette was held in place for 5 minutes after the injection before being retracted from the brain. The scalp incision was sutured, and post-injection analgesics were given to aid recovery (0.1 mg/kg Buprenex).

2.3.4 Immunohistochemistry

Mice were transcardially perfused with 100 mM PBS followed by 4% formaldehyde in PBS, and brains were post-fixed overnight at 4°C. Free floating sections (30 µm) were cut using a vibratome (Leica VT100) and incubated with blocking solution (10% donkey serum in PBS with 0.3% Triton-X 100) for 1h at room temperature, then incubated at room temperature over night with primary antibody diluted in blocking solution. The following primary antibodies were used: NeuN (Chemicon; 1:1000), Parvalbumin PVG-214 (Swant; 1:2000), GABA (Sigma; 1:4000), and CamKII (Epitomics 1:500). After washing, antibody staining was revealed using species-specific fluorophore-conjugated secondary antibodies (Cy5 from Jackson, Alexa 488 from Molecular Probes). GABA was detected with biotinylated secondary antibodies (Jackson Laboratories) and revealed using a combination of ABC kit (Vector Laboratories) and TSA fluorescent amplification kit (Perkin-Elmer). Sections were mounted on glass slides with Vectashield (Vector) and coverslipped.

Spread and labeling efficiency were scored by hand through examination of every 30 µm coronal section (n = 3 animals per genotype) for the presence of mCherry fluorescence using a Zeiss LSM510 confocal microscope. For quantification of co-labeling of ChR2-mCherry and PV (n = 4 animals per genotype) confocal images were acquired and individual cells were identified independently for each of the two fluorescent channels. Scans from each channel were collected in multi-track mode to avoid cross-talk between channels.

2.3.5 Electrophysiology

Mice were anesthetized with isoflurane and held in place with a head post cemented to the skull. All incisions were infiltrated with lidocaine. A small craniotomy was made over barrel cortex approx 200 µm anterior to the virus injection site. Extracellular single-unit and local field potential recordings were made with tetrodes or stereotrodes. Intracellular recordings were

conducted by whole cell *in vivo* recording in current clamp mode. Stimulus control and data acquisition was performed using software custom written in LabView (National Instruments, Austin TX) and Matlab (The Mathworks, Natick MA) by U.K. Further electrophysiology methods and a description of the reversal potential calculation are given in Supplementary Methods.

Light stimulation was generated by a 473nm laser (Shanghai Dream Lasers, Shanghai, China) controlled by Grass stimulator (Grass Technologies, West Warwick, RI) or computer. Light pulses were given via a 200μm diameter, unjacketed optical fiber (Ocean Optics, Dunedin FL) positioned at the cortical surface directly above the recording site. For experiments using the broad range of light stimulation frequencies (8, 16, 24, 32, 40, 48, 80, 100, and 200 Hz), we stimulated in bouts of 3 sec of 1 ms pulses at 4 mW/mm^2 at each frequency in random order. In a subset of these experiments, we stimulated at 1, 4 and 8 mW/mm^2.

Vibrissae were stimulated by computer-controlled movements of piezoelectric wafers (Piezo Systems). Vibrissa stimulations were single high-velocity deflections in the dorsal then ventral direction (~6 ms duration). In most cases, adjacent vibrissae that yielded indistinguishable amplitude responses during hand mapping were deflected simultaneously. Vibrissa stimulations evoked RS spike responses with an onset latency of 9.1 ± .08 ms. For RS cell response suppression experiments, light pulses were given on randomly interleaved trials. For γ□phase experiments, we gave a series of trials each consisting of a 1 sec series of 1 ms light pulses at 40 Hz, with a single whisker deflection after the 30th light pulse. The precise timing of the whisker deflection relative to the light pulses was varied across five phase points. Each of the five phase points was included in random order across a minimum of 250 total trials.

Unit and local field potential analysis used software custom written in Igor Pro (Wavemetrics, Portland OR) by J.A.C. For each stimulation frequency, we measured relative power in an 8 Hz band centered on that frequency. For each recording site, we measured power from 5-10 LFP traces under each condition. Example power spectra are averages of the power spectra from 5-10 traces of unfiltered LFPs from individual experiments. Relative power was calculated by measuring the ratio of power within the band of interest to total power in the power spectrum of the unfiltered LFP. We also measured the power ratio $P_{light}/ P_{baseline}$ where P_{light} is the relative power in a frequency band in the presence of light stimulation and $P_{baseline}$ is the power in that

band in the absence of light stimulation. All numbers are given as mean ± SEM, except where otherwise noted.

2.4 Author Contributions

J.A.C., M.C., K.M., L.-H.T., and C.I.M. designed the experiments. F.Z. and K.D. designed and cloned the AAV DIO ChR2-mCherry vector. M.C. and K.M. characterized the virus *in vitro* and *in vivo* and injected the animals. M.C performed histological statistical analyses. J.A.C. performed and analyzed the extracellular recordings. U.K. and J.A.C. performed the intracellular recordings. U.K. analyzed the intracellular data. J.A.C., M.C., K.M., U.K., L.-H.T., and C.I.M. wrote the manuscript.

2.5 References

1. Fries, P., Reynolds, J. H., Rorie, A. E. & Desimone, R. Modulation of oscillatory neuronal synchronization by selective visual attention. *Science* **291**, 1560-3 (2001).

2. Engel, A. K. & Singer, W. Temporal binding and the neural correlates of sensory awareness. *Trends Cogn Sci* **5**, 16-25 (2001).

3. Orekhova, E. V. et al. Excess of high frequency electroencephalogram oscillations in boys with autism. *Biol Psychiatry* **62**, 1022-9 (2007).

4. Spencer, K. M., Niznikiewicz, M. A., Shenton, M. E. & McCarley, R. W. Sensory-evoked gamma oscillations in chronic schizophrenia. *Biol Psychiatry* **63**, 744-7 (2008).

5. Uhlhaas, P. J., Haenschel, C., Nikolic, D. & Singer, W. The role of oscillations and synchrony in cortical networks and their putative relevance for the pathophysiology of schizophrenia. *Schizophr Bull* **34**, 927-43 (2008).

6. Traub, R. D., Jefferys, J. G. & Whittington, M. A. Simulation of gamma rhythms in networks of interneurons and pyramidal cells. *J Comput Neurosci* **4**, 141-50 (1997).

7. Traub, R. D., Whittington, M. A., Stanford, I. M. & Jefferys, J. G. A mechanism for generation of long-range synchronous fast oscillations in the cortex. *Nature* **383**, 621-4 (1996).

8. Whittington, M. A., Traub, R. D. & Jefferys, J. G. Synchronized oscillations in interneuron networks driven by metabotropic glutamate receptor activation. *Nature* **373**, 612-5 (1995).

9. Wang, X. J. & Buzsaki, G. Gamma oscillation by synaptic inhibition in a hippocampal interneuronal network model. *J Neurosci* **16**, 6402-13 (1996).

10. Steriade, M. Grouping of brain rhythms in corticothalamic systems. *Neuroscience* **137**, 1087-106 (2006).

11. Berger, H. On the electroencephalogram of man. *Electroencephalogr Clin Neurophysiol*, Suppl 28:37+ (1969).

12. Whittington, M. A., Faulkner, H. J., Doheny, H. C. & Traub, R. D. Neuronal fast oscillations as a target site for psychoactive drugs. *Pharmacol Ther* **86**, 171-90 (2000).

13. Deans, M. R., Gibson, J. R., Sellitto, C., Connors, B. W. & Paul, D. L. Synchronous activity of inhibitory networks in neocortex requires electrical synapses containing connexin36. *Neuron* **31**, 477-85 (2001).

14. Galarreta, M. & Hestrin, S. A network of fast-spiking cells in the neocortex connected by electrical synapses. *Nature* **402**, 72-5 (1999).

15. Hasenstaub, A. et al. Inhibitory postsynaptic potentials carry synchronized frequency information in active cortical networks. *Neuron* **47**, 423-35 (2005).

16. Whittington, M. A., Traub, R. D., Faulkner, H. J., Stanford, I. M. & Jefferys, J. G. Recurrent excitatory postsynaptic potentials induced by synchronized fast cortical oscillations. *Proc Natl Acad Sci U S A* **94**, 12198-203 (1997).

17. Borgers, C., Epstein, S. & Kopell, N. J. Background gamma rhythmicity and attention in cortical local circuits: a computational study. *Proc Natl Acad Sci U S A* **102**, 7002-7 (2005).

18. Gray, C. M. & Singer, W. Stimulus-specific neuronal oscillations in orientation columns of cat visual cortex. *Proc Natl Acad Sci U S A* **86**, 1698-702 (1989).

19. Boyden, E. S., Zhang, F., Bamberg, E., Nagel, G. & Deisseroth, K. Millisecond-timescale, genetically targeted optical control of neural activity. *Nat Neurosci* **8**, 1263-8 (2005).

20. Deisseroth, K. et al. Next-generation optical technologies for illuminating genetically targeted brain circuits. *J Neurosci* **26**, 10380-6 (2006).

21. Hippenmeyer, S. et al. A developmental switch in the response of DRG neurons to ETS transcription factor signaling. *PLoS Biol* **3**, e159 (2005).

22. Kuhlman, S. J. & Huang, Z. J. High-resolution labeling and functional manipulation of specific neuron types in mouse brain by Cre-activated viral gene expression. *PLoS ONE* **3**, e2005 (2008).

23. Ren, J. Q., Aika, Y., Heizmann, C. W. & Kosaka, T. Quantitative analysis of neurons and glial cells in the rat somatosensory cortex, with special reference to GABAergic neurons and parvalbumin-containing neurons. *Exp Brain Res* **92**, 1-14 (1992).

24. Ascoli, G. A. et al. Petilla terminology: nomenclature of features of GABAergic interneurons of the cerebral cortex. *Nat Rev Neurosci* **9**, 557-68 (2008).

25. Zeng, H. et al. Forebrain-specific calcineurin knockout selectively impairs bidirectional synaptic plasticity and working/episodic-like memory. *Cell* **107**, 617-29 (2001).

26. Hubbard, J. I., Llinas, R. & Quastel, D. M. J. *Electrophysiological analysis of synaptic transmission.* (The Camelot Press Ltd., London, 1969).

27. Borgers, C. & Kopell, N. Effects of noisy drive on rhythms in networks of excitatory and inhibitory neurons. *Neural Comput* **17**, 557-608 (2005).

28. Burchell, T. R., Faulkner, H. J. & Whittington, M. A. Gamma frequency oscillations gate temporally coded afferent inputs in the rat hippocampal slice. *Neurosci Lett* **255**, 151-4 (1998).

29. Fries, P., Neuenschwander, S., Engel, A. K., Goebel, R. & Singer, W. Rapid feature selective neuronal synchronization through correlated latency shifting. *Nat Neurosci* **4**, 194-200 (2001).

30. Huber, D. et al. Sparse optical microstimulation in barrel cortex drives learned behaviour in freely moving mice. *Nature* **451**, 61-4 (2008).

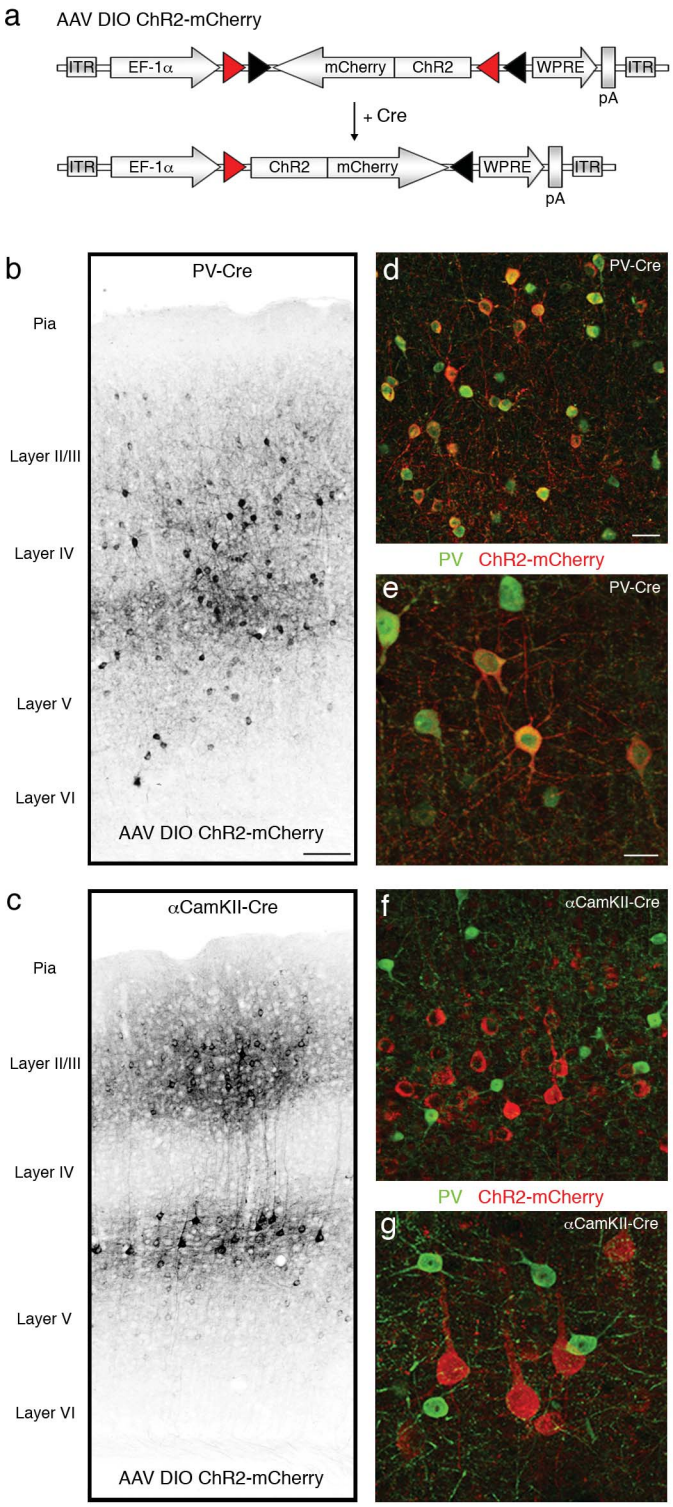
a
AAV DIO ChR2-mCherry
ITR
EF-1α
mCherry
ChR2
WPRE
pA
ITR
+ Cre
ITR
EF-1α
ChR2
mCherry
WPRE
pA
ITR
b
PV-Cre
Pia
Layer II/III
Layer IV
Layer V
Layer VI
AAV DIO ChR2-mCherry
d
PV-Cre
PV ChR2-mCherry
e
PV-Cre
c
αCamKII-Cre
Pia
Layer II/III
Layer IV
Layer V
Layer VI
AAV DIO ChR2-mCherry
f
αCamKII-Cre
PV ChR2-mCherry
g
αCamKII-Cre

Figure 1. AAV DIO ChR2-mCherry gives Cre-dependent and cell type-specific expression of light-activated channels *in vivo*. (a) AAV DIO ChR2-mCherry with Cre-dependent expression of ChR2 produced cell type-specific targeting of light-activated channels. In the presence of Cre, ChR2-mCherry is inverted into the sense direction and expressed from the EF1-α promoter. (b) ChR2-mCherry was robustly expressed in PV^+ interneurons in barrel cortex of adult PV-Cre mice. (c) A corresponding injection in αCamKII-Cre mice resulted in exclusive labeling of excitatory neurons. (d-e) ChR2-mCherry expression in PV-Cre mice was confined to cells expressing PV. (e) PV^+ cells with ChR2-mCherry expression and typical FS interneuron morphology. (f-g) ChR2-mCherry expression in αCamKII-Cre mice is confined to neurons immuno-negative for PV. (g) ChR2-mCherry-expressing cells with typical pyramidal neuron morphology. Scale bars are the same in (b-c; 100 μm), (d, f; 25 μm) and in (e, g; 25 μm).

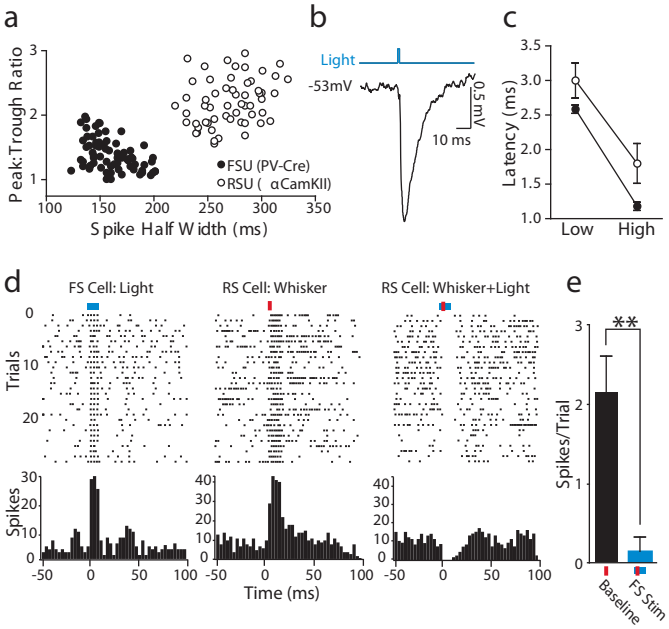

Figure 2. Light-evoked activity in fast-spiking, PV^+ inhibitory interneurons suppresses sensory processing in nearby excitatory neurons. (a) Light-activated RS and FS cells recorded in layers 2/3 and 4 of barrel (SI) cortex in PV-Cre and αCamKII-Cre mice, respectively, formed two discrete overall populations based on waveform properties. (b) Intracellular *in vivo* recording of an RS cell in a PV-Cre animal. A 1 ms pulse of blue light (blue line) at low power evoked an IPSP with a sharp onset. (c) The latency to light-activated FS spikes (filled circles) agreed well with the onset latency of the resulting IPSPs (open circles). The IPSP time to peak decreased with increasing power (Low Power: 3 mW/mm^2, High Power: 8 mW/mm^2). (d) Sustained activation of FS inhibitory interneurons eliminated sensory responses in nearby RS neurons. A layer 2/3 FS cell was reliably activated by a 10 ms light pulse (blue line; left panel). An RS cell recorded on the same tetrode responded to vibrissa deflection (red bar; center panel). Activation of inhibitory activity simultaneously with vibrissa deflection eliminated the RS sensory response (right panel). (e) Mean RS vibrissa response decreased significantly in the presence of elevated FS cell activity. Asterisks denote $p < 0.01$; error bars are mean ± SEM.

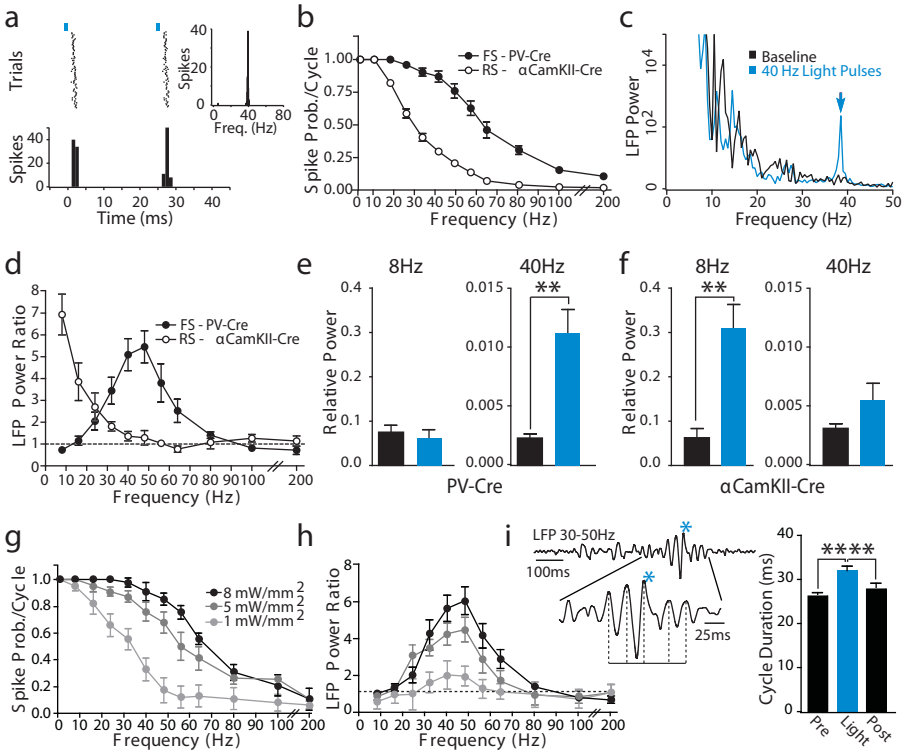

Figure 3. Fast spiking inhibitory interneurons generate gamma oscillations in the local cortical network. (a) In response to 40 Hz light pulses (blue bars), this FS cell fired reliably at 25 ms intervals, giving an instantaneous firing frequency of 40 Hz (inset). (b) Average spike probability per light pulse cycle in light-activated FS and RS cells in the PV-Cre and αCamKII-Cre mice, respectively (RS n = 17, open circles; FS n = 22, filled circles). (c) Example of the increase in power at ~40 Hz in the local field potential (LFP) caused by activation of FS cells by light pulses at 40 Hz. (d) Mean power ratio in each frequency band in response to light activation of FS (filled circles) and RS (open circles) cells at those frequencies. (e-f) Comparison of the effect of activating FS and RS cells at 8 and 40 Hz on relative LFP power in those frequency bands. Black bars: relative power in the baseline LFP; Blue bars: relative power in the presence of light pulses. (g) Average spike probability of FS cells per light pulse cycle in response to three levels of light intensity. (h) Mean power ratios from LFP recordings at the light intensity levels shown in (g). (i) Trace shows spontaneously occurring γ activity in the LFP. Brief activation of FS cells (blue asterisk) prolonged the duration of the ongoing γ cycle and consequently shifted the phase of the following cycles. The duration of the cycle during which the light stimulus was given (Light)

was significantly longer than the preceding (Pre) or following cycle (Post). Asterisks denote $p < 0.01$; error bars are mean ± SEM.

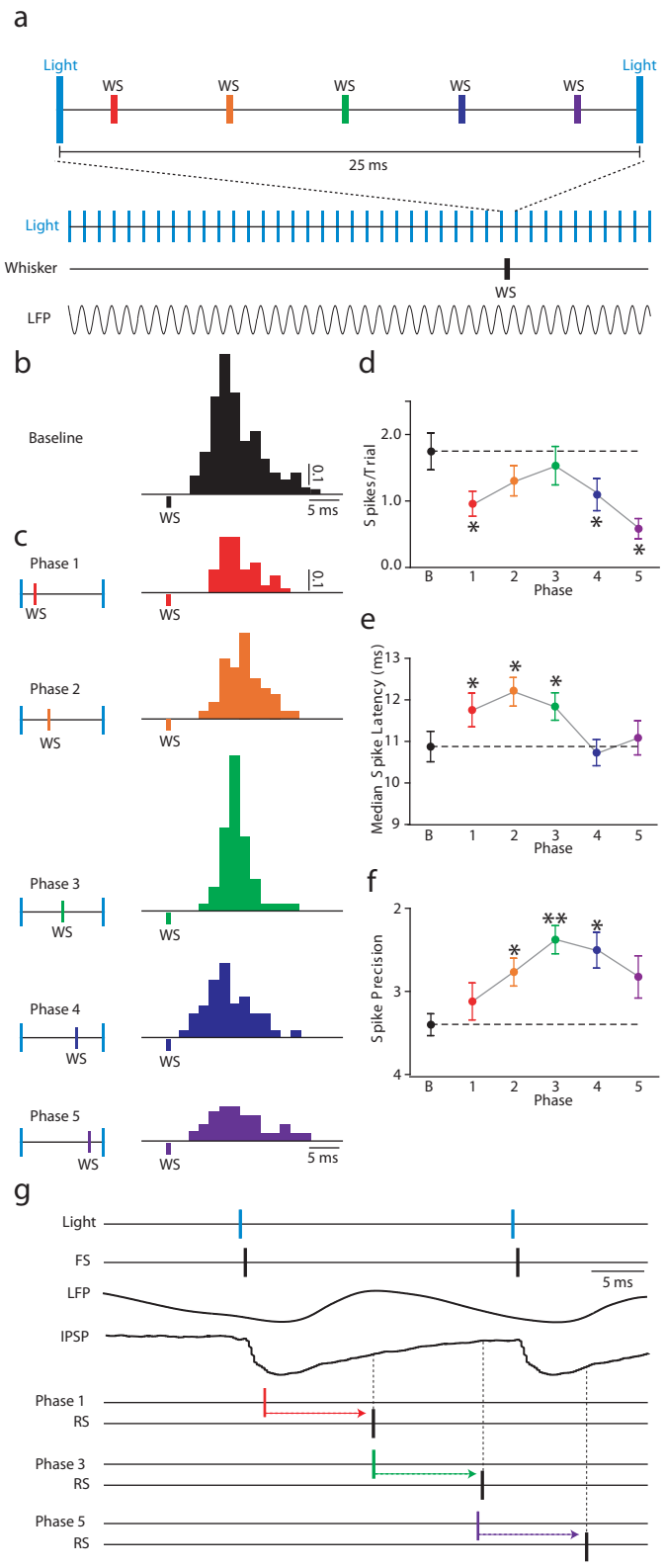
a
Light
WS
WS
WS
WS
WS
Light
25 ms
Light
Whisker
WS
LFP
b
Baseline
WS
0.1
5 ms
c
Phase 1
WS
Phase 2
WS
Phase 3
WS
Phase 4
WS
Phase 5
WS
d
Spikes/Trial
2.0
1.0
0.0
B 1 2 3 4 5
Phase
e
Median Spike Latency (ms)
13
12
11
10
9
B 1 2 3 4 5
Phase
f
Spike Precision
2
3
4
B 1 2 3 4 5
Phase
g
Light
FS
LFP
IPSP
5 ms
Phase 1
RS
Phase 3
RS
Phase 5
RS

Figure 4. Gamma oscillations gate sensory responses of excitatory neurons. (a) On each trial, FS-PV$^+$ inhibitory interneurons were activated at 40 Hz and a single vibrissa deflection was presented at one of five phases. (b) Baseline response of one layer 4 RS cell to single vibrissa deflections, shown in units of spikes/trial. (c) Responses of the same cell when the whisker was deflected at each of five temporal phases relative to the induced γ oscillation. Average spikes evoked per trial under each condition. (e) Timing of the RS spike response, measured as median spike latency. (f) Spike precision of the RS responses. (g) Schematic model of the gating of sensory responses by γ oscillations. IPSP and LFP examples are averaged data traces. Asterisks denote $p < 0.05$, $p < 0.01$; error bars are mean ± SEM.

2.7 Supplementary Figures

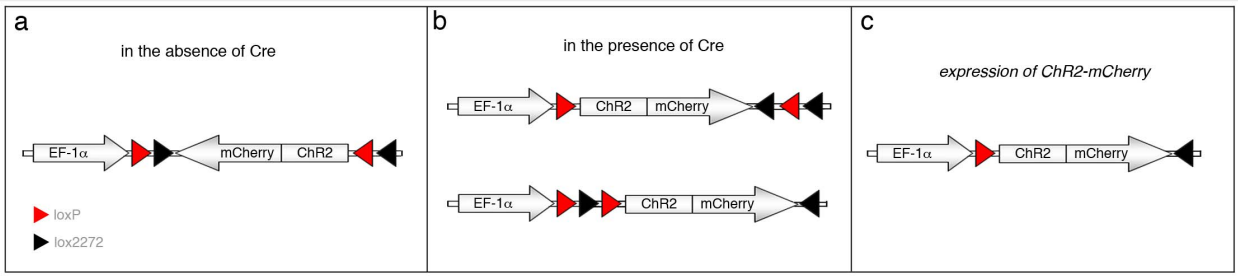

Supplementary Figure 1

Supplementary Figure 1. Cre dependent expression of the light-activated channel ChR2 (a) The adeno-associated viral vector AAV DIO ChR2-mCherry carries an inverted version of ChR2 fused to the fluorescent marker mCherry. This strategy prevents ChR2 from being expressed in the absence of Cre. (b) The loxP variants loxP and lox2272 flanking ChR2-mCherry are incompatible and cannot recombine with each other[1], leading to a stochastic recombination of either variant[2] in the presence of Cre. Because both loxP variants are constituted of lox pairs facing each other, recombination results in inversion of ChR2-mCherry into the sense orientation. As a consequence of the first recombination event, the second unrecombined loxP variant now is constituted of two directly oriented lox sites and will therefore excise one of the lox sites of the first loxP variant, an event that prevents further recombination. (c) This strategy eliminates possible misexpression of ChR2 due to leakiness of the commonly used translational stop cassettes and targets recombination and expression of ChR2-mCherry exclusively to Cre expressing cells.

1. Lee, G. & Saito, I. Role of nucleotide sequences of loxP spacer region in Cre-mediated recombination. *Gene* 216, 55-65 (1998).

2. Livet, J. et al. Transgenic strategies for combinatorial expression of fluorescent proteins in the nervous system. *Nature* 450, 56-62 (2007).

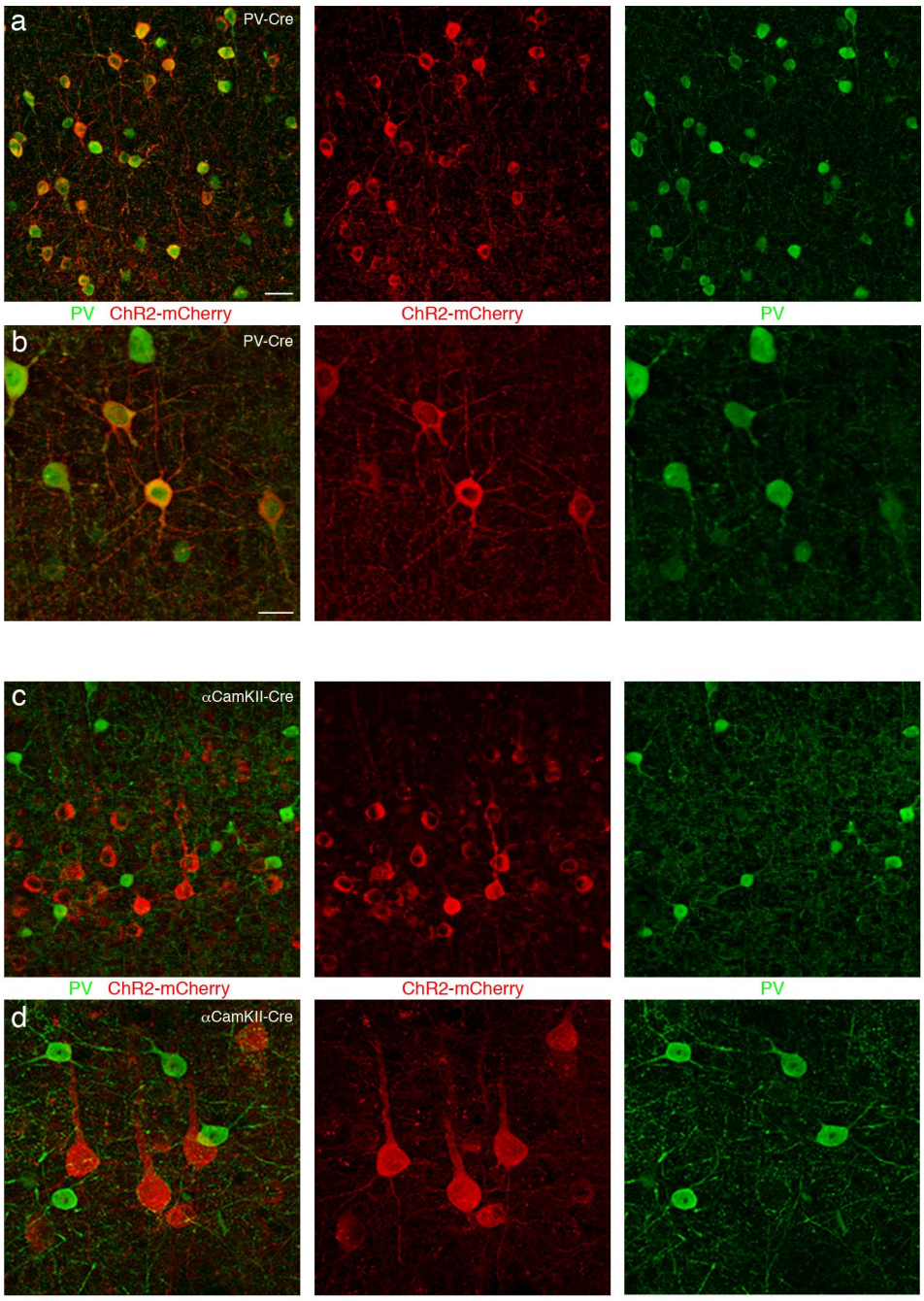

Supplementary Figure 2

Supplementary Figure 2. Cell type-specific expression of ChR2 in the adult barrel cortex. (a) When injected into the barrel cortex of adult PV-Cre mice, the viral vector AAV DIO ChR2-mCherry gave robust expression of ChR2 in PV^+ interneurons throughout cortical layers. (b)

Confocal Z-stack showing PV^+ cells with ChR2-mCherry expression and typical FS interneuron morphology. (c-d) A corresponding injection into the barrel cortex of αCamKII-Cre mice resulted in exclusive labeling of excitatory neurons. (c) ChR2-mCherry expression in αCamKII-Cre mice was confined to excitatory neurons immuno-negative for parvalbumin (PV). (d) Confocal Z-stack showing ChR2-mCherry expressing cells with typical pyramidal neuron morphology. Scale bars are the same in (a, c; 25 μm) and (b, d; 25 μm).

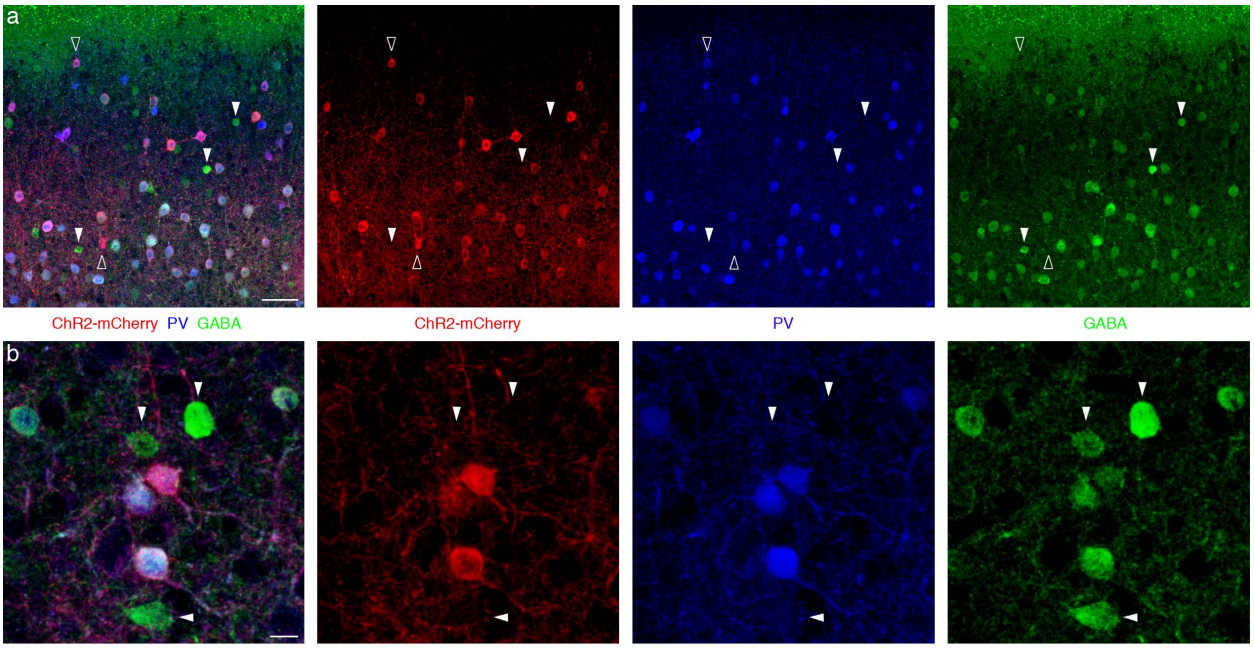

Supplementary Figure 3

Supplementary Figure 3. ChR2-mCherry expressing cells in PV-Cre mice are PV+ interneurons that express the inhibitory neurotransmitter GABA. (a-b) After injection of AAV DIO ChR2-mCherry into the barrel cortex of adult PV-Cre mice, expression of light-activated channels is found in GABAergic PV+ interneurons. (a) Confocal Z-stack of triple labeled cells in layer 2/3. Virtually all cells expressing ChR2-mCherry show detectable levels of PV and GABA. In the instance of low/non-detectable levels of GABA (hollow arrowheads) the ChR2-mCherry+ cells still show detectable levels of PV. White arrowheads point to GABAergic interneurons (GABA+) not expressing the Ca^{2+}-binding protein PV and therefore also lacking expression of light-activated channels. (b) High-magnification confocal Z-stack of triple labeled cells. GABAergic PV- interneurons are clearly lacking expression of ChR2-mCherry (white arrowheads). Scale bar is 50 μm in (a) and 10 μm in (b).

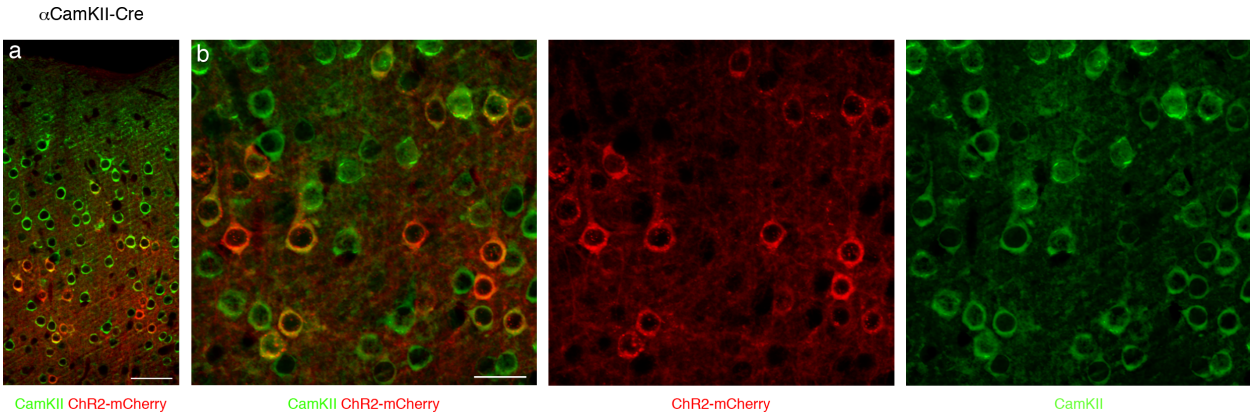

Supplementary Figure 4

Supplementary Figure 4. ChR2-mCherry expressing cells in αCamKII-Cre mice are CamKII$^+$ excitatory neurons . (a-b) After injection of AAV DIO ChR2-mCherry into the barrel cortex of adult αCamKII-Cre mice, expression of light-activated channels is restricted to CamKII$^+$ excitatory neurons. (a) One 3 μm section of layer 2/3. (b) Part of (a) in high-magnification, showing that ChR2-mCherry expressing neurons are immuno-positive for the excitatory marker CamKII. Scale bar is 50 μm in (a) and 25 μm in (b).

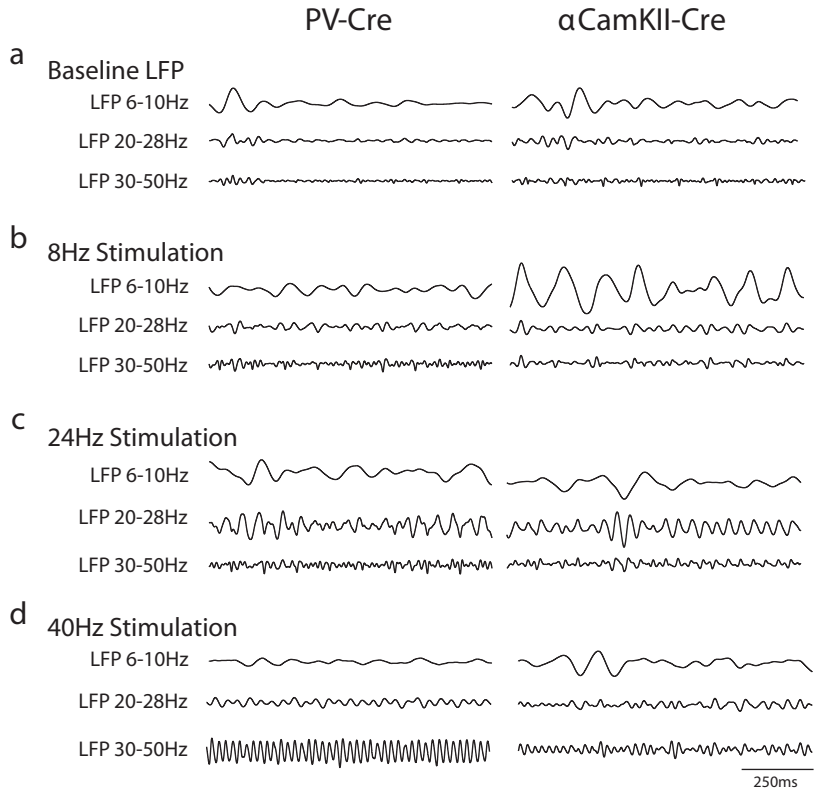

Supplementary Figure 5

Supplementary Figure 5. Examples of LFP traces from PV-Cre and αCamKII-Cre mice during baseline activity and varying frequencies of light stimulation.

(a) Baseline LFP recordings from barrel cortex in the absence of light stimulation. (b) Stimulation at 8 Hz evoked increased 8 Hz activity in αCamKII-Cre but not PV-Cre mice, but did not affect activity in the 24 or 40 Hz bands in either type of mouse. (c) Similarly, 24 Hz stimulation evoked a small increase in 24 Hz activity in both types of mouse but did not affect other frequency bands. (d) Stimulation at 40 Hz evoked a large 40 Hz oscillation in the PV-Cre mouse, but did not affect activity in any frequency band in the αCamKII-Cre mouse.

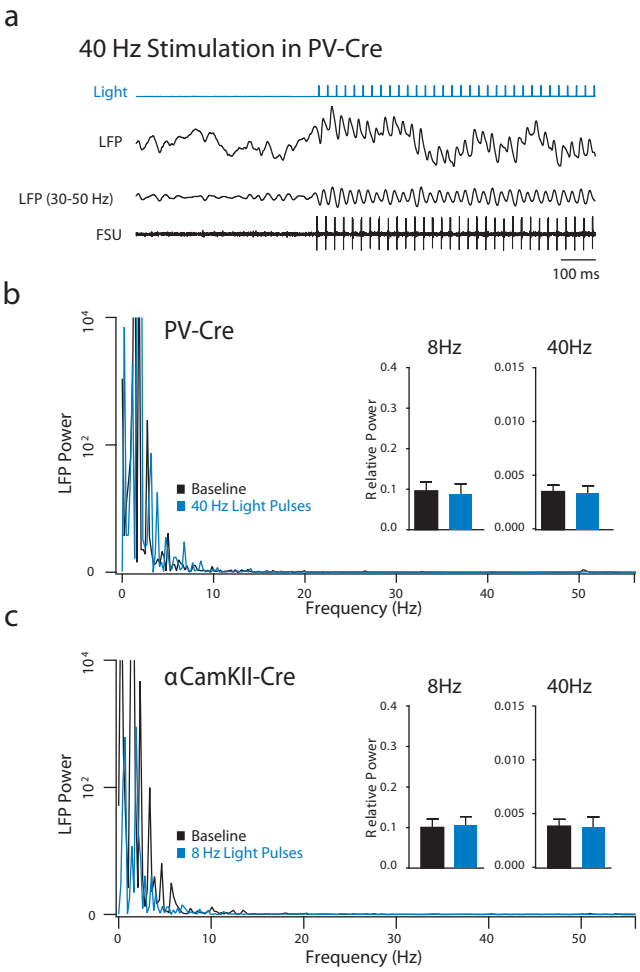

Supplementary Figure 6

Supplementary Figure 6. Light stimulation evokes LFP activity only in transduced tissue expressing ChR2. (a) LFP and single unit FS interneuron recording in a PV-Cre animal during 40 Hz stimulation with light pulses. Light pulses evoked a robust gamma oscillation in the LFP, which can be seen clearly in the trace filtered between 30 and 50 Hz. The recorded FSU fired one spike in response to each light pulse. (b) Light stimulation at 40 Hz did not affect the LFP in barrel cortex of the untransduced hemisphere of PV-Cre animals. In this example (left), there was no difference in LFP power in any frequency band between baseline (black) and 40 Hz light stimulation (blue) conditions. The bar graphs (right) show population averages (n = 6 animals) for LFP power in the 8 and 40 Hz frequency bands during baseline (black) and light stimulation

(blue) of untransduced cortex. (c) Similarly, 8 Hz light stimulation in barrel cortex of the untransduced hemisphere of an αCamKII-Cre animal had no impact on LFP power in this example (left). Across the population, there was no impact of light stimulation in either the 8 or 40 Hz bands (n = 5 animals; right).

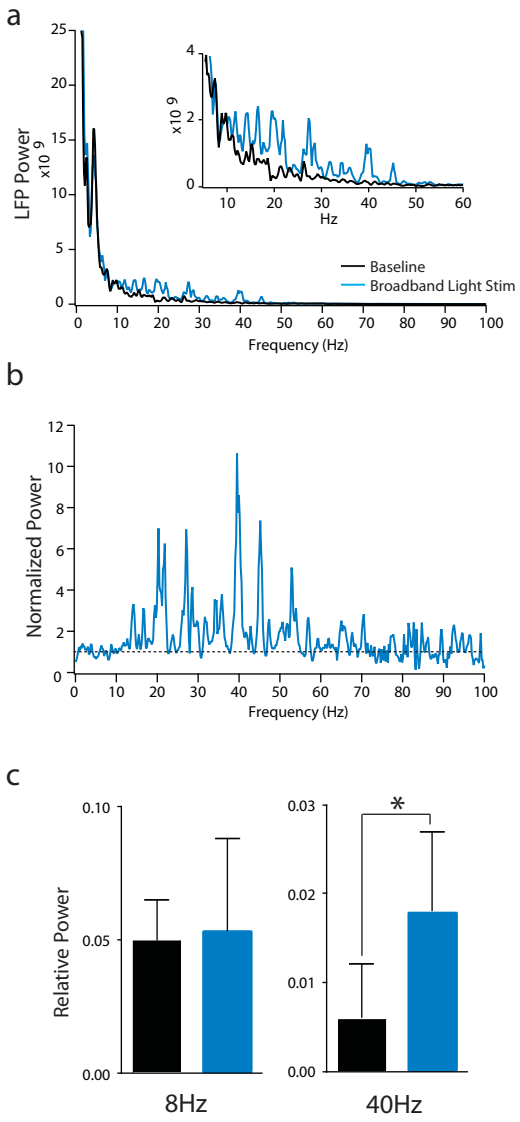

Supplementary Figure 7

Supplementary Figure 7. Broadband light stimulation evoked LFP activity in the gamma range. (a) The broadband stimulus (5-200 Hz) evoked an increase in LFP power that was specific to the gamma range (20-80 Hz), even though the stimulus contained many other frequencies. Inset traces show an expanded portion of the LFP power spectra. Baseline power spectrum is shown in black, power spectrum during broadband light stimulation is shown in blue. (b) LFP power spectrum during broadband stimulation, normalized to the baseline power spectrum. (c) Relative LFP power in the 8 Hz (left) and 40 Hz (right) frequency bands during baseline activity (black)

and broadband light stimulation (blue). Relative power was unaffected in the 8 Hz band, but was significantly increased in the 40 Hz band ($n = 7$ sites in 4 animals; $p < 0.05$).

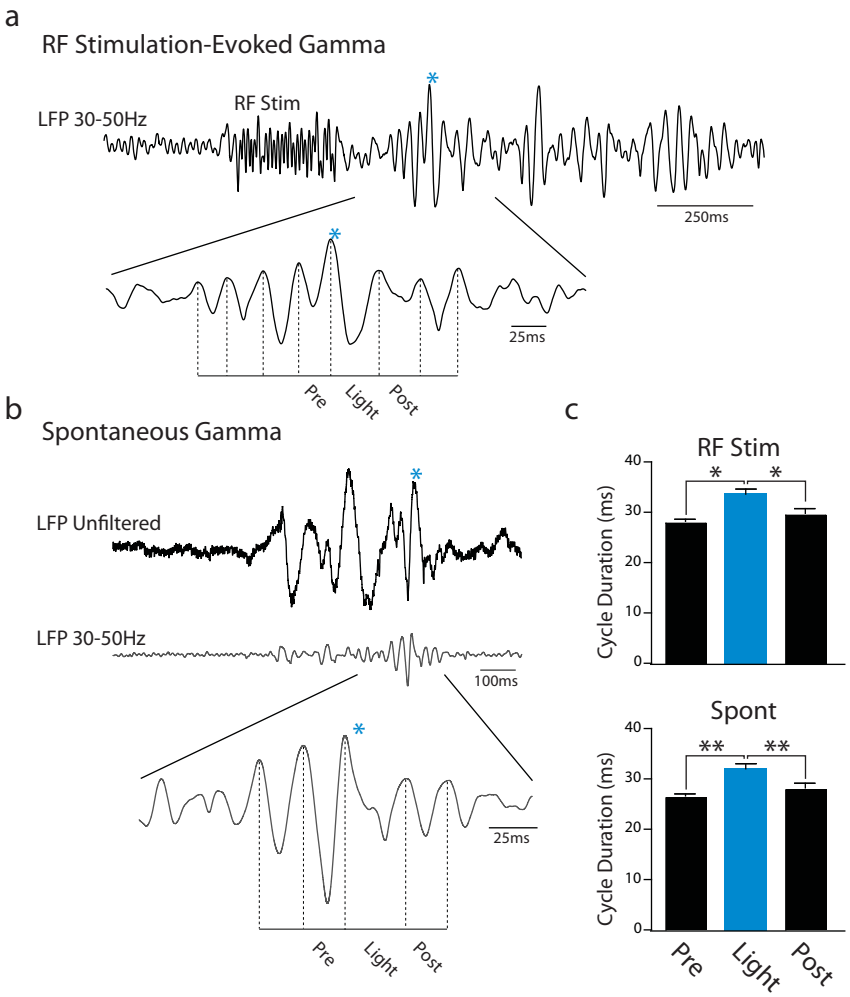

Supplementary Figure 8

Supplementary Figure 8. Brief stimulation of FS cells during naturally occurring gamma shifts the phase of the ongoing oscillation. (a) Stimulation of the midbrain reticular formation (RF) led to increased gamma activity (n = 18 trials, 2 animals). A brief light pulse was given during an ongoing gamma oscillation (blue asterisk), prolonging the ongoing gamma cycle and shifting the phase of the following cycles relative to the pre-light oscillation. (b) FS stimulation during naturally occurring gamma observed during spontaneous LFP activity (n = 26 trials, 4 animals). Upper trace: unfiltered example of LFP activity. Center trace: gamma frequency band. Lower trace: enlarged portion of the filtered LFP, with a brief pulse of light denoted by the blue asterisk. (c) FS activation by the light pulse significantly increased the duration of the ongoing

gamma cycle (Light) in comparison to the preceding (Pre) and following (Post) cycles during gamma oscillations evoked by RF stimulation (Kruskal-Wallis test with Dunn's post-test; $p < 0.05$). Similarly, FS activation increased the duration of the ongoing gamma cycle during spontaneous gamma oscillations, as shown in the example in (b) ($p < 0.01$).

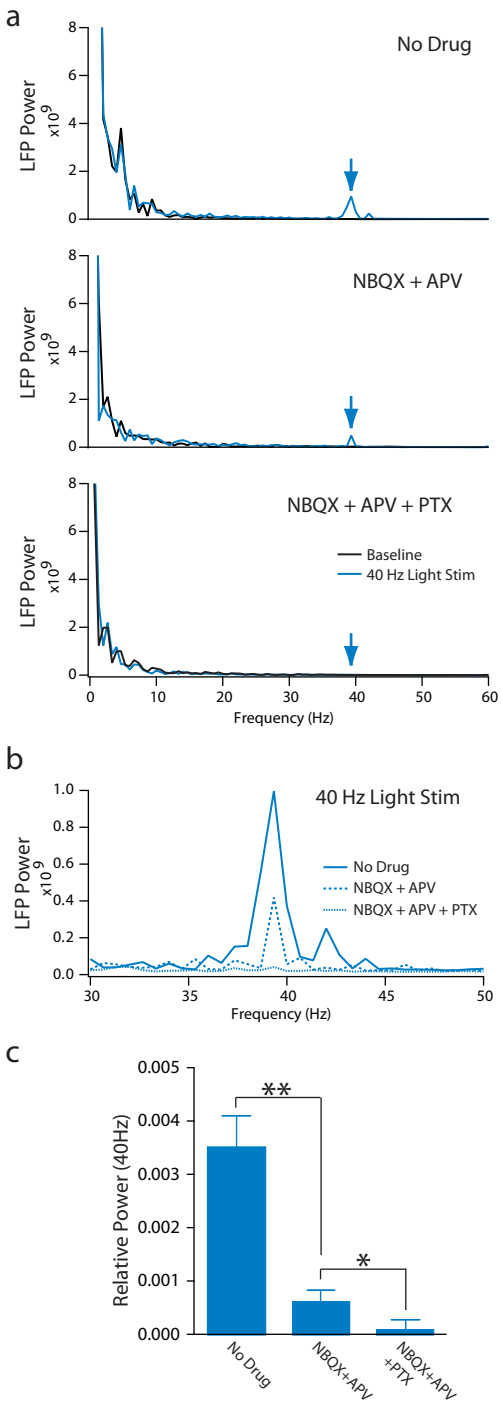

Supplementary Figure 9

Supplementary Figure 9. Gamma oscillations induced by FS activation require excitatory synaptic activity. (a) Upper panel: LFP power spectra from a PV-Cre animal in the absence of pharmacological manipulation, showing robust gamma activity evoked by 40 Hz light stimulation (arrows). Middle Panel: LFP power spectra after blockade of AMPA and NMDA receptors with NBQX and APV, respectively. Lower Panel: LFP power spectra after additional blockade of GABAa receptors by picrotoxin. (b) Enlarged overlay of the gamma range of the LFP power spectra during light stimulation under each pharmacological condition. (c) Blockade of AMPA and NMDA receptors significantly decreased the relative power evoked in the gamma frequency band by the light ($n = 4$ sites in 4 animals; $p < 0.01$). The remaining 40 Hz activity in the LFP was eliminated by further blockade of GABAa receptors ($p < 0.05$).

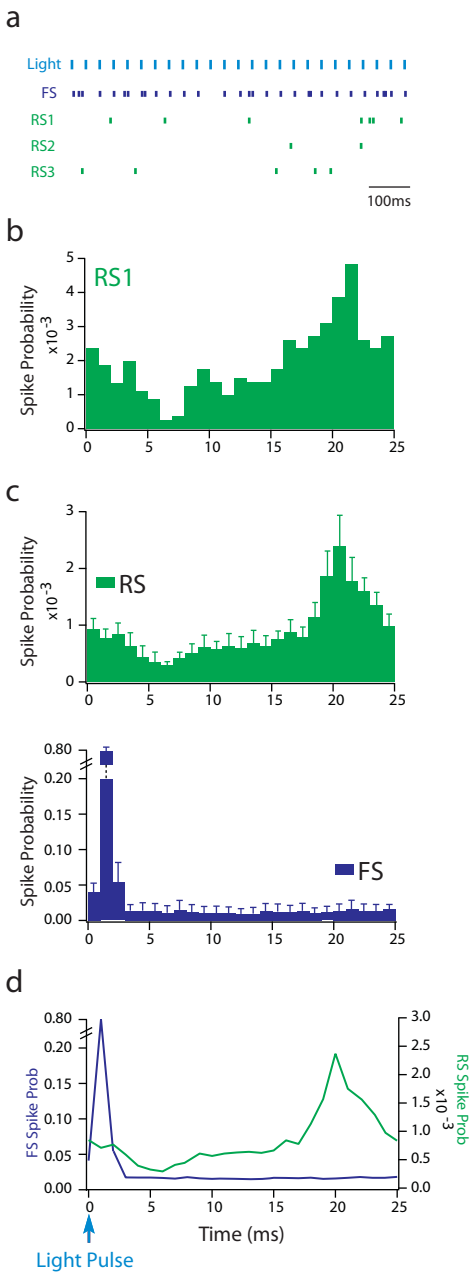

Supplementary Figure 10

Supplementary Figure 10. Gamma oscillations rhythmically entrain spontaneous RS activity. (a) Raster plot from one experiment, showing repeated activation of an FS cell (blue) by light pulses. Three nearby RS cells were recorded simultaneously (RS1-3, green). (b) Cycle histogram of the spiking activity of RS1 from (a), with 0 set as the time of the light flash on each cycle. (c)

Upper panel: Population cycle histogram from 17 RS cells in 5 PV-Cre animals, showing a decrease in spike probability around 4-10 ms after the light flash and an increase in spike probability around 20 ms. Lower panel: Population cycle histogram from 9 FS cells recorded in the same experiments, showing a light-evoked peak in firing at 1-2 ms. (d) Overlay of the FS (blue) and RS (green) spike probability profiles. Light pulses at 0 ms evoked FS spikes with a delay of 1-2 ms, followed by an increase in RS spiking at 17-24 ms.

2.8 Supplementary Methods

2.8.1 AAV-DIO-ChR2-mCherry

This vector carries an inverted version of ChR2 fused to the fluorescent marker mCherry to prevent ChR2 from being expressed in the absence of Cre. ChR2-mCherry is flanked by a pair of canonical loxP sites (loxP) and a pair of mutated loxP sites (lox2272). In the presence of Cre, ChR2-mCherry is inverted into the sense direction and expressed from the EF1-α promoter.

2.8.2 *In vitro* characterization

HEK293 cells (ATCC) were cultured in IMDM (Invitrogen) and 10% FBS (Hyclone) in the presence of gentamycin (Invitrogen). *In vitro* transduction of HEK293 cells with AAV DIO ChR2-mCherry was performed with a serial dilution of viral particles. Cell transfections were performed 7 days later using Lipofectamine 2000 according to manufacturer´s instructions (Invitrogen). For induction of recombination, cells were co-transfected with one plasmid expressing EGFP and one plasmid expressing Cre recombinase in 1:3 ratio. Control cells transduced with virus were transfected with an EGFP expressing plasmid alone. Expression of membrane targeted ChR2-mCherry was scored in an inverted epifluorescent microscope (Nikon) 3 days later.

2.8.3 Extracellular Recordings

Tetrodes and stereotrodes were made from four or two twisted Formvar-coated Tungsten wires (California Fine Wire Company, Grover Beach, CA), respectively, of 12.5 μm diameter each. Online spike discrimination and data acquisition used the Cheetah data acquisition software (Neuralynx, Bozeman MT). Units were hand-separated post-hoc using manual cluster-cutting software (SpikeSort3D, Neuralynx). Cross correlation analysis was used to confirm unit separation. Units that were not easily separable were discarded. Local field potentials were recorded with open filters; units were recorded from data filtered from 600-9000 Hz. All data was sampled at 30kHz.

Spike waveforms of RS and FS cells were characterized, as shown in the examples below, by measuring (1) the ratio between the amplitude of the initial peak (*a*) to the following trough (*b*)

and (2) the duration of the spike at half height (*c*). Dotted line indicates mean baseline level in the absence of spikes.

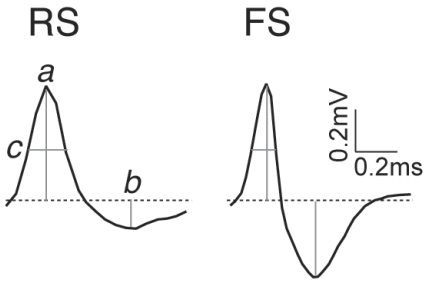

FS and RS spikes were significantly different in both mean spike duration at half height (FS 163.1 ± 3.2 μs, RS 262.4 ± 4.2 μs; unpaired t-test, $p < 0.001$) and peak:trough ratio (FS 1.3 ± 0.03, RS 2.2 ± 0.1; unpaired t-test, $p < 0.001$).

The latency to light-activated FS spikes (median spike latency: Low Power 2.5 ± 0.4 ms, High Power 1.1 ± 0.1 ms; black circles) agreed well with the onset latency of the resulting IPSPs (median onset latency: Low Power 3.2 ± 0.3 ms, High Power 1.6 ± 0.1 ms; open circles). The IPSP time to peak decreased with increasing power (time to peak: Low Power 16.3 ± 1.3 ms, High Power 5.4 ± 0.4 ms; unpaired t-test, $p < 0.05$). Low Power: 3 mW/mm^2, High Power: 8 mW/mm^2.

2.8.4 Whole-Cell Recordings

Electrodes (5-7MOhm resistance) were pulled on a Sutter P-97 and filled with internal patch solution (130 mM K-Gluconate, 4 mM KCl, 2 mM NaCl, 10 mM Hepes, 0.2 mM EGTA, 10 mM Phosphocreatine, 4 mM MgATP, 0.3 mM Na3GTP, adjusted to pH 7.25 with KOH and 292 mOsm with ddH2O). Electrodes were lowered under positive pressure while injecting small amplitude current pulses. After formation of a gigaseal, the cell membrane was broken and the whole-cell recording configuration achieved (MultiClamp 700B, Molecular Devices, Sunnyvale CA). After establishing a stable recording, a series of light pulses (1 and 10 ms duration at 3 and 8 mW/mm^2) were presented to evoke FS activity and subsequent IPSPs. In addition, small current pulses were given to measure input resistance, leak conductance (g_L), and leak reversal potential (E_L), and membrane capacitance (C_m). All recordings were stable, with a membrane potential <60mV and steady input resistance. Mean baseline input resistance was 81 ± 16.7 MΩ.

The synaptic reversal potential E_{syn} at the peak of the light-evoked IPSP was calculated as follows. The membrane equation states that the capacitive current in the cell is equal to the sum of all other currents (leak, synaptic and injected):

$C_m * dV_m/dt = g_L * (E_L - V_m) + g_{syn} * (E_{syn} - V_m) + I_{inj}$.

In this equation, the synaptic conductance g_{syn} includes both excitatory and inhibitory conductances and the synaptic reversal potential E_{syn} is a weighted sum of the excitatory and inhibitory reversals. This equation can be rewritten to solve for the synaptic current:

$I_{syn} = g_{syn} * (E_{syn} - V_m) = dV_m/dt * C_m - g_L * (E_L - V_m) - I_{inj}$.

The right-hand side of this equation can be calculated from experimental data. The membrane potential and its derivative, as well as the injected current, are directly given. Membrane capacitance (C_m), leak conductance (g_L), and leak reversal potential (E_L) were estimated based on response to hyperpolarizing current pulses. According to this equation, the synaptic current I_{syn} is linear in the membrane potential V_m. Because of natural fluctuations in the membrane potential during repeated stimulations, injecting varying levels of current I_{inj} yields a V-I plot. Since I_{syn} is zero if $V_m = E_{syn}$, the synaptic reversal potential can be calculated as the voltage where the best line fit intersects with the x-axis.

2.8.5 Broadband Light Stimulation

For broadband light stimulation we gave 3 sec bouts of 1ms light pulses at frequencies randomly selected from an even distribution 5-200 Hz.

2.8.6 Pharmacology

Baseline LFP and FS spike responses to 40 Hz light stimulation were recorded. The AMPA receptor blocker NBQX and the NMDA receptor APV were then each applied at 50 μM to the surface of the cortex for one hour, after which LFP and spike responses were again characterized. The GABAa receptor blocker picrotoxin was then applied at 50 μM in combination with the NBQX and APV. After an additional hour, LFP and spike responses were again characterized.

Chapter 3:

What do we gain from gamma? Local dynamic gain modulation drives enhanced efficacy and efficiency of signal transmission

This chapter has previously been published as:
Ulf Knoblich, Joshua H. Siegle, Dominique L. Pritchett, Christopher I. Moore (2010). What do we gain from gamma? Local dynamic gain modulation drives enhanced efficacy and efficiency of signal transmission. Front. Hum. Neurosci. 4:185. doi: 10.3389/fnhum.2010.00185

3.1 Abstract

Gamma oscillations in neocortex are hypothesized to improve information transmission between groups of neurons. We recently showed that optogenetic drive of fast-spiking interneurons (FS) at 40 Hz in mouse neocortex *in vivo* modulates the spike count and precision of sensory evoked responses. At specific phases of alignment between stimuli and FS activation, total evoked spike count was unchanged compared to baseline, but precision was increased. In the present study, we used computational modeling to investigate the origin of these local transformations, and to make predictions about their impact on downstream signal transmission. We replicated the prior experimental findings, and found that the local gain observed can be explained by mutual inhibition of fast-spiking interneurons, leading to more robust sensory-driven spiking in a brief temporal window post-stimulus, increasing local synchrony. Enhanced spiking in a second neocortical area, without a net increase in overall driven spikes in the first area, resulted from faster depolarization of target neurons due to increased presynaptic synchrony. In addition, we found that the precise temporal structure of spiking in the first area impacted the gain between cortical areas. The optimal spike distribution matched the "window of opportunity" defined by the timing of inhibition in the target area: spiking beyond this window did not contribute to downstream spike generation, leading to decreased overall gain. This result predicts that efficient transmission between neocortical areas requires a mechanism to dynamically match the temporal structure of the output of one area to the timing of inhibition in the recipient zone.

3.2 Introduction

Cortical oscillations in the gamma range (30-80 Hz) have been observed in numerous brain regions in a variety of species (Gray and Singer, 1989; Engel et al., 1991; Ribary et al., 1991; Maldonado et al., 2000; Nase et al., 2003), and during a wide range of behavioral states, from attentive wakefulness to REM sleep (Maloney et al., 1997; Gruber et al., 1999). The appearance of gamma at specific times relative to task performance implicates these rhythms in sensory processing, perceptual binding, memory formation, and conscious experience (Tallon-Baudry et al., 1997; Tallon-Baudry and Bertrand, 1999; Fries et al., 2001; Womelsdorf et al., 2006; Jensen et al., 2007; Fries, 2009; Gregoriou et al., 2009). However, the correlation between gamma expression and enhanced processing is nevertheless a debated issue, particularly in primary sensory neocortex (Chalk et al., 2010). In apparent contrast to the diversity of conditions

under which gamma has been detected, studies performed *in vitro*, *in vivo*, and *in silico* point to a unifying mechanism for gamma: volleys of alternating inhibition and excitation between parvalbumin-positive fast-spiking interneurons and pyramidal cells (Freeman, 1968; Wang and Buzsáki, 1996; Fisahn et al., 1998; Whittington et al., 2000; Traub et al., 2005; Bartos et al., 2007; Börgers et al., 2008; Börgers and Kopell, 2008; Atallah and Scanziani, 2009; Cardin et al., 2009; Paik et al., 2009); but see also (Galán et al., 2006). If gamma-range oscillations enhance signal processing, their common mechanism may reflect an essential temporal structure in the functioning of neural circuits.

To move beyond assertions based in correlation and directly test the hypothesis that the precise spike timing brought about by gamma oscillations enhances intracortical communication, it is necessary to bring this oscillation under experimental control. Enforcing temporal precision within a local network will require interventions that are somewhat artificial, but which are essential for understanding the benefits of gamma. In a recent study, Cardin et al. (2009) used optical stimulation to drive parvalbumin-positive neurons in the gamma frequency range, inducing network effects that mimic physiological gamma. When punctate sensory stimuli (brief vibrissa deflections) were presented, the precise timing of inhibition relative to sensory input altered the evoked response. For certain delays, the overall number of spikes was reduced, indicating gamma can change the input gain of a region. For other delays, rhythmic inhibition did not decrease the total number of spikes, but did cause spiking to occur in a more compressed temporal window, increasing the synchrony of the evoked response.

In considering dynamics in rate coding, a fundamental question is the value that an action potential (or a fixed number of action potentials) has in generating firing in a downstream area. Central to this question of gain modulation is whether the same number of spikes in a local area can generate a greater number of spikes in a target area, enhancing the *efficacy* of signal transmission. Synchrony is often cited as a potential mechanism for increasing the value of a given spike rate in a local area (König et al., 1996; Azouz and Gray, 2000; Pinto et al., 2000; Azouz and Gray, 2003; Börgers and Kopell, 2005; Bruno and Sakmann, 2006; Wang et al., 2010), though relatively little direct experimental evidence has been offered for this idea.

Presuming efficacy can be modulated, we can begin to explore the boundaries on this improvement in transmission. For example, it is important to know the limit beyond which firing in the local area cannot be further optimized, leading to diminishing returns when more local

spikes are added. We refer to this as the *efficiency* of transmission, as additional, less useful spikes would reflect "wasted" effort of the presynaptic area.

Using a computational model consisting of 4488 neurons with realistic Hodgkin-Huxley biophysics, we addressed three questions regarding neural gain and gamma posed by the Cardin et al. (2009) findings. First, we delineated a potential local network mechanism that can explain the local gain change observed, i.e. the increased firing rate during the early part of the response at specific phases of alignment between sensory stimulus and gamma cycle. Second, we asked how an imposed gamma oscillation can impact the efficacy of signal transmission, and third, how it may impact its efficiency. Though the oscillations induced in our network (and in Cardin et al., 2009) lack the spatial and temporal flexibility of natural rhythms, they are a potentially powerful tool for probing the importance of spike timing in intracortical communication. Limitations of this approach in general and specific ways that it is non-natural are presented in the Discussion.

We found, in agreement with previous suggestions, that a sharper onset in the rate of presynaptic spiking enhanced the *efficacy* of signal transmission. We further found that spiking *efficiency* was crucially dependent on the shape of the sensory evoked "spike packet," defined as local spikes within a temporal window on the scale of a single cycle of gamma (see Tiesinga and Sejnowski, 2009 for explication of a similar term, "spike volleys"). Under model conditions in which the recipient neocortical area exhibited strong recurrent inhibition, spiking beyond the gamma-defined window did not contribute to additional downstream activation, decreasing the net gain between areas. Given that such conditions are observed during enhanced attention and arousal and during processing of naturalistic stimuli, these findings suggest a fundamental time scale for the effective transmission of signals through the neocortex during active sensory processing.

3.3 Materials and Methods

The model was organized in a sequence of three processing stages. An input stage (I) provided excitatory feed-forward input (simulating a sensory stimulus) to the first processing stage (X1), which is the site of "optical" modulation, and the output of X1 was fed into the second processing stage (X2). Both processing stages were identical except for the strength of recurrent

inhibition. In addition, a separate stage (B) provided both excitatory and inhibitory background input to simulate individual variability of each neuron in cortex.

The input and background stages were modeled as spike generators without further processing. Each processing stage consisted of pyramidal cells (P) and fast-spiking inhibitory cells (FS). Both cell types received inputs from the P cells of the previous stage, and made local connections with both cells types within each stage.

Each stage contained 1024 pyramidal cells and each processing stage also contained 196 fast-spiking interneurons, approximating the cortical proportions of these different cell types (Markram et al., 2004). The time constants for P and FS cells were tuned to approximate the physiological properties of pyramidal cells and fast-spiking interneurons, respectively.

3.3.1 Cell models

Input (B and I) cells were modeled as independent variable rate Poisson process spike generators with a time step of 100 μs.

Pyramidal (P) cells had a single somatic compartment with six attached dendritic compartments. The somatic compartment was based on the single compartment Hodgkin-Huxley type model (Golomb and Amitai, 1997), and adapted to include additional dendritic compartments. The membrane potential was determined by the membrane equation summing currents from different intrinsic currents through channels present in the membrane with synaptic and injected currents.

For the soma:

$$C_m \frac{dV_m}{dt} = I_L + I_{Na} + I_{NaP} + I_{KDr} + I_{Ka} + I_{Ks} + I_{syn} + I_{inj}$$

C_m = 1.5 μF/cm^2.

Leak current:

$$I_L = g_L(E_L - V_m)$$

g_L = 0.20 mS/cm^2, E_L = -65 mV.

Fast sodium channels:

$$I_{Na} = g_{Na}(E_{Na} - V_m)m^3 h$$

$$m = m_\infty = \frac{1}{1 + e^{-\frac{V_m - \theta_m}{\sigma_m}}}$$

$$h_\infty = \frac{1}{1 + e^{-\frac{V_m - \theta_h}{\sigma_h}}}$$

$$\tau_h = 0.37 + \frac{2.78}{1 + e^{-\frac{V_m - \theta_{ht}}{\sigma_{ht}}}}$$

$$\frac{dh}{dt} = \frac{h_\infty - h}{\tau_h}$$

g_{Na} = 53 mS/cm^2, E_{Na} = 55 mV, θ_m = -30.0 mV, σ_m = 9.5 mV, θ_h = -53.0 mV, σ_h = -7.0 mV, θ_{ht} = -40.5 mV, σ_{ht} = -6.0 mV.

Persistent sodium channels:

$$I_{NaP} = g_{NaP}(E_{Na} - V_m)p$$

$$p = p_\infty = \frac{1}{1 + e^{-\frac{V_m - \theta_p}{\sigma_p}}},$$

g_{NaP} = 0.15 mS/cm^2, E_{Na} = 55 mV, θ_p = -40.0 mV, σ_m = 5.0 mV.

Delayed rectifier potassium channels:

$$I_{KDr} = g_{KDr}(E_K - V_m)n^4$$

$$n_\infty = \frac{1}{1 + e^{-\frac{V_m - \theta_n}{\sigma_n}}}$$

$$\tau_n = 0.37 + \frac{1.85}{1 + e^{-\frac{V_m - \theta_{nt}}{\sigma_{nt}}}}$$

$$\frac{dn}{dt} = \frac{n_\infty - n}{\tau_n}$$

g_{KDr} = 6.6 mS/cm^2, E_K = -90 mV, θ_n = -30.0 mV, σ_n = 10.0 mV, θ_{nt} = -27.0 mV, σ_{nt} = -15.0 mV.

A-type potassium channels:

$$I_{Ka} = g_{Ka}\left(E_K - V_m\right)a^3 b$$

$$a = a_\infty = \frac{1}{1 + e^{-\frac{V_m - \theta_a}{\sigma_a}}}$$

$$b_\infty = \frac{1}{1 + e^{-\frac{V_m - \theta_b}{\sigma_b}}}$$

$$\frac{db}{dt} = \frac{b_\infty - b}{\tau_b}$$

g_{Ka} = 4.6 mS/cm^2, E_K = -90 mV, θ_a = -50.0 mV, σ_a = 20.0 mV, θ_b = -80.0 mV, σ_b = 6.0 mV, τ_b=15.0 ms.

Slow potassium channels:

$$I_{Ks} = g_{Ks}\left(E_K - V_m\right)z$$

$$z_\infty = \frac{1}{1 + e^{-\frac{V_m - \theta_z}{\sigma_z}}}$$

$$\frac{dz}{dt} = \frac{z_\infty - z}{\tau_z}$$

g_{Ks} = 0.88 mS/cm^2, E_K = -90 mV, θ_z = -39.0 mV, σ_z = 5.0 mV, τ_b = 75.0 ms.

Synaptic currents:

$$I_{syn} = g_{syn}\left(E_{syn} - V_m\right)$$

E_{AMPA} = 0 mV, E_{GABAA} = -80 mV.

The dendrites were modeled analogously but only contained passive (leak) channels.

Fast-spiking cells show different properties including fast spikes, higher firing rates, lack of spike rate adaptation (Beierlein et al., 2003; Ma et al., 2006; Caputi et al., 2008) and were modeled as single compartments after the Hodgkin-Huxley type equations in a previous model (Wang and Buzsáki, 1996):

$$C_m \frac{dV_m}{dt} = I_L + I_{Na} + I_{KDr} + I_{syn} + I_{inj}$$

C_m = 1.5 μF/cm^2.

Leak current:

$$I_L = g_L(E_L - V_m)$$

g_L = 0.40 mS/cm^2, E_L = -70 mV.

Fast sodium channels:

$$I_{Na} = g_{Na}(E_{Na} - V_m)m^3h$$

$$\alpha_m = \frac{-0.1 \cdot (V_m + 35)}{e^{-0.1 \cdot (V_m + 35)} - 1}$$

$$\beta_m = 4e^{-\frac{V_m + 60}{18}}$$

$$m = m_\infty = \frac{\alpha_m}{\alpha_m + \beta_m}$$

$$\alpha_h = 0.07e^{\frac{-(V_m + 58)}{20}}$$

$$\beta_h = \frac{1}{e^{-0.1(V_m + 28)} + 1}$$

$$\frac{dh}{dt} = 5(\alpha_h(1-h) - \beta_h h)$$

g_{Na} = 140.0 mS/cm^2, E_{Na} = 55 mV.

Delayed rectifier potassium channels:

$$I_{KDr} = g_{KDr}(E_K - V_m)n^4$$

$$\alpha_n = \frac{-0.1 \cdot (V_m + 34)}{e^{-0.1 \cdot (V_m + 34)} - 1}$$

$$\beta_n = 0.125 e^{-\frac{V_m + 44}{80}}$$

$$m = m_\infty = \frac{\alpha_m}{\alpha_m + \beta_m}$$

g_{KDr} = 36.0 mS/cm^2, E_K = -90 mV.

3.3.2 Synaptic dynamics

The model included two synapse types, excitatory AMPA synapses and inhibitory $GABA_A$ synapses. All synapses were modeled by kinetic models with two states representing the open and closed states of ion channels (Destexhe et al., 1994). The fraction of open channels for a synapse *r* increased with the rate constant α when neurotransmitter was present (*T* = 1 mM), and decreased with the dissociation rate β:

$$\frac{dr}{dt} = \alpha T(1-r) - \beta r$$

The total conductance *g* of a synapse was the product of its maximal conductance $\hat{g}$ and the fraction of open channels *r*. The rate constants for the different synapse types (Destexhe et al., 1994) were: AMPA synapses: α = 1.1 × 10^6 $M^{-1}s^{-1}$, β = 190 s^{-1}; $GABA_A$: α = 0.53 × 10^6 $M^{-1}s^{-1}$, β = 180 s^{-1}.

3.3.3 Connectivity

Synaptic connections were made such that each post-synaptic cell received input from presynaptic cells in a local environment. For a given post-synaptic cell, the probability of a synaptic connection with a pre-synaptic cell was determined by a Gaussian probability distribution with a width of 20% of the total model extent.

All excitatory synapses are modeled as AMPA synapses. Fast-spiking cells made $GABA_A$-ergic synapses onto the soma of pyramidal cells. The conductances within each stage were: g_{PP} = 0.56 nS, g_{PF} = 5.0 nS, g_{FF} = 20.0 nS, g_{F1P1} = 3.6 nS, g_{F2P2} = 14.4 nS and conductance values between stages were set to be: $g_{BP(e)}$ = 0.8 nS, $g_{BP(i)}$ = 1.2 nS, $g_{BF(e)}$ = 0.6 nS, $g_{BF(i)}$ = 0.48 nS, $g_{IP1} = g_{P1P2}$ = 15.0 nS, $g_{IF1} = g_{P1F2}$ = 0.4 nS.

3.3.4 Inputs

B and I cells were modeled as variable rate Poisson spike generators. For each B cell, the mean firing rate was fixed at 40 Hz throughout the simulation. Each cell in the processing stages received a random subset of these spike trains, each connected to either excitatory or inhibitory synapses, to mimic random background fluctuations in neocortical cells. The firing rate of I cells was varied with the stimulus. At the stimulus time, their rate was determined by a Gaussian profile with amplitude 250 Hz and width 2 ms, and they were otherwise silent.

To model light-activated stimulation of fast-spiking cells, we added a strong excitatory synapse to X1 FS cells. The kinetics of these channels were similar to those of channelrhodopsin-2 (Nagel et al., 2003; Boyden et al., 2005; Ishizuka et al., 2006), and their activation was triggered with a 1 ms “light” pulse instead of neurotransmitter as for chemical synapses. For the results presented here, half of all FS cells were “light-activated”. While there is no direct evidence for the fraction of cells activated in Cardin et al., this number is consistent with observations in these and other channelrhodopsin-2-expressing animals. In a version of these simulations in which all FS cells are light-activated, qualitatively similar results were observed, indicating that the observed effects are not critically dependent on the choice of this parameter.

The delay between light and “sensory” input was defined as the time between the onset of the “light pulse” and the time of peak of the I cell Gaussian firing rate profile, i.e. the median spike time of the input population spike packet.

3.3.5 Simulation environment and global parameters

All simulations were carried out using the CNS (Cortical Network Simulator (Mutch et al., 2010)) package written in Matlab (The Mathworks, Natick, MA) and C, running on custom PCs with an Nvidia GeForce GTX285 or GTX480 GPU (EVGA, Brea, CA). All differential equations were solved with the Crank-Nicolson method. The time step for intracellular and synaptic computations was 10 μs, inter-cellular spike-based communication was performed with a time step of 100 μs.

3.3.6 Analysis

Post-stimulus time histograms (PSTHs) were computed using a bin size of 2 ms. Total spike count was defined as the number of elicited spikes up to 50 ms after the stimulus. Synchrony was measured as the inter-quartile range of spikes times in the population during a single trial. Gain was defined as the ratio between the spike count in the target area and the spike count in the source area. Statistical significance of differences was assessed using an ANOVA with Dunnett's test for comparisons between different phases or delays and the baseline condition, and t-tests for comparisons between only two conditions.

3.4 Results

To investigate the mechanism of timing-dependent modulation of sensory responses observed in Cardin et al. (2009), we generated a large multi-stage neural network consisting of an input stage (I) and two processing stages (X1 and X2) (Figure 1). Each processing stage was organized as a two-dimensional layer of excitatory neurons and inhibitory interneurons. The input stage consisted of 1024 variable rate Poisson spike generators in a 32 x 32 grid. The processing stages were identical, each a 32 x 32 grid of pyramidal cells (P) interspersed with a 14 x 14 grid of fast-spiking interneurons (FS), modeled as Hodgkin-Huxley style multi- and single-compartment cells, respectively. Within each stage, both cell types received inputs from both cell types and connectivity was local, i.e. for a given post-synaptic neuron, the connection probability for each potential pre-synaptic neuron fell off with a Gaussian profile with a sigma equal to 20% of the extent of the entire layer. Both cell types also received input from pyramidal cells of the previous layer. In addition, each cell received a random sequence of excitatory and inhibitory synaptic inputs (driven by a random subset of 40 out of 1024 Poisson spike trains for each cell) to capture

variability between cortical cells. The synaptic weights were tuned to approximate basic properties of the anesthetized mouse primary somatosensory cortex in general and the results of Cardin et al. 2009 specifically. The latency from stimulus to X1 spike was 8-10 ms for most cells, matching *in vivo* latencies (Pinto et al., 2000), the difference of median spike times in X1 and X2 varied between 4 and 10 ms, depending on the number of spikes in X1. To model light-activated stimulation of fast-spiking cells, we added a strong excitatory synapse with activation kinetics paralleling those of channelrhodopsin-2, which were activated with a 1 ms "light" pulse (Nagel et al., 2003; Boyden et al., 2005; Ishizuka et al., 2006).

3.4.1 Local effects of synchronous inhibition

We first replicated the experimental data and investigated the local effects of synchronized inhibition in the affected area. Dissociating the contributions of pre- and post-stimulus inhibition, we then determined the mechanism for these effects.

3.4.1.1 The impact of repetitive induced inhibition on sensory evoked responses

To replicate the *in vivo* results, we activated X1 FS cells at a frequency of 40 Hz and gave a brief feed-forward stimulus from the input layer at varying phases (in 2 ms steps) between two light pulses (Figure 2A). Consistent with the experimental data, we observed modulation of X1 P activity in response to the stimulus that depended on the precise timing between stimulus and induced inhibition (Figure 2B). Responses to stimuli close to the time of induced inhibition were almost completely suppressed, while stimuli approximately half a period after the last light pulse (12-16 ms) elicited a comparable number of spikes in X1 P (Figure 2C). Spike synchrony was enhanced overall during induced inhibition, however, stimuli during the first half-period led to the strongest increases in synchrony (Figure 2D).

3.4.1.2 Isolated effects of pre- and post-stimulus inhibition in X1

Each stimulus was preceded and followed by a pulse of inhibition, suggesting that the mechanism(s) for the observed changes in response packet size and shape resulted from a linear or non-linear combination of the earlier and later inhibitory inputs. To isolate the contributions of pre- and post-stimulus inhibition, we employed a second paradigm in which a single inhibition-inducing light pulse was paired with a stimulus at varying delays from 25 ms to 1 ms pre-stimulus and 0 to 24 ms post-stimulus in 2 ms steps (Figure 2E). These values were chosen such

that for each delay in the pre-stimulus inhibition condition there was a corresponding value in the post-stimulus inhibition condition, effectively mapping onto the same phase in the repetitive inhibition experiment.

Pre- and post-stimulus inhibition conditions showed two distinct and opposite effects on the size and shape of the response packet in X1 (Figure 2F). Post-stimulus inhibition 25 ms after the stimulus did not have an appreciable effect on the response. Decreasing the stimulus latency preceding inhibition led to a gradual decrease in the number of elicited spikes. Delays of 10-14 ms only suppressed the latter part of the response packet in X1, leaving the first part virtually unchanged. This sculpting of evoked spikes led to significant changes in synchrony ($p < 0.01$), but no significant decrease in spike count (Figure 2G and H). For shorter delays, inhibition reached the P cells early enough to cause significant suppression ($p < 0.01$). Inhibition immediately before the stimulus (16-24 ms) led to almost complete suppression of the X1 response ($p < 0.01$), similar to inhibition immediately afterwards (0-4 ms). As the post-stimulus delay was increased to 12-20 ms, the response became elevated throughout the response period ($p < 0.01$). This response potentiation peaked at a delay of 14 ms and then decreased again, returning to the baseline response as the delay was further increased beyond 20 ms (Figure 2F-H).

3.4.1.3 Prediction of the impact of repetitive inhibition from isolated inhibition

We hypothesized that the impact of repetitive inhibition could be explained by linear combination of the effects of pre- and post-stimulus inhibition. To test this prediction, we computed a modulation kernel for each delay from the single inhibition responses by normalizing the corresponding PSTH by the baseline PSTH. For a given kernel, the value in each bin was the ratio between the response during the delay condition and the response during the baseline condition, representing the impact of this condition on that particular time bin. If the number of spikes was unchanged, the kernel value was 1, if all spikes were suppressed, the value was 0. Because the delays were chosen to map onto the same phase in the repetitive inhibition case, the equivalent kernel representing the combined effect of pre- and post-stimulus inhibition can be derived by simply multiplying the two corresponding kernels.

Applying these combined kernels from each phase of the repetitive inhibition to the baseline response predicted the size and shape of the actual responses (Figure 3A). Thus, the effect of

repetitive inhibition on a sensory response in X1 was captured by the combined effect of the inhibition immediately preceding and following the stimulus. During the middle phases, the pre-stimulation inhibition caused an overall boost across the response packet and the post-stimulus inhibition suppressed the late spikes, effectively creating a more synchronous packet of approximately equal size compared to the baseline response. Given that our initial simulations showed the same local effects on rate and synchrony in X1 as the experimental data (Cardin et al., 2009), these results suggest that further mechanisms, beyond the impact of repeated events of inhibition, need not be invoked to explain the "gamma" dependent gain observed.

3.4.1.4 Biophysical mechanism of response elevation

While suppression by post-stimulus inhibition has a straightforward explanation, the cause of increased spiking in response to a stimulus approximately 10 ms after light stimulation is not intuitive. To understand the mechanism underlying this phenomenon, we investigated the sub- and supra-threshold responses of P and FS cells in the network. Under baseline conditions, due to their strong inputs and fast membrane kinetics, FS cells fired a population spike at short latency after the onset of the incoming sensory input while the incoming excitatory post-synaptic potential (PSP) in P cells was still rising (Figure 3B). This population spike caused an inhibitory PSP in the P cells that reduced the slope and amplitude of the resulting compound PSP (Figure 3C). Comparing the early and late phase of the rising compound PSP in X1 P, the IPSP reduced the slope by more than 60% (Figure 3D, left). As soon as P cells did fire, strong recurrent connections from P onto FS cells caused a secondary FS response, restoring the balance between excitation and inhibition.

In the pre-stimulus inhibition condition, light-activating FS cells in the model also caused a strong IPSP in FS cells. The resulting hyper-polarization and increased conductance in these cells suppressed their initial sensory driven response, causing the EPSP in the P cells to proceed without interference from an early IPSP (Figure 3B-D, right). Without the contribution of perisomatic inhibitory synapses, a more depolarized membrane potential and higher PSP slope were observed, both of which predict a higher spike probability (Azouz and Gray, 2000). Because of the earlier IPSP caused by the light-induced FS activation, the starting membrane potential for P cells was slightly more hyperpolarized compared to baseline, causing an increase in latency of spike onset and stronger synchronization, also consistent with experimental data

(see Figure 4, Cardin et al., 2009). As soon as P cell spiking started, FS cell spiking increased, similar to the baseline case. These results provide a biophysical mechanism for the modulation of size and shape of the X1 population response due to induced FS-to-FS inhibition.

To test whether this mutual inhibition mechanism is necessary for the response enhancement, we created a model variant lacking the underlying inhibitory FS-FS synapses. As expected from the lack of mutual FS inhibition, early feed-forward driven FS spikes were not affected by light stimulation (Figure 3E). The P cell spiking was strongly reduced, consistent with the hyperpolarizing effect of the earlier light-induced IPSP in combination with unchanged feed-forward inhibition. Subsequently, late FS spiking driven by P activity was reduced, as well. The spike count for post-stimulus inhibition conditions in this model variant was similar to the original model (Figure 3F, compare to Figure 2G). However, almost all pre-stimulus inhibition conditions showed significant suppression, and the enhanced spike count for several pre-stimulus inhibition conditions found in the original model was completely abolished, supporting the crucial role of mutual FS inhibition for this enhancement mechanism.

3.4.2 Impact of the response packet shape on downstream *efficacy*

We investigated the impact of these changes in the X1 response size and shape on the efficacy in driving responses in a downstream target area (X2). As expected, the number of spikes elicited in X2 in the repetitive inhibition paradigm closely followed the spike count in X1 (Figure 4A and B). Phases close to an inhibitory pulse (0-4 and 20-24 ms) exhibited decreased gains compared to baseline ($p < 0.01$), explained by the much lower X1 firing rates under these conditions (Figure 4C, $p < 0.01$). Intermediate delays (12-16 ms), however, while matching the X1 spike count of the baseline condition, had significantly higher X2 spike counts ($p < 0.01$), resulting in a significantly higher X2 gain ($p < 0.01$).

In contrast to X1 spike count, which did not consistently exceed baseline levels, X1 spike synchrony values were significantly changed during the intermediate phases (2-14 ms, $p < 0.01$), suggesting this shift was causal in the increased gain. The sub- and supra-threshold responses of both cell types in X2 support such a mechanism. FS and P cells in X2 exhibited similar response packet shapes during baseline and delay conditions, but elevated counts during the delay condition (Figure 4D, left). The average P cell membrane potential revealed a 50% higher PSP slope (Figure 4E and F). This steeper slope was driven by the larger number of coincident X1

spikes during the early phase of the X1 spike packet. Due to this increased slope, more cells were able to fire spikes before the IPSP from the FS cells started to suppress the P cells, leading to a stronger and more synchronous response.

3.4.3 Impact of response packet shape on downstream *efficiency*

During the single pulse post-stimulus inhibition condition, X2 gain was only weakly modulated for all delays, despite the fact that at least as many spikes were driven as in the baseline response (Figure 4G-I). Comparing the 12 ms delay response for the single pulse inhibition to the corresponding latency from the repetitive inhibition condition reveals that FS and P cells in X2 exhibited sub- and supra-threshold responses (Figure 4J-L) that are nearly equivalent to the repetitive inhibition condition, despite different X1 responses.

To understand the difference in X2 gain despite the virtually equivalent spike count in X2 (78 vs. 72 spikes, Figure 5A), we analyzed the temporal structure of the two X1 response packets. Compared to the repetitive inhibition condition, the X1 response in the single post-stimulus inhibition condition was similar during the first 10 ms, but contained more late spikes (158 vs. 109 spikes). The single inhibition X1 response contained a large number of spikes during and after the conclusion of most X2 firing. The impact of these late X1 spikes on X2 was reduced by an IPSP from X2 FS cells.

To quantify the impact of spikes during different parts of the X1 response packet, we performed simulations that exactly replicated the conditions used to produce the responses in Figure 4A, with the only difference being that a tenth of X1 spikes were deleted. In each run, all the spikes from a different one of the ten deciles were deleted, and we determined the size of the X2 response for each of these deletions. This analysis revealed that deletion of spikes during the first 10 ms of the X1 response had the strongest impact on X2 spike count. In contrast, spikes later than 10 ms after the response onset had almost no impact (Figure 5B). To confirm this result, we performed another deletion experiment in which we erased all spikes 10 ms or later after response onset. Indeed, now X1 responses were comparable in shape in both conditions, and X2 responses were identical.

These results revealed that the precise temporal structure of a spike packet not only influenced its efficacy in driving X2 responses, but also its efficiency in eliciting downstream responses, both

determinants of gain. Beyond a specific window determined by the timing of inhibition in the target region, X1 spikes had no net gain and were essentially extraneous to signal relay.

3.5 Discussion

We will first discuss our results on the local effects of repetitive inhibition, followed by the resulting changes in efficacy and efficiency. We conclude with a discussion of how our results relate to intrinsically generated gamma.

3.5.1 Local effects of repetitive inhibition

We have identified opposing contributions of pre- and post-stimulus inhibition to the enhancement of spike count and synchrony for the optimal phase delay between stimulus and inhibition. While post-stimulus inhibition cuts off late spikes, and thus increases synchrony of the population response, pre-stimulus inhibition causes an overall increase in spiking, particularly during the early phase of the response, by FS-to-FS inhibition. In combination, these effects lead to the observed strong increase in synchrony while maintaining or only moderately increasing spike count. This finding is in alignment with several previous experimental and computational studies reporting similar effects under conditions of natural, intrinsically generated gamma oscillations *in vitro*, *in vivo* and *in silico* (Burchell et al., 1998; Pouille and Scanziani, 2001; Fries et al., 2001; Börgers et al., 2005; Womelsdorf et al., 2006; Fries et al., 2008).

The computational benefit of gamma has been described as synchronizing spikes within a local population without changing the overall number of spikes, effectively creating a sequence of impactful spike packets interspersed with brief periods of relative silence, in contrast to a continuous stream of spikes without temporal structure. This view implies that each gamma cycle can be viewed as a separate "window of opportunity" (Pinto et al., 2000; Wehr and Zador, 2003; Hasenstaub et al., 2005; Wilent and Contreras, 2005), similar to the mechanisms controlling the transient imbalance of excitation and inhibition in response to a brief sensory stimulus. Mechanistic explanations of gamma-related redistribution of spikes have focused on the effect of the rhythmic inhibitory post-synaptic potentials in pyramidal cells suppressing spikes or delaying spiking in response to a sustained stimulus, leading to a compression of spike times into a shorter window and thus increased synchrony (Whittington et al., 2000; Tiesinga and

Sejnowski, 2009; Börgers and Kopell, 2003). Our results indicate that the mutual suppression of FS cells could also play an important role in modulating the gain in the local network, regardless of whether gamma is created by a PING or ING mechanism (Whittington et al., 2000; Tiesinga and Sejnowski, 2009). This finding is consistent with the result that a transient increase in excitation is accompanied by a synchronized decrease in inhibition in cat V1 neurons (Azouz and Gray, 2008).

3.5.2 Spike synchrony and downstream efficacy

We found that the synchrony of spikes in a population packet, particularly during the onset of a response, had a profound impact on the size of the downstream response, in agreement with previous computational and experimental studies (König et al., 1996; Azouz and Gray, 2000; Pinto et al., 2000; Azouz and Gray, 2003; Börgers and Kopell, 2005; Bruno and Sakmann, 2006; Womelsdorf et al., 2007; Wang et al., 2010). Taking into account the correlation between attention and gamma band activity (Fries et al., 2001; Börgers et al., 2005; Womelsdorf et al., 2006; Roy et al., 2007; Börgers et al., 2008; Fries et al., 2008), these findings support the view that attention might act by increasing synchrony among local ensembles of neurons and thus selectively enhancing their impact on a target area, effectively increasing signal-to-noise without large increases in average spike rate (Steinmetz et al., 2000; Fries et al., 2001; Buia and Tiesinga, 2006; Fries et al., 2008).

3.5.3 Packet shape and downstream efficiency

In contrast to the efficacy of a spike packet, which was mostly determined by the early phase, its efficiency was determined by firing in the late phase, i.e. its length. If a packet was too long, late spikes arrived at the downstream circuit after inhibition had set in and thus had diminished impact, decreasing overall packet gain. Thus, a key benefit of repetitive inhibition, as in the case of gamma, is optimal packet length controlled by post-stimulus inhibition, determined by the time between two inhibitory events.

Given the dependence of downstream inhibition on the strength of activity in a presynaptic source, our results imply a close connection between early efficacy and the most efficient packet size. To maintain maximal efficiency, packet length needs to be dynamically adjusted to the spike count at the beginning of the packet. If activity is low in the presynaptic input, inhibition

will also be more weakly recruited, and a longer packet length will show greater efficiency. In contrast, in the conditions of the current experiment, narrower temporal windows are optimal. This prediction is consistent with several theoretical and experimental studies showing excitatory integration during weak stimulus presentation, and stronger relative inhibition during strong drive (Somers et al., 1998; Moore et al., 1999).

While there is considerable debate over the contribution of different processes to the total energy consumption of the brain (Attwell and Iadecola, 2002), spiking and evoked pre- and postsynaptic activity are believed to account for a significant fraction of total metabolic demand. It has been argued (Laughlin and Sejnowski, 2003) that energy consumption constrains neural activity and that the brain has developed mechanisms to maintain the optimal balance between transmitted information and energetic cost. Thus it is possible that one of the functions of gamma, and the redundancy in mechanisms leading to its emergence, is to sustain this efficiency across large networks by optimizing spike timing.

3.5.4 Implications for intrinsically generated gamma

Although our ultimate goal is to understand the mechanism and function of gamma in natural circuits, the premises of our study deviate from intrinsic *in vivo* gamma in two crucial ways.

First, and maybe most importantly, repetitive inhibition was induced artificially in our optogenetic study and in this model, in contrast to intrinsically generated inhibition during states of gamma activity. This manipulation allowed us to dissociate excitation and inhibition temporally, to understand the mechanisms underlying the link between them during natural gamma activity. A consequence of the independent control of inhibitory activity is the disruption of self-regulatory and adaptive mechanisms controlling the interplay between excitation and inhibition. During natural gamma, the spatial and temporal distribution of inhibitory activity is much less rigid and more adaptive to the contextual network activity. Considering the link between stimulus strength or discrimination performance and gamma frequency (Edden et al., 2009), it is possible that one of the functions of intrinsically generated gamma activity is to ensure the match between output packet shape and timing of inhibition in the target area that we have found to be necessary for optimally efficient transmission.

Second, we used punctate stimuli instead of more natural/naturalistic stimuli that are sustained for several hundreds of milliseconds. Further, the impact of this stimulus was modeled as a

discrete input with relatively brief temporal consequences, in contrast to the sustained activity patterns that can be observed following some punctate stimuli (Metherate and Cruikshank, 1999). Following the view that gamma essentially creates a sequence of windows of opportunity, our results can be interpreted as describing one of these windows embedded in an ongoing sequence. The extent to which this prediction holds, and where the effects and mechanisms applicable during ongoing ensemble activity deviate from our findings, will need to be tested in future studies, both *in silico* and *in vivo*. Due to the availability of a wealth of optogenetic tools (Chow et al., 2010; Gradinaru et al., 2010), the majority of predictions we have made can be feasibly tested in the near future.

Using a detailed large-scale biophysical model, we have demonstrated a mechanism for sensory response gain modulation. Precisely timed inhibition in a given neocortical area altered the size and shape of its population spike packet, and these differences impacted the efficacy and efficiency of transmission of this signal to a downstream neocortical area. In a subset of conditions, local synchronized inhibition increased the gain of transmission, allowing fewer spikes to have a larger impact. This modulation in gain was limited to spiking added in an initial temporal window, the addition of later spikes did not impact downstream firing. Thus, gamma-range inhibition changes the shape of the local response packet to optimize both its efficacy and its efficiency.

3.6 References

Atallah, B. V., Scanziani, M., 2009. Instantaneous modulation of gamma oscillation frequency by balancing excitation with inhibition. Neuron 62 (4), 566–577.

Attwell, D., Iadecola, C., 2002. The neural basis of functional brain imaging signals. Trends Neurosci. 25 (12), 621–625.

Azouz, R., Gray, C. M., 2000. Dynamic spike threshold reveals a mechanism for synaptic coincidence detection in cortical neurons in vivo. Proc. Natl. Acad. Sci. U.S.A. 97 (14), 8110–8115.

Azouz, R., Gray, C. M., 2003. Adaptive coincidence detection and dynamic gain control in visual cortical neurons in vivo. Neuron 37 (3), 513–523.

Azouz, R., Gray, C. M., 2008. Stimulus-selective spiking is driven by the relative timing of synchronous excitation and disinhibition in cat striate neurons in vivo. Eur. J. Neurosci. 28 (7), 1286–1300.

Bartos, M., Vida, I., Jonas, P., 2007. Synaptic mechanisms of synchronized gamma oscillations in inhibitory interneuron networks. Nat. Rev. Neurosci. 8 (1), 45–56.

Beierlein, M., Gibson, J. R., Connors, B. W., 2003. Two dynamically distinct inhibitory networks in layer 4 of the neocortex. J. Neurophysiol. 90 (5), 2987–3000.

Börgers, C., Epstein, S., Kopell, N. J., 2005. Background gamma rhythmicity and attention in cortical local circuits: a computational study. Proc. Natl. Acad. Sci. U.S.A. 102 (19), 7002–7007.

Börgers, C., Epstein, S., Kopell, N. J., 2008. Gamma oscillations mediate stimulus competition and attentional selection in a cortical network model. Proc. Natl. Acad. Sci. U.S.A. 105 (46), 18023–18028.

Börgers, C., Kopell, N. J., 2003. Synchronization in networks of excitatory and inhibitory neurons with sparse, random connectivity. Neural Comput. 15 (3), 509–538.

Börgers, C., Kopell, N. J., 2005. Effects of noisy drive on rhythms in networks of excitatory and inhibitory neurons. Neural Comput. 17 (3), 557–608.

Börgers, C., Kopell, N. J., 2008. Gamma oscillations and stimulus selection. Neural Comput. 20 (2), 383–414.

Boyden, E. S., Zhang, F., Bamberg, E., Nagel, G., Deisseroth, K., 2005. Millisecond-timescale, genetically targeted optical control of neural activity. Nat. Neurosci. 8 (9), 1263–1268.

Bruno, R. M., Sakmann, B., 2006. Cortex is driven by weak but synchronously active thalamocortical synapses. Science 312 (5780), 1622–1627.

Buia, C. I., Tiesinga, P. H., 2006. Attentional modulation of firing rate and synchrony in a model cortical network. J. Comput. Neurosci. 20 (3), 247–264.

Burchell, T. R., Faulkner, H. J., Whittington, M. A., 1998. Gamma frequency oscillations gate temporally coded afferent inputs in the rat hippocampal slice. Neurosci. Lett. 255 (3), 151–154.

Caputi, A., Rozov, A., Blatow, M., Monyer, H., 2008. Two Calretinin-Positive GABAergic Cell Types in Layer 2/3 of the Mouse Neocortex Provide Different Forms of Inhibition. Cereb. Cortex 19 (6), 1345–1359.

Cardin, J. A., Carlén, M., Meletis, K., Knoblich, U., Zhang, F., Deisseroth, K., Tsai, L.-H., Moore, C. I., 2009. Driving fast-spiking cells induces gamma rhythm and controls sensory responses. Nature 459 (7247), 663–667.

Chalk, M., Herrero, J. L., Gieselmann, M. A., Delicato, L. S., Gotthardt, S., Thiele, A., 2010. Attention reduces stimulus-driven gamma frequency oscillations and spike field coherence in V1. Neuron 66 (1), 114–125.

Chow, B. Y., Han, X., Dobry, A. S., Qian, X., Chuong, A. S., Li, M., Henninger, M. A., Belfort, G. M., Lin, Y., Monahan, P. E., Boyden, E. S., 2010. High-performance genetically targetable optical neural silencing by light-driven proton pumps. Nature 463 (7277), 98–102.

Destexhe, A., Mainen, Z. F., Sejnowski, T. J., 1994. Synthesis of models for excitable membranes, synaptic transmission and neuromodulation using a common kinetic formalism. J. Comput. Neurosci. 1 (3), 195–230.

Edden, R. A. E., Muthukumaraswamy, S. D., Freeman, T. C. A., Singh, K. D., 2009. Orientation discrimination performance is predicted by GABA concentration and gamma oscillation frequency in human primary visual cortex. J. Neurosci. 29 (50), 15721–15726.

Engel, A. K., König, P., Kreiter, A. K., Singer, W., 1991. Interhemispheric synchronization of oscillatory neuronal responses in cat visual cortex. Science 252 (5010), 1177–1179.

Fisahn, A., Pike, F. G., Buhl, E. H., Paulsen, O., 1998. Cholinergic induction of network oscillations at 40 Hz in the hippocampus in vitro. Nature 394 (6689), 186–189.

Freeman, W. J., 1968. Relations between unit activity and evoked potentials in prepyriform cortex of cats. J. Neurophysiol. 31 (3), 337–348.

Fries, P., 2009. Neuronal gamma-band synchronization as a fundamental process in cortical computation. Annu. Rev. Neurosci. 32, 209–224.

Fries, P., Reynolds, J. H., Rorie, A. E., Desimone, R., 2001. Modulation of oscillatory neuronal synchronization by selective visual attention. Science 291 (5508), 1560–1563.

Fries, P., Womelsdorf, T., Oostenveld, R., Desimone, R., 2008. The effects of visual stimulation and selective visual attention on rhythmic neuronal synchronization in macaque area V4. J. Neurosci. 28 (18), 4823–4835.

Galán, R. F., Fourcaud-Trocmé, N., Ermentrout, G. B., Urban, N. N., 2006. Correlation-induced synchronization of oscillations in olfactory bulb neurons. J. Neurosci. 26 (14), 3646–3655.

Golomb, D., Amitai, Y., 1997. Propagating neuronal discharges in neocortical slices: computational and experimental study. J. Neurophysiol. 78 (3), 1199–1211.

Gradinaru, V., Zhang, F., Ramakrishnan, C., Mattis, J., Prakash, N., Diester, I., Goshen, I., Thompson, K. R., Deisseroth, K., 2010. Molecular and cellular approaches for diversifying and extending optogenetics. Cell 141 (1), 154–165.

Gray, C. M., Singer, W., 1989. Stimulus-specific neuronal oscillations in orientation columns of cat visual cortex. Proc. Natl. Acad. Sci. U.S.A. 86 (5), 1698–1702.

Gregoriou, G. G., Gotts, S. J., Zhou, H.-H., Desimone, R., 2009. High-frequency, long-range coupling between prefrontal and visual cortex during attention. Science 324 (5931), 1207–1210.

Gruber, T., Müller, M. M., Keil, A., Elbert, T., 1999. Selective visual-spatial attention alters induced gamma band responses in the human EEG. Clin Neurophysiol 110 (12), 2074–2085.

Hasenstaub, A. R., Shu, Y., Haider, B., Kraushaar, U., Duque, A., McCormick, D. A., 2005. Inhibitory postsynaptic potentials carry synchronized frequency information in active cortical networks. Neuron 47 (3), 423–435.

Ishizuka, T., Kakuda, M., Araki, R., Yawo, H., 2006. Kinetic evaluation of photosensitivity in genetically engineered neurons expressing green algae light-gated channels. Neurosci. Res. 54 (2), 85–94.

Jensen, O., Kaiser, J., Lachaux, J.-P., 2007. Human gamma-frequency oscillations associated with attention and memory. Trends Neurosci. 30 (7), 317–324.

König, P., Engel, A. K., Singer, W., 1996. Integrator or coincidence detector? The role of the cortical neuron revisited. Trends Neurosci. 19 (4), 130–137.

Laughlin, S. B., Sejnowski, T. J., 2003. Communication in neuronal networks. Science 301 (5641), 1870–1874.

Ma, Y., Hu, H., Berrebi, A. S., Mathers, P. H., Agmon, A., 2006. Distinct subtypes of somatostatin-containing neocortical interneurons revealed in transgenic mice. J. Neurosci. 26 (19), 5069–5082.

Maldonado, P. E., Friedman-Hill, S., Gray, C. M., 2000. Dynamics of striate cortical activity in the alert macaque: II. Fast time scale synchronization. Cereb. Cortex 10 (11), 1117–1131.

Maloney, K. J., Cape, E. G., Gotman, J., Jones, B. E., 1997. High-frequency gamma electroencephalogram activity in association with sleep-wake states and spontaneous behaviors in the rat. Neuroscience 76 (2), 541–555.

Markram, H., Toledo-Rodriguez, M., Wang, Y., Gupta, A., Silberberg, G., Wu, C., 2004. Interneurons of the neocortical inhibitory system. Nat. Rev. Neurosci. 5 (10), 793–807.

Metherate, R., Cruikshank, S. J., 1999. Thalamocortical inputs trigger a propagating envelope of gamma-band activity in auditory cortex in vitro. Exp. Brain Res. 126 (2), 160–174.

Moore, C. I., Nelson, S. B., Sur, M., 1999. Dynamics of neuronal processing in rat somatosensory cortex. Trends Neurosci. 22 (11), 513–520.

Mutch, J., Knoblich, U., Poggio, T., 2010. CNS: a GPU-based framework for simulating cortically-organized networks. Tech. Rep. MIT-CSAIL-TR-2010-013 / CBCL-286.

Nagel, G., Szellas, T., Huhn, W., Kateriya, S., Adeishvili, N., Berthold, P., Ollig, D., Hegemann, P., Bamberg, E., 2003. Channelrhodopsin-2, a directly light-gated cation-selective membrane channel. Proc. Natl. Acad. Sci. U.S.A. 100 (24), 13940–13945.

Nase, G., Singer, W., Monyer, H., Engel, A. K., 2003. Features of neuronal synchrony in mouse visual cortex. J. Neurophysiol. 90 (2), 1115–1123.

Paik, S.-B., Kumar, T., Glaser, D. A., 2009. Spontaneous local gamma oscillation selectively enhances neural network responsiveness. PLoS Comput. Biol. 5 (3).

Pinto, D. J., Brumberg, J. C., Simons, D. J., 2000. Circuit dynamics and coding strategies in rodent somatosensory cortex. J. Neurophysiol. 83 (3), 1158–1166.

Pouille, F., Scanziani, M., 2001. Enforcement of temporal fidelity in pyramidal cells by somatic feed-forward inhibition. Science 293 (5532), 1159–1163.

Ribary, U., Ioannides, A. A., Singh, K. D., Hasson, R., Bolton, J. P., Lado, F., Mogilner, A., Llinas, R. R., 1991. Magnetic field tomography of coherent thalamocortical 40-Hz oscillations in humans. Proc. Natl. Acad. Sci. U.S.A. 88 (24), 11037–11041.

Roy, A., Steinmetz, P. N., Hsiao, S. S., Johnson, K. O., Niebur, E., 2007. Synchrony: a neural correlate of somatosensory attention. J. Neurophysiol. 98 (3), 1645–1661.

Somers, D. C., Todorov, E. V., Siapas, A. G., Toth, L. J., Kim, D.-S., Sur, M., 1998. A local circuit approach to understanding integration of long-range inputs in primary visual cortex. Cereb. Cortex 8 (3), 204–217.

Steinmetz, P. N., Roy, A., Fitzgerald, P. J., Hsiao, S. S., Johnson, K. O., Niebur, E., 2000. Attention modulates synchronized neuronal firing in primate somatosensory cortex. Nature 404 (6774), 187–190.

Tallon-Baudry, C., Bertrand, O., 1999. Oscillatory gamma activity in humans and its role in object representation. Trends Cogn. Sci. (Regul. Ed.) 3 (4), 151–162.

Tallon-Baudry, C., Bertrand, O., Delpuech, C., Permier, J., 1997. Oscillatory gamma-band (30-70 Hz) activity induced by a visual search task in humans. J. Neurosci. 17 (2), 722–734.

Tiesinga, P. H., Sejnowski, T. J., 2009. Cortical enlightenment: are attentional gamma oscillations driven by ING or PING. Neuron 63 (6), 727–732.

Traub, R. D., Contreras, D., Cunningham, M. O., Murray, H., LeBeau, F. E. N., Roopun, A. K., Bibbig, A., Wilent, W. B., Higley, M. J., Whittington, M. A., 2005. Single-column thalamocortical network model exhibiting gamma oscillations, sleep spindles, and epileptogenic bursts. J. Neurophysiol. 93 (4), 2194–2232.

Wang, H.-P., Spencer, D., Fellous, J.-M., Sejnowski, T. J., 2010. Synchrony of thalamocortical inputs maximizes cortical reliability. Science 328 (5974), 106–109.

Wang, X.-J., Buzsáki, G., 1996. Gamma oscillation by synaptic inhibition in a hippocampal interneuronal network model. J. Neurosci. 16 (20), 6402–6413.

Wehr, M., Zador, A. M., 2003. Balanced inhibition underlies tuning and sharpens spike timing in auditory cortex. Nature 426 (6965), 442–446.

Whittington, M. A., Traub, R. D., Kopell, N. J., Ermentrout, G. B., Buhl, E. H., 2000. Inhibition-based rhythms: experimental and mathematical observations on network dynamics. Int J Psychophysiol 38 (3), 315–336.

Wilent, W. B., Contreras, D., 2005. Dynamics of excitation and inhibition underlying stimulus selectivity in rat somatosensory cortex. Nat. Neurosci. 8 (10), 1364–1370.

Womelsdorf, T., Fries, P., Mitra, P. P., Desimone, R., 2006. Gamma-band synchronization in visual cortex predicts speed of change detection. Nature 439 (7077), 733–736.

Womelsdorf, T., Schoffelen, J.-M., Oostenveld, R., Singer, W., Desimone, R., Engel, A. K., Fries, P., 2007. Modulation of neuronal interactions through neuronal synchronization. Science 316 (5831), 1609–1612.

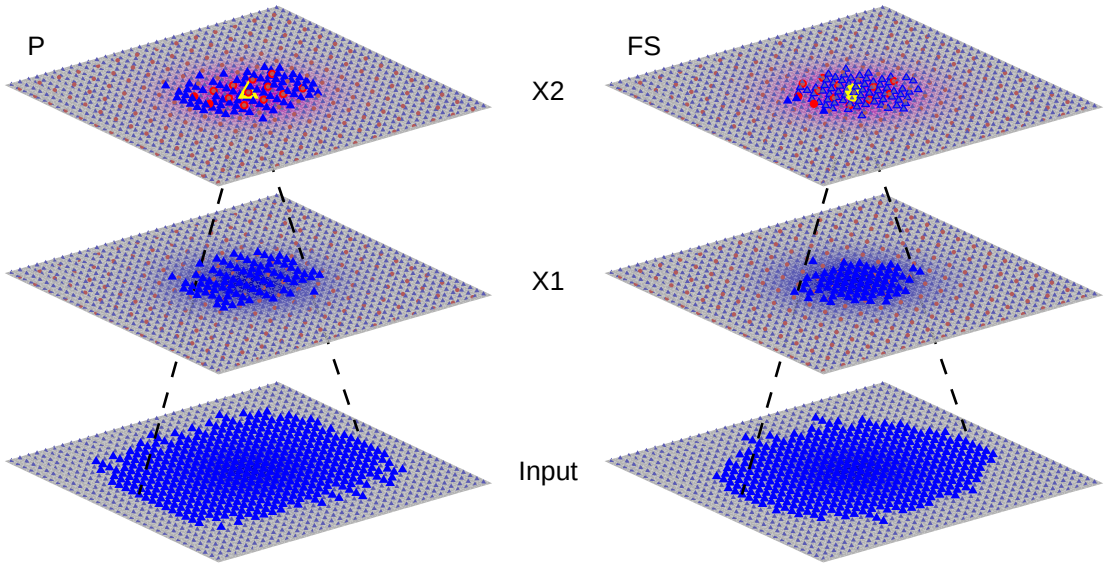

Figure 1. Model architecture and connectivity. Connectivity is shown for one pyramidal (P) cell (left) and one fast-spiking inhibitory (FS) cell (right) in X2 (marked in yellow). Blue triangles represent P cells, red circles represent F cells. Both cells types connect to both cells types locally within each stage and receive input from a pool of excitatory cells from the previous stage.

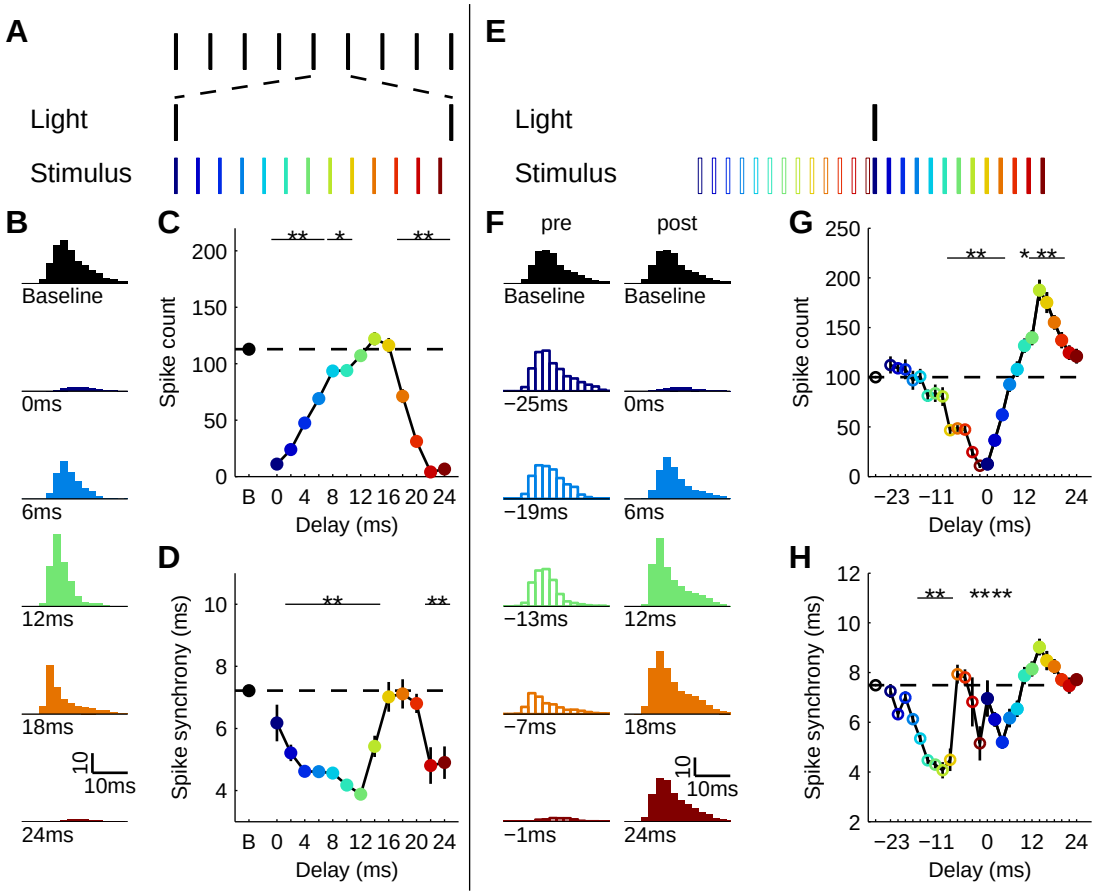

Figure 2. Timing-dependent impact of inhibition on sensory responses. **(A)** Stimulation paradigm for repetitive inhibition. A single sensory stimulus was given at different phases in between two light pulses embedded in a light train at 40 Hz. **(B)** Population X1 response at baseline (top) and different phases during repetitive inhibition. **(C)** Spike count for each phase of stimulation. Dashed line indicates baseline condition. **(D)** Spike synchrony, defined as inter-quartile range of spike times across the population (smaller numbers denote more synchrony). **(E)** Stimulation paradigm for single inhibition. A single sensory stimulus was given at different delays relative to a single light pulse. **(F)** Population X1 response at baseline (top) and different delays for a post-stimulus (left) and pre-stimulus (right) light pulse. **(G)** Spike count for each phase of stimulation. Filled circles correspond to pre-stimulus inhibition, open circles mark post-stimulus inhibition. **(H)** Spike synchrony. *P<0.05, **P<0.01; error bars, mean +/- s.e.m.

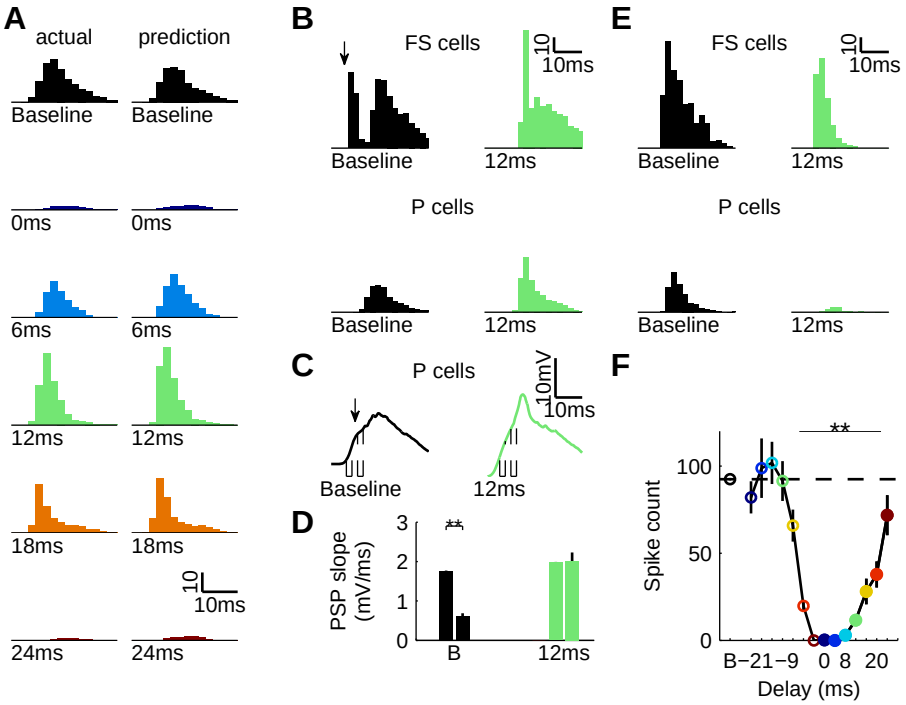

Figure 3. Mechanism of timing-dependent gain modulation. **(A)** Left: actual population X1 responses during repetitive inhibition (re-plotted from 2B). Right: predicted population X1 responses combining independent effects of pre- and post-stimulus inhibition on the spike response packet. **(B)** X1 population responses for FS cells (top) and P cells (bottom) for the baseline (left) and 12 ms delay (right) condition. Arrow in upper left panel indicates the fast FS population spike during baseline missing for the delay condition. **(C)** Average membrane potential of X1 P cells. Dashed lines indicate periods during which slope is measured. Arrow indicates impact of IPSP induced by FS population spike indicated in B. **(D)** PSP slope for both times indicated in C for both conditions. **(E)** Same as (B), but for a model variant without FS-FS inhibition. **(F)** Spike count dependent on delay for model without FS-FS inhibition (analogous to Figure 2C). *P<0.05, **P<0.01; error bars, mean +/- s.e.m.

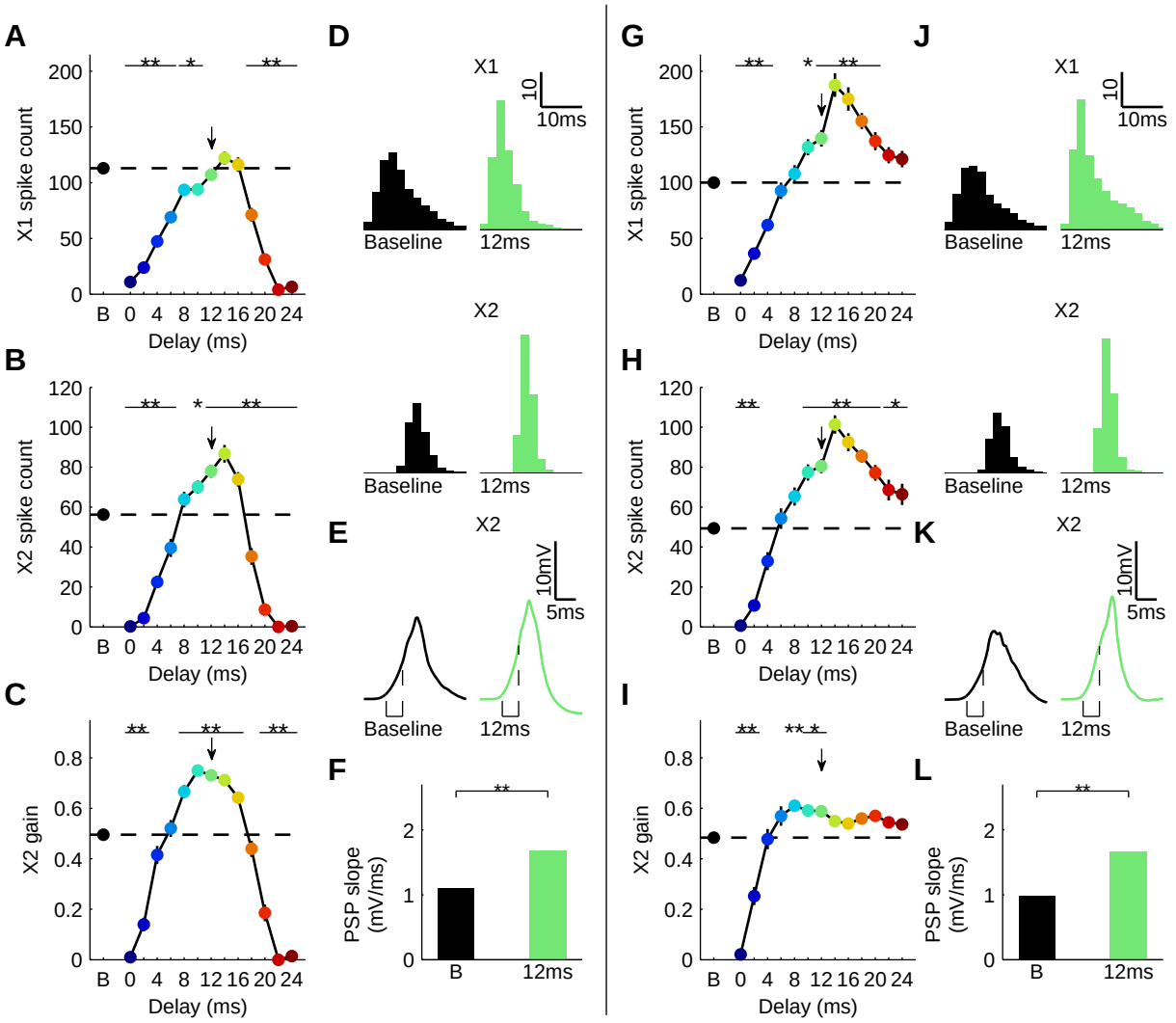

Figure 4. Relationship between X1 spike counts and X2 spike counts and gain. **(A)** X1 spike counts for repetitive inhibition. **(B)** X2 spike counts. **(C)** X2 gain. Arrows in A-C mark the 12ms delay condition. **(D)** X2 population responses for FS cells (top) and P cells (bottom) for the baseline (left) and 12 ms delay (right) condition. **(E)** Average membrane potential of X2 P cells. Dashed lines indicate periods during which slope is measured. **(F)** PSP slope indicated time in E for both conditions. **(G-L)** Same as (A-F), but for single post-stimulus inhibition. *P<0.05, **P<0.01; error bars, mean +/- s.e.m.

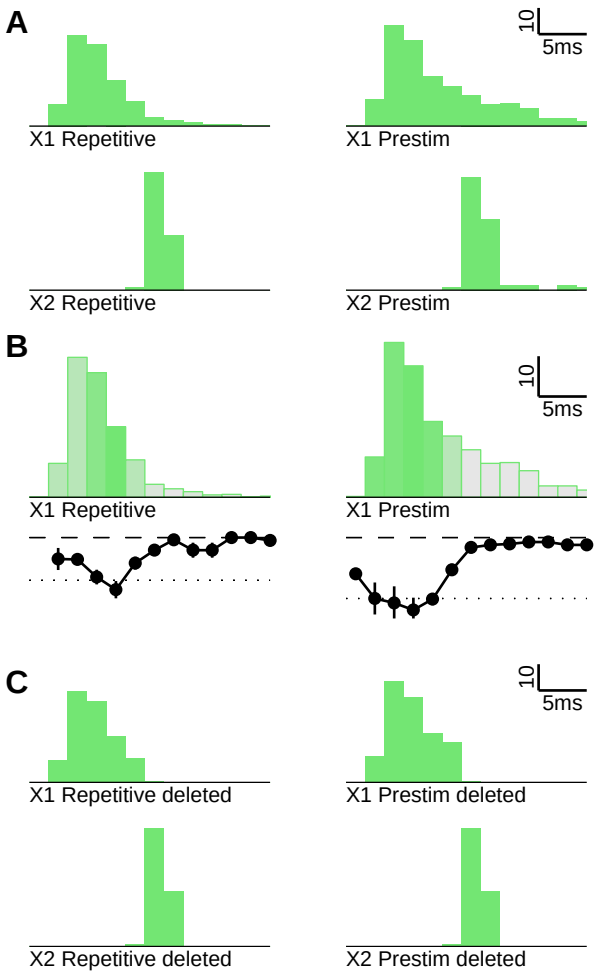

Figure 5: X2 gain depends on X1 packet shape. **(A)** Population responses for X1 (top) and X2 (bottom) for repetitive (left) and single post-stimulus inhibition (right). **(B)** Impact of individual spikes of the X1 response. Shading and the curve below the PSTH indicate the X2 response after deletion of spikes in the corresponding bin. **(C)** Same as A, but after deleting all spikes that did not strongly contribute to the X2 response.

Chapter 4:

Somatostatin-positive interneurons regulate network activity and contribute to sensory adaptation in vivo

4.1 Abstract

Sensory adaptation is a ubiquitous neural phenomenon, occurring at several stages in all sensory modalities (Adrian and Zotterman, 1926; Kohn, 2007; Wark et al., 2007; Demb, 2008). A variety of theories predict such adaptation is crucial to perception, allowing systems to tailor neural computation to the processing demands of a given environment (Abbott et al., 1997; Fairhall et al., 2001; Moore et al., 1999). Previous work examining the cellular mechanisms underlying adaptation has predominantly focused on changes in excitatory activity, with little direct evidence for the involvement of inhibition (Kohn, 2007; Higley and Contreras, 2006; Chung et al., 2002). However, the properties of somatostatin-positive (SOM) interneurons described *in vitro* suggest they are well positioned to show activity-dependent recruitment and generate inhibition following sustained afferent drive. To test the hypothesis that these neurons make a previously unappreciated contribution to this transformation, and more generally to explore their role in regulating network excitability *in vivo*, we employed optogenetic manipulations to selectively activate and inactivate SOM cells with millisecond resolution. Here we show that SOM interneurons regulate spontaneous network activity and transform sensory-driven activity, enhancing signal-to-noise through suppression of background spiking. Further, inactivation of SOM cells partially 'rescues' adapted responses, preferentially increasing sensory-driven activity following sustained sensory stimulation. These findings suggest that a previously unappreciated neocortical mechanism regulates this key sensory transformation.

4.2 Introduction

Sensory environments comprise a wide and variable range of stimulus intensities. Effective encoding of sensory inputs is believed to require dynamic adaptation of neural sensitivity to such changes in environmental context (Fairhall et al., 2001; Wark et al., 2007). The best studied form of such activity-dependent dynamics is sensory adaptation. The suppression of evoked responses during sustained stimulation is a fundamental neural property observed across sensory modalities and at all levels of sensory processing, from periphery to neocortex (Adrian and Zotterman, 1926; Demb, 2008; Kohn, 2007; Wark et al., 2007). Several theoretical studies have highlighted the potential computational benefits of adaptation at the cellular and network levels. One potential role for these dynamics is in maintaining neural activity in an optimal regime for

sensory coding given the level of ongoing drive (Abbott et al., 1997; Fairhall et al., 2001), a feature often called normalization.

Implementation of activity-dependent suppression requires a mechanism that tracks the level of local circuit activity. It has been proposed that specific interneuron types might serve to maintain the balance between excitation and inhibition across a variety of activity levels in the network (Markram et al., 2004; Moore et al., 2010; Haider and McCormick, 2009). This hypothesis is supported by the close link between deficiencies in specific interneurons and epileptic seizures (Cobos et al., 2005; Zhou and Roper, 2010). A leading candidate interneuron type for activity-dependent recruitment during active sensing/high-drive conditions are somatostatin-positive interneurons (SOM). These cells are most prevalent in layers 2/3 and 5, exhibit low-threshold spiking characteristics, and often show broader dendritic processes and axonal distributions (Martinotti type) than basket cells (Beierlein et al., 2000; Beierlein et al., 2003; Halabisky et al., 2006; Kapfer et al., 2007). The suppression generated by these interneurons is usually (though not always) reported as having a longer duration (on the order of ~100 milliseconds) than that generated by basket interneurons (on the order of ~10 milliseconds), and is typically later in onset (Beierlein et al., 2003; Berger et al., 2010; pei Ma et al., 2010).

Several features of SOM suggest that they are positioned to engage during levels of high network drive. *In vitro*, SOM receive facilitating EPSPs during high frequency activity in single presynaptic pyramidal cells, and show supra-linear summation to simultaneous activation of multiple presynaptic pyramidal cells (Kapfer et al., 2007; Silberberg and Markram, 2007; Berger et al., 2010). The breadth of integration implied by their dendritic structure also suggests they track general levels of network activity. This activity-dependence, anatomy, and the basic physiological impact of SOM on neighboring pyramidal cells is observed across different areas, including such distinct regions as somatosensory and olfactory neocortex (Berger et al., 2009).

Despite the *in vitro* data suggesting that SOM should be recruited during processes like repeated sensory drive, no direct evidence for their role in any aspect of sensory coding has been presented. Recent studies have shown SOM can be recruited in mouse V1 by sustained sensory input (Kerlin et al., 2010; pei Ma et al., 2010). Supporting the idea that their recruitment might be activity dependent, V1 SOM neurons show slower sensory activation (pei Ma et al., 2010) and a non-fast spiking class of interneuron (potentially including SOM) is more active during whisking in barrel cortex (Gentet et al., 2010). The only prior study that has implicated SOM in

in vivo sensory regulation has claimed that they regulate input to apical dendrites of layer V neurons, an argument derived from inferences based on the unique Martinotti morphology (Murayama et al., 2009). In sum, in contrast to the more extensive studies of FS/PV, there is little known about the role of SOM in *in vivo* networks, or in controlling sensory responses.

Further, proposals for the mechanisms underlying sensory adaptation in neocortex have focused on cell-intrinsic mechanisms and changes in excitatory synaptic transmission such as synaptic depression (Kohn, 2007). Studies in barrel cortex have emphasized synaptic depression (of excitatory synapses) as an exclusive means for reducing excitation (Chung et al., 2002; Higley and Contreras, 2006). The strength of intracortical, interneuron-driven inhibition has also been argued to decrease with sensory adaptation through synaptic depression (of inhibitory synapses), ostensibly decreasing the impact of inhibition during adaptation and therefore arguing against the prediction that interneurons mediate this form of inhibition (Higley and Contreras, 2006).

To test the hypothesis that SOM interneurons impact *in vivo* neocortical dynamics, and more specifically that their activity contributes to neocortical sensory adaptation, we employed optogenetic manipulations to selectively activate and inactivate them on millisecond timescales. This approach provided causal control specific to cell-type and with high temporal specificity. If SOM interneurons impact spontaneous *in vivo* neocortical dynamics as predicted by *in vitro* studies, direct optical SOM stimulation should drive longer IPSPs in neighboring pyramidal neurons, with a longer onset latency and a smaller magnitude than IPSPs generated by similar stimulation of FS/PV interneurons (Cardin et al., 2009).

The key signature of sensory adaptation in barrel cortex is a reduction of evoked spiking. A key computational 'benefit' proposed for this reduction is improved signal-to-noise in evoked spiking due to differential suppression of noisy or more poorly timed spikes within the response period (see (Moore, 2004) for a discussion). If SOM interneurons impact sensory adaptation, as predicted by our hypothesis, then stimulation of SOM should reduce subthreshold evoked membrane potential (Chung et al., 2002; Higley and Contreras, 2006), should reduce spike rate, and should enhance driven spiking relative to background rates in non-adapted barrel cortex. Conversely, adaptation-driven changes should be 'rescued' by optical suppression of SOM, increasing the membrane potential and spike rate, and decreasing signal-to-noise. Further, the *in vitro* dependence of SOM recruitment on high levels of network activity (in rate and/or

synchrony) predicts that these neurons will only shape adapted responses, and that SOM inactivation should have little impact on sensory-evoked activity in a non-adapted neocortex.

4.3 Results

4.3.1 Cell-type-specific expression of light-activated ion channels and pumps

To achieve bidirectional control of SOM interneurons we used a combination of channelrhodopsin-2 (ChR2), a sodium channel originally identified in the alga Chlamydomonas reinhardtii (Boyden et al., 2005; Deisseroth et al., 2006) and halorhodopsin (eNpHR3.0), a modified version of the chloride pump from the archaeon *Natronomonas pharaonis* (Gradinaru et al., 2010). We injected a mixture of adeno-associated viral vectors containing either double-floxed inverted open reading frame ChR2-mCherry (AAV DIO ChR2-mCherry) or double-floxed inverted open reading frame eNpHR3.0-EYFP (AAV DIO eNpHR3.0-EYFP), providing Cre-dependent expression of both opsins, into the somatosensory cortex barrel field of SOM-Cre mice (Fig. 1a). Expression of both opsins was specific to SOM^+ cells (Fig. 1b-e) and not co-localized with parvalbumin, a marker for the majority of SOM^- interneurons (Gonchar et al., 2007; Xu et al., 2010) (Fig. 1f-i). Our findings are consistent with the characterization of this Cre-line by its originators (Huang et al., personal communication).

4.3.2 SOM cell activation suppresses spontaneous activity

We found that 1 ms blue (473 nm) light pulses were sufficient to drive spiking activity in SOM interneurons, however 10 ms pulses elicited more robust and shorter latency spiking (8.8 ± 2.0 ms, mean ± s.d., n = 98) (Fig. 2a). Conversely, orange (593 nm) light pulses sustained for 2 s reliably suppressed spontaneous activity during the entire stimulation period and induced strong transient rebound spiking at the offset, consistent with the observation of sag currents in these low-threshold spiking cells *in vitro* (Beierlein et al., 2003; Ma et al., 2006) (Fig. 2b).

Optical drive of SOM generated inhibitory post-synaptic potentials (IPSPs) in nearby layer 5 pyramidal cells and suppressed spontaneous spiking activity on a parallel time course (Fig. 2c). Onset latency of IPSPs was 6.6 ± 2.9 ms (mean ± s.d., n = 22), consistent with direct synaptic input from SOM cells. Measured IPSPs lasted 204 ± 71 ms, with a time to peak of 46 ± 14 ms. The duration, magnitude and latency of this inhibition was nearly identical with that observed in

in vitro studies (Berger et al., 2010) and approximately an order of magnitude slower than the kinetics of FS/PV interneuron-induced IPSPs *in vivo* (Cardin et al., 2009).

The average size of IPSPs generated by pre-stimulus membrane potentials between -50 and -65 mV was 3.8 ± 2.6 mV. The mean apparent reversal potential based on spontaneous membrane potential fluctuations was -67 ± 14x mV, indicating involvement of Cl^- conductances, although a subset of cells showed a lower apparent reversal potentials in response to current injections of approximately -90 mV (Fig. 2e). This variance could reflect either variation within the SOM population or their targets as have been previously reported (Halabisky et al., 2006; Xu and Callaway, 2009), or could reflect variation in the quality of space clamp in our recordings, a common concern with intracellular *in vivo* approaches.

Sustained (2 s) orange light stimulation led to no appreciable depolarization in pyramidal cells (0.3 ± 0.2 mV, $p = 0.84$) accompanied by no increase in spontaneous firing rate ($p = 0.84$) (Fig. 2d). After light offset, pyramidal cells exhibited an IPSP and reduction in spiking in accordance with the rebound spiking found in SOM, which had a slower onset but total duration and size similar to the ChR2-evoked IPSP (Fig. 2f).

4.3.3 Modulation of SOM cell activity differentially impacts early and late sensory responses

To test the impact of SOM activation on sensory evoked responses and their role in adaptation, we combined short (10 ms) blue or sustained (2.5 s) orange light pulses with a train of 16 vibrissa stimuli presented at 8 Hz. Light pulses were timed to coincide with the response to the first (early) or fifth (late) stimulus given the time course of their impact on spontaneous activity and the vibrissa response in pyramidal cells. Based on the time to peak of blue light induced IPSPs and spontaneous spiking suppression, blue light was onset 25 ms before vibrissa stimulus onset. In contrast, orange light was onset 200 ms before vibrissa stimulation because of the long duration of the observed suppressive effect.

Activation of SOM impacted early and late sensory responses in similar ways (Fig. 3a,c,e,g). As with activation during spontaneous activity, blue light pulses evoked an IPSP of comparable size (early: -2.2 ± 0.3 mV; late: -2.1 ± 0.4 mV; $n = 19$). Peak membrane potential responses were also significantly reduced (early: -0.9 ± 0.5 mV, $p = 0.01$; late: -0.8 ± 0.3 mV, $p = 0.03$), although less than would be predicted from the size of the IPSP. The PSP 'size'—measured relative to the

immediately preceding membrane potential—was increased (early: 1.3 ± 0.4 mV, p = 0.004; late: 1.3 ± 0.4 mV, p = 0.006) as was the rate of rise (early: 0.7 ± 0.2 mV/ms, p = 0.003; late: 0.4 ± 0.1 mV, p = 0.04). Firing rates were significantly reduced during early and late conditions (early: -0.8 ± 0.3 Hz, p =0.004; late: -0.8 ± 0.4 Hz, p = 0.03). Vector strength, measured as the ratio between evoked and background spikes, was increased for both conditions, although neither change was significant, likely due to the high variance in the population (early: 0.03 ± 0.06, p = 0.78; late: 0.04 ± 0.08, p = 0.49).

Inactivation of SOM reversed key effects of adaptation, but showed minimal impact on sensory responses in the non-adapted state (Fig. 3b,d,f,h). While early inactivation caused no change in evoked membrane potential (0.0 ± 0.1 mV, p = 0.75), late inactivation led to a significant increase (0.6 ± 0.3 mV, p = 0.049). Correlated changes were observed in spike frequency, which was unchanged early (0.0 ± 0.2 Hz, p = 0.94), but significantly increased late (0.7 ± 0.3 Hz, p = 0.01). Vector strength decreased only slightly early and more strongly late, although neither change was significant (early: -0.02 ± 0.04, p = 0.57; late: -0.09 ± 0.06, p = 0.27), although it should be noted that these changes are numerically opposite to the activation condition. No significant effects were observed for relative PSP sizes (early: -0.4 ± 0.3 mV, p = 0.12; late: -0.3 ± 0.2 mV, p = 0.47) and PSP slope (early: -0.05 ± 0.04 mV/ms, p = 0.47; late: -0.01 ± 0.01 mV/ms, p = 0.49).

These findings directly support our initial hypothesis, that SOM play a previously unappreciated role in sensory adaptation: SOM activation replicates the suppressive effects of adaptation, and SOM inactivation 'rescues' adapted responses, with little impact on non-adapted responses. However, the magnitude of effects during inactivation, while significant, were relatively small and variable. We reasoned that the variance we observed was due to variability in ambient network excitation in anesthetized animals. Activation of SOM *in vitro* depends on higher-frequency and more synchronous drive, and they are depolarized by factors such acetylcholine (Fanselow et al., 2008). As such, the relative anesthetic level for any given experiment could modulate their recruitment by a variety of mechanisms.

To investigate the relationship between anesthetic state and efficacy of our optical inactivation, we computed the relative power in the delta band (0 - 4 Hz) in the surface local field potential for recordings from two animals (Figure 4a,b). We found that peak membrane potential changes for late inactivation were significantly higher during recordings with lower delta power (1.4 ± 0.3

mV vs. 0.3 ± 0.2 mV, p = 0.03). Firing rate changes were also elevated, although not significantly, likely due to small sample size (1.7 ± 1.1 Hz vs. -0.3 ± 0.2 mV, p = 0.18). Restricting our analysis to the subset of recordings with low delta (< 30% of total power) resulted in increased effects of SOM inactivation (Figure 4e). Peak depolarization during early inactivation showed no change in this sub-sample (-0.1 ± 0.3 mV, p = 0.56), while late inactivation revealed an increased peak membrane potential (1.4 ± 0.6 mV, p = 0.09). PSP sizes were decreased (early: -1.1 ± 0.6 mV, p = 0.16; late: -0.5 ± 0.2 mV, p = 0.47) and PSP slope was reduced early but not late (early: -0.1 ± 0.1 mV/ms, p = 0.31; late: 0.02 ± 0.02 mV/ms, p = 0.44). Spike frequency was unchanged early (-0.2 ± 0.4 Hz, p = 1), but increased late (1.2 ± 0.7 Hz, p = 0.19). Vector strength was not significantly changed in this sub-sample (early: -0.05 ± 0.09, p = 0.63; late: 0.01 ± 0.11, p = 1.0).

To further quantify the effect of SOM cell inactivation on the adaptation of evoked spiking in this sub-sample of low delta power recordings, we calculated adaptation ratios for the baseline and late inactivation conditions (Figure 4c,d). Peak membrane potential was reduced by 17 ± 31% during baseline but only 2 ± 22 % for late inactivation. Evoked firing was reduced by 52 ± 10% but 7 ± 18%, corresponding to a 'rescue' from 88% of the effect of adaptation.

4.4 Discussion

We employed bidirectional optical modulation of SOM cells to test their impact on neocortical dynamics. SOM activation mimicked the main effects of sensory adaptation (Garabedian et al., 2003), decreasing spike rate and membrane potential while increasing vector strength. In contrast, SOM inactivation did not appreciably impact responses to the first stimulus but significantly increased late firing, 'rescuing' adapted responses. This dissociation between early and late inactivation is consistent with a delayed, activity-dependent recruitment of SOM cells, such that their activation only affects stimuli presented in this network state.

Drive-dependent recruitment of SOM interneurons positions them to provide inhibitory balance during active sensory processing, such as during whisking, attentive viewing or sniffing. As such, SOM may sense ongoing network activity levels and enhance signal-to-noise in spiking activity accordingly (Moore et al., 2010), increasing the ratio of driven spikes to background or less-precisely timed signals. Increased precision in spiking, obtained through suppression of weaker inputs, may facilitate sensory discrimination. This hypothesis presumes that signal to

noise quantified in this way is relevant to information processing in the neocortex. As discussed in detail in Chapter 3, the relative temporal dispersion of a spike packet is potentially key to the relay of signals in the neocortex, but there are conditions under which such temporal precision does not necessarily impact downstream firing probability (and thereby transmission of a rate code).

The higher impact of inactivation during periods of lighter anesthesia is consistent with reports of state-dependent non-fast spiking cell activity *in vivo* (Gentet et al., 2010), showing an increase in activity during whisking as compared to quiescence. SOM cells have been reported to depolarize in response to acetylcholine application *in vitro* (Beierlein et al., 2000; Kawaguchi and Kondo, 2003), and isoflurane suppresses acetylcholine release in cerebral cortex in a dose-dependent manner (Shichino et al., 1998). As such, higher isoflurane concentrations appear to have lead to partial inactivation of SOM cells, occluding the full effect of optogenetic inactivation in our study. Anesthesia is an important and consistent confound in the study of adaptation, and synaptic dynamics in general. Synaptic function and dynamics are strongly modulated by acetylcholine (Gil et al., 1997), and cortical acetylcholine release is modulated by the general arousal and attentional state of the animal (Arnold et al., 2002) and suppressed during anesthesia (Shichino et al., 1998; Shichino et al., 1998; Dong et al., 2006). These conditions could partly explain the prior emphasis on synaptic depression as the sole or nearly exclusive mechanism regulating sensory adaptation.

The increase in PSP size and slope, in combination with an overall decrease in membrane potential, during SOM cell activation suggests a dual action of direct inhibition of pyramidal cells combined with "disinhibition", i.e. inhibition of fast-spiking (FS) cells which inhibit pyramidal cells. Inhibition of parvalbumin-positive FS cells has been reported *in vitro* (Beierlein et al., 2000) and the increase in SOM cell activity *in vivo* during whisking was accompanied by a decrease in FS cell spiking (Gentet et al., 2010). These combined effects led to a suppression of background activity relative to evoked spiking, resulting in an increased signal-to-noise ratio, consistent with previous data (Garabedian et al., 2003).

There have been numerous reports extolling the delicate balance of excitation and inhibition in cortical networks across a wide range of conditions, including during sensory adaptation (Higley and Contreras, 2006; Heiss et al., 2008; Haider and McCormick, 2009). Maintaining such an intricate balance might be difficult to achieve with independent mechanisms of adaptation for

excitatory and inhibitory cells and/or synapses such as synaptic depression that is local to each synapse and only depends on the activity of the synapse itself, as previously proposed. In contrast, a common mechanism sensing the overall activity in a network and suppressing excitatory and inhibitory cells accordingly can explain the tight balance maintained more easily. With their activity-dependent recruitment (Kapfer et al., 2007; Silberberg and Markram, 2007; Berger et al., 2009; Berger et al., 2010) and effects on both pyramidal and FS cells (Beierlein et al., 2000; Gentet et al., 2010), SOM cells seem to be positioned perfectly to play such a role, and our data directly support this hypothesis.

Previous studies in visual and somatosensory neocortex have downplayed the role of inhibitory neurons in adaptation, based in part on the results of application of the $GABA_A$ receptor antagonist bicuculline (DeBruyn and Bonds, 1986; Vidyasagar, 1990; Nelson, 1991; Chung et al., 2002). During bicuculline administration, the magnitude of adaptation is unchanged. Recently, it has been reported that dendrite-targeting interneurons such as SOM act via $GABA_A$ receptors containing different subunits than soma-targeting inhibitory cells (Ali and Thomson, 2008), consistent with the prolonged time course we observed *in vivo* and others observed *in vitro* (Beierlein et al., 2000; Berger et al., 2010). To our knowledge, it has not been shown whether these receptors are bicuculline sensitive. SOM may also be acting through $GABA_B$ receptors. Bicuculline-insensitive $GABA_B$ receptors mediate inhibition in apical tufts of layer 5 pyramidal neurons (Pérez-Garci et al., 2006), and blocking $GABA_B$ receptors has a larger effect on the sustained response to visual stimuli as compared to their onset transient (Allison et al., 1996), consistent with our findings. Other previous studies have concluded that the site of action of adaptation must be presynaptic, based on pharmacological manipulations (Nelson, 1991; McLean and Palmer, 1996). Presynaptic $GABA_B$ receptors regulate synaptic efficacy and dynamics (Dittman and Regehr, 1996; Deisz et al., 1997; Brenowitz et al., 1998), and amacrine cells in the retina mediate adaptation by inhibiting ganglion cells directly as well as at the presynaptic terminals of their inputs (Zaghloul et al., 2007; Demb, 2008). Such a combination of pre- and postsynaptic mechanisms is consistent with our data and could reconcile the involvement of GABAergic interneurons with previous reports of hyperpolarization as a key mechanism of adaptation (Carandini and Ferster, 1997) as well as the lack of sensitivity to bicuculline application.

4.5 Methods

4.5.1 Virus injections

Transgenic mice expressing Cre-recombinase in SOM neurons were anesthetized with 1-2% isoflurane. A small craniotomy was made 1.2 mm posterior to bregma and 3.0 mm lateral to the midline. A 1:1 mixture of adeno-associated virus vectors containing AAV-DIO-ChR2-mCherry and AAV-DIO-eNpHR3.0-EYFP, respectively, was delivered by a glass pipette. The glass micropipette was lowered to 600 μm below the cortical surface. A bolus of 0.5 μl of virus was injected into barrel cortex at 0.05 μl/min. The pipette was held in place for 10 min following the injection and then retracted to a depth of 300 μm below the surface. An additional 0.5 μl virus was injected at the same rate, the pipette was held in place for 10 min after the injection before being retracted from the brain. The scalp incision was closed with Vetbond, and analgesics were given to aid recovery (0.1 mg/kg Buprenex).

4.5.2 Animal Anesthesia and Surgery

SOM-Cre mice were anesthetized with isoflurane mixed with oxygen for all procedures. During surgery, anesthesia was kept at a level of 1-2%. The state of the animals was monitored by measuring temperature, breathing rate and surface local field potentials. Prior to surgical procedures, the animal's reflexes were tested to determine that a surgical anesthesia has been reached. Immediately prior to electrophysiological recording the anesthetic level was reduced to 0.5-1.5% isoflurane, the animal was transferred to the recording setup and held in place with a head post cemented to the skull. A small craniotomy was performed over barrel cortex (Bregma AP -1.2, ML 3.0). Whole-brain surface local field potentials were recorded by two epidural tungsten wires placed approximately 1mm anterior of Bregma and posterior of Lambda.

4.5.3 Electrophysiological recordings and stimulation

All stimulus control and data acquisition were performed using software custom-written in LabView and Matlab. All recordings were performed at cortical depths between 700 and 1000 μm, corresponding to layer 5.

Light stimuli were created using two diode pumped solid state lasers operating at 473 and 593 nm, combined into a single beam and coupled into an optical fiber. The end of the fiber was placed over the craniotomy, approximately 200 µm above the pia.

Vibrissae contralateral to the recording site were stimulated using trains of 25 ms long air puffs aimed to deflect the majority of mystacial vibrissae in a caudal direction and presented at a rate of 8 Hz for 2 s.

4.5.3.1 Juxtacellular recordings

Glass electrodes (10-14 MΩ resistance) were pulled and filled with saline. Electrodes were lowered under positive pressure while injecting small amplitude current pulses. Upon encounter of a cell membrane indicated by a sudden increase in resistance, pressure was relieved and light suction was applied. After formation of a medium resistance seal (>= 80 MΩ) and verification of occurrence of spikes, the cell-attached recording configuration was achieved.

4.5.3.2 Intracellular recordings

Glass electrodes (5-7 MΩ resistance) were pulled and filled with internal patch solution (in mM) 130 K+-gluconate, 4 KCl, 2 NaCl, 10 HEPES, 0.2 EGTA, 10 Phosphocreatine, 4 Mg-ATP, 0.3 NA3-GTP, adjusted to pH 7.25 with KOH and 292 mOsm with ddH2O. During a subset of recordings, the patch solution also contained 0.2% biocytin. Electrodes were lowered under positive pressure while injecting small amplitude current pulses. Upon encounter of a cell membrane indicated by a sudden increase in resistance, pressure was relieved and light suction was applied. After formation of a gigaseal (typically 2-3 GΩ), the cell membrane was broken and the whole-cell recording configuration achieved. Access resistance was compensated online and corrected post-hoc if necessary.

4.5.4 Data analysis

All data analysis was performed using custom-written routines in Matlab. Spike activity was binned at 25-125 ms and reported as instantaneous firing rate. For membrane potential analysis during combined light and vibrissa stimulation, the average baseline potential 500-1000 ms before stimulus onset was subtracted from each condition. For quantification of the effects of light stimulation on sensory responses all values were reported as change relative to baseline (no light stimulation).

4.5.5 Immunohistochemistry

Animals were transcardially perfused with 100 mM phosphate buffer (PB) followed by 4% paraformaldehyde in PB and brains were extracted and post-fixed in 4% paraformaldehyde. Subsequently, brains were transferred to a solution of 2% paraformaldehyde and 30% sucrose for cryoprotection for another 24 hours. Slices of 25-60 μm thickness were cut using a cryostat and either immediately mounted on slides using Vectashield or processed for immunohistological staining of SOM or PV. Free-floating sections were rinsed in PBS five times and incubated in blocking solution (10% normal goat serum in PBS with 0.2% Triton-X 100) for 1 h and then with primary antibody diluted in blocking solution for 12-36 h at room temperature. Primary antibodies used were somatostatin AB5494 (Millipore; 1:100) and parvalbumin PV-28 (Swant, 1:2,000). After rinsing with PBS five times, sections were incubated with the appropriate secondary antibodies diluted in blocking solution for 2 h at room temperature. Secondary antibodies used were AlexaFluor 450 (Invitrogen, 1:200) and AlexaFluor 647 (Invitrogen, 1:200). Somatostatin staining was amplified using a TSA amplification kit (Invitrogen). Image stacks were taken using a confocal microscope.

4.6 References

Abbott, L. F., Varela, J. A., Sen, K., Nelson, S. B., 1997. Synaptic depression and cortical gain control. Science 275 (5297), 220–224.

Adrian, E. D., Zotterman, Y., 1926. The impulses produced by sensory nerve-endings: Part II. The response of a Single End-Organ. J. Physiol. (Lond.) 61 (2), 151–171.

Ali, A. B., Thomson, A. M., 2008. Synaptic alpha 5 subunit-containing GABAA receptors mediate IPSPs elicited by dendrite-preferring cells in rat neocortex. Cereb. Cortex 18 (6), 1260–1271.

Allison, J. D., Kabara, J. F., Snider, R. K., Casagrande, V. A., Bonds, A. B., 1996. GABAB-receptor-mediated inhibition reduces the orientation selectivity of the sustained response of striate cortical neurons in cats. Vis. Neurosci. 13 (3), 559–566.

Arnold, H. M., Burk, J. A., Hodgson, E. M., Sarter, M., Bruno, J. P., 2002. Differential cortical acetylcholine release in rats performing a sustained attention task versus behavioral control tasks that do not explicitly tax attention. Neuroscience 114 (2), 451–460.

Beierlein, M., Gibson, J. R., Connors, B. W., 2000. A network of electrically coupled interneurons drives synchronized inhibition in neocortex. Nat. Neurosci. 3 (9), 904–910.

Beierlein, M., Gibson, J. R., Connors, B. W., 2003. Two dynamically distinct inhibitory networks in layer 4 of the neocortex. J. Neurophysiol. 90 (5), 2987–3000.

Berger, T. K., Perin, R., Silberberg, G., Markram, H., 2009. Frequency-dependent disynaptic inhibition in the pyramidal network: a ubiquitous pathway in the developing rat neocortex. J. Physiol. (Lond.) 587 (22), 5411–5425.

Berger, T. K., Silberberg, G., Perin, R., Markram, H., 2010. Brief bursts self-inhibit and correlate the pyramidal network. PLoS Biol. 8 (9).

Boyden, E. S., Zhang, F., Bamberg, E., Nagel, G., Deisseroth, K., 2005. Millisecond-timescale, genetically targeted optical control of neural activity. Nat. Neurosci. 8 (9), 1263–1268.

Brenowitz, S., David, J., Trussell, L. O., 1998. Enhancement of synaptic efficacy by presynaptic GABA(B) receptors. Neuron 20 (1), 135–141.

Carandini, M., Ferster, D., 1997. A tonic hyperpolarization underlying contrast adaptation in cat visual cortex. Science 276 (5314), 949–952.

Cardin, J. A., Carlén, M., Meletis, K., Knoblich, U., Zhang, F., Deisseroth, K., Tsai, L.-H., Moore, C. I., 2009. Driving fast-spiking cells induces gamma rhythm and controls sensory responses. Nature 459 (7247), 663–667.

Chung, S., Li, X., Nelson, S. B., 2002. Short-term depression at thalamocortical synapses contributes to rapid adaptation of cortical sensory responses in vivo. Neuron 34 (3), 437–446.

Cobos, I., Calcagnotto, M. E., Vilaythong, A. J., Thwin, M. T., Noebels, J. L., Baraban, S. C., Rubenstein, J. L. R., 2005. Mice lacking Dlx1 show subtype-specific loss of interneurons, reduced inhibition and epilepsy. Nat. Neurosci. 8 (8), 1059–1068.

DeBruyn, E. J., Bonds, A. B., 1986. Contrast adaptation in cat visual cortex is not mediated by GABA. Brain Res. 383 (1), 339–342.

Deisseroth, K., Deisseroth, K., Feng, G., Feng, G., Majewska, A. K., Majewska, A. K., Miesenböck, G., Ting, A., Schnitzer, M. J., 2006. Next-generation optical technologies for illuminating genetically targeted brain circuits. J. Neurosci. 26 (41), 10380–10386.

Deisz, R. A., Billard, J. M., Zieglgänsberger, W., 1997. Presynaptic and postsynaptic GABAB receptors of neocortical neurons of the rat in vitro: differences in pharmacology and ionic mechanisms. Synapse 25 (1), 62–72.

Demb, J. B., 2008. Functional circuitry of visual adaptation in the retina. J. Physiol. (Lond.) 586 (18), 4377–4384.

Dittman, J. S., Regehr, W. G., 1996. Contributions of calcium-dependent and calcium-independent mechanisms to presynaptic inhibition at a cerebellar synapse. J. Neurosci. 16 (5), 1623–1633.

Dong, H.-L., Fukuda, S., Murata, E., Higuchi, T., 2006. Excitatory and inhibitory actions of isoflurane on the cholinergic ascending arousal system of the rat. Anesthesiology 104 (1), 122–133.

Fairhall, A. L., Lewen, G. D., Bialek, W., de Ruyter Van Steveninck, R. R., 2001. Efficiency and ambiguity in an adaptive neural code. Nature 412 (6849), 787–792.

Fanselow, E. E., Richardson, K. A., Connors, B. W., 2008. Selective, state-dependent activation of somatostatin-expressing inhibitory interneurons in mouse neocortex. J. Neurophysiol. 100 (5), 2640–2652.

Garabedian, C. E., Jones, S. R., Merzenich, M. M., Dale, A. M., Moore, C. I., 2003. Band-pass response properties of rat SI neurons. J. Neurophysiol. 90 (3), 1379–1391.

Gentet, L. J., Avermann, M., Matyas, F., Staiger, J. F., Petersen, C. C. H., 2010. Membrane Potential Dynamics of GABAergic Neurons in the Barrel Cortex of Behaving Mice. Neuron 65 (3), 422–435.

Gil, Z., Connors, B. W., Amitai, Y., 1997. Differential regulation of neocortical synapses by neuromodulators and activity. Neuron 19 (3), 679–686.

Gonchar, Y., Wang, Q., Burkhalter, A., 2007. Multiple distinct subtypes of GABAergic neurons in mouse visual cortex identified by triple immunostaining. Front. Neuroanat. 1.

Gradinaru, V., Zhang, F., Ramakrishnan, C., Mattis, J., Prakash, N., Diester, I., Goshen, I., Thompson, K. R., Deisseroth, K., 2010. Molecular and cellular approaches for diversifying and extending optogenetics. Cell 141 (1), 154–165.

Haider, B., McCormick, D. A., 2009. Rapid neocortical dynamics: cellular and network mechanisms. Neuron 62 (2), 171–189.

Halabisky, B., Shen, F., Huguenard, J. R., Prince, D. A., 2006. Electrophysiological classification of somatostatin-positive interneurons in mouse sensorimotor cortex. J. Neurophysiol. 96 (2), 834–845.

Heiss, J. E., Katz, Y., Ganmor, E., Lampl, I., 2008. Shift in the balance between excitation and inhibition during sensory adaptation of S1 neurons. J. Neurosci. 28 (49), 13320–13330.

Higley, M. J., Contreras, D., 2006. Balanced excitation and inhibition determine spike timing during frequency adaptation. J. Neurosci. 26 (2), 448–457.

Kapfer, C., Glickfeld, L. L., Atallah, B. V., Scanziani, M., 2007. Supralinear increase of recurrent inhibition during sparse activity in the somatosensory cortex. Nat. Neurosci. 10 (6), 743–753.

Kawaguchi, Y., Kondo, S., 2003. Parvalbumin, somatostatin and cholecystokinin as chemical markers for specific GABAergic interneuron types in the rat frontal cortex. J. Neurocytol. 31 (3), 277–287.

Kerlin, A. M., Andermann, M. L., Berezovskii, V. K., Reid, R. C., 2010. Broadly tuned response properties of diverse inhibitory neuron subtypes in mouse visual cortex. Neuron 67 (5), 858–871.

Kohn, A., 2007. Visual adaptation: physiology, mechanisms, and functional benefits. J. Neurophysiol. 97 (5), 3155–3164.

Ma, Y., Hu, H., Berrebi, A. S., Mathers, P. H., Agmon, A., 2006. Distinct subtypes of somatostatin-containing neocortical interneurons revealed in transgenic mice. J. Neurosci. 26 (19), 5069–5082.

Markram, H., Toledo-Rodriguez, M., Wang, Y., Gupta, A., Silberberg, G., Wu, C., 2004. Interneurons of the neocortical inhibitory system. Nat. Rev. Neurosci. 5 (10), 793–807.

McLean, J., Palmer, L. A., 1996. Contrast adaptation and excitatory amino acid receptors in cat striate cortex. Vis. Neurosci. 13 (6), 1069–1087.

Moore, C. I., 2004. Frequency-dependent processing in the vibrissa sensory system. J. Neurophysiol. 91 (6), 2390–2399.

Moore, C. I., Carlén, M., Knoblich, U., Cardin, J. A., 2010. Neocortical interneurons: from diversity, strength. Cell 142 (2), 189–193.

Moore, C. I., Nelson, S. B., Sur, M., 1999. Dynamics of neuronal processing in rat somatosensory cortex. Trends Neurosci. 22 (11), 513–520.

Murayama, M., Pérez-Garci, E., Nevian, T., Bock, T., Senn, W., Larkum, M. E., 2009. Dendritic encoding of sensory stimuli controlled by deep cortical interneurons. Nature 457 (7233), 1137–1141.

Nelson, S. B., 1991. Temporal interactions in the cat visual system. III. Pharmacological studies of cortical suppression suggest a presynaptic mechanism. J. Neurosci. 11 (2), 369–380.

Pérez-Garci, E., Gassmann, M., Bettler, B., Larkum, M. E., 2006. The GABAB1b isoform mediates long-lasting inhibition of dendritic Ca2+ spikes in layer 5 somatosensory pyramidal neurons. Neuron 50 (4), 603–616.

pei Ma, W., hua Liu, B., tang Li, Y., Huang, Z. J., Zhang, L. I., Tao, H. W., 2010. Visual representations by cortical somatostatin inhibitory neurons–selective but with weak and delayed responses. J. Neurosci. 30 (43), 14371–14379.

Shichino, T., Murakawa, M., Adachi, T., Arai, T., Miyazaki, Y., Mori, K., 1998. Effects of inhalation anaesthetics on the release of acetylcholine in the rat cerebral cortex in vivo. Br J Anaesth 80 (3), 365–370.

Silberberg, G., Markram, H., 2007. Disynaptic inhibition between neocortical pyramidal cells mediated by Martinotti cells. Neuron 53 (5), 735–746.

Vidyasagar, T. R., 1990. Pattern adaptation in cat visual cortex is a co-operative phenomenon. Neuroscience 36 (1), 175–179.

Wark, B., Lundstrom, B. N., Fairhall, A. L., 2007. Sensory adaptation. Curr. Opin. Neurobiol. 17 (4), 423–429.

Xu, X., Callaway, E. M., 2009. Laminar specificity of functional input to distinct types of inhibitory cortical neurons. J. Neurosci. 29 (1), 70–85.

Xu, X., Roby, K. D., Callaway, E. M., 2010. Immunochemical characterization of inhibitory mouse cortical neurons: three chemically distinct classes of inhibitory cells. J. Comp. Neurol. 518 (3), 389–404.

Zaghloul, K. A., Manookin, M. B., Borghuis, B. G., Boahen, K., Demb, J. B., 2007. Functional circuitry for peripheral suppression in Mammalian Y-type retinal ganglion cells. J. Neurophysiol. 97 (6), 4327–4340.

Zhou, F.-W., Roper, S. N., 2010. Altered Firing Rates and Patterns in Interneurons in Experimental Cortical Dysplasia. Cereb. Cortex.

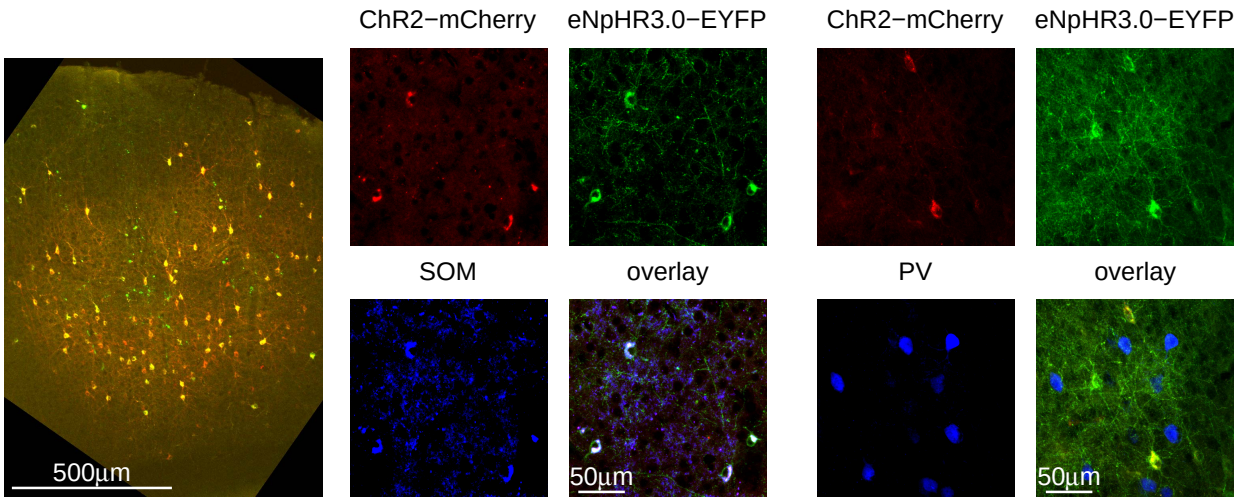

Figure 1. Cell-type-specific expression of channel- and halorhodopsin

(a) Coronal section of SI of a mouse injected with viral vectors carrying ChR2-mCherry (red channel) and eNpHR3.0-EYFP (green channel) showing expression throughout all cortical layers and extensive double infection. (b) Virus expression is specific to somatostatin-expressing neurons as evident from the overlap of mCherry and EYFP with somatostatin immunolabeling. (c) Virus expression is not overlapping with parvalbumin-expressing neurons as evident from the lack of overlap of mCherry and EYFP with parvalbumin immunolabeling.

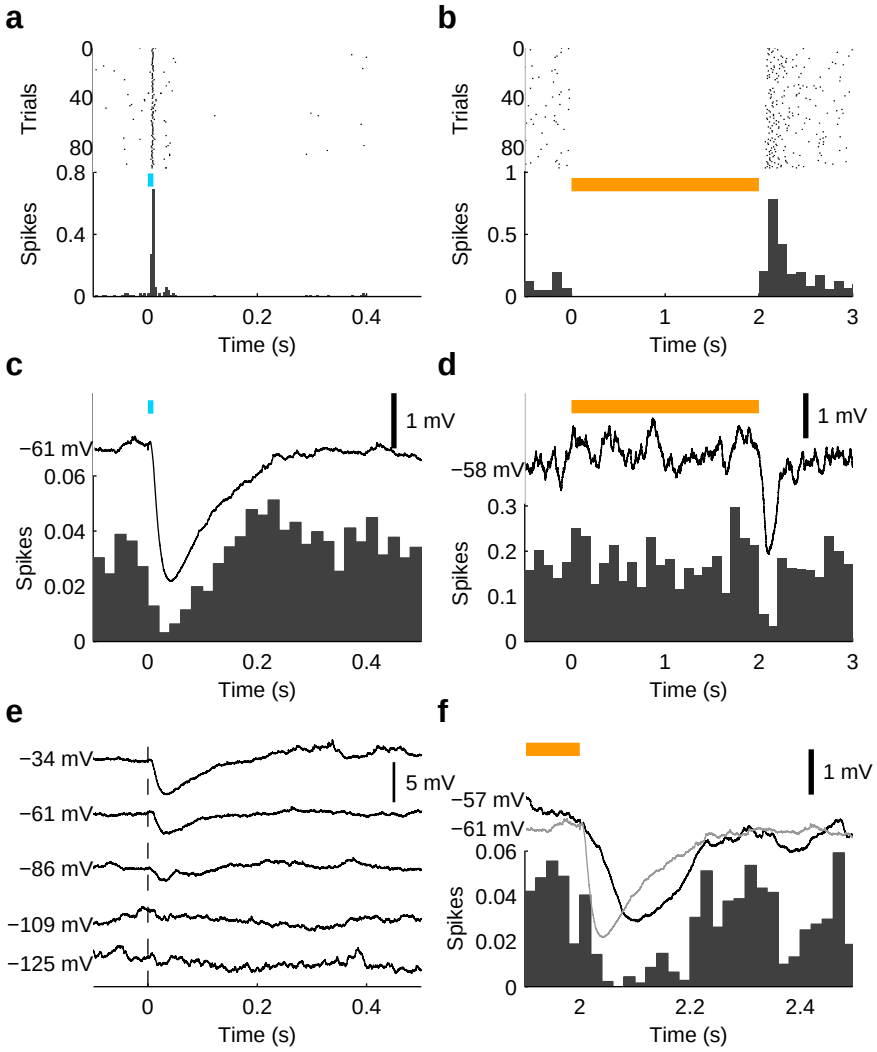

Figure 2. Bidirectional control of SOM neurons and impact on spontaneous pyramidal cell activity.

(a) Reliable firing of an example SOM cell in response to 10ms blue light pulses. (b) Robust silencing of an example SOM cell in response to sustained orange light stimulation. (c) Light-evoked IPSP and corresponding suppression of spontaneous layer 5 pyramidal cell activity. (d) Response to light-driven inactivation of SOM cells showing a rebound IPSP after light offset and corresponding suppression of spontaneous layer 5 pyramidal cell activity. (e) Effect of current injections on light-evoked IPSP in an example pyramidal cell. (f) Higher resolution comparison of rebound IPSP (black) with corresponding spiking suppression and light-evoked IPSP (gray).

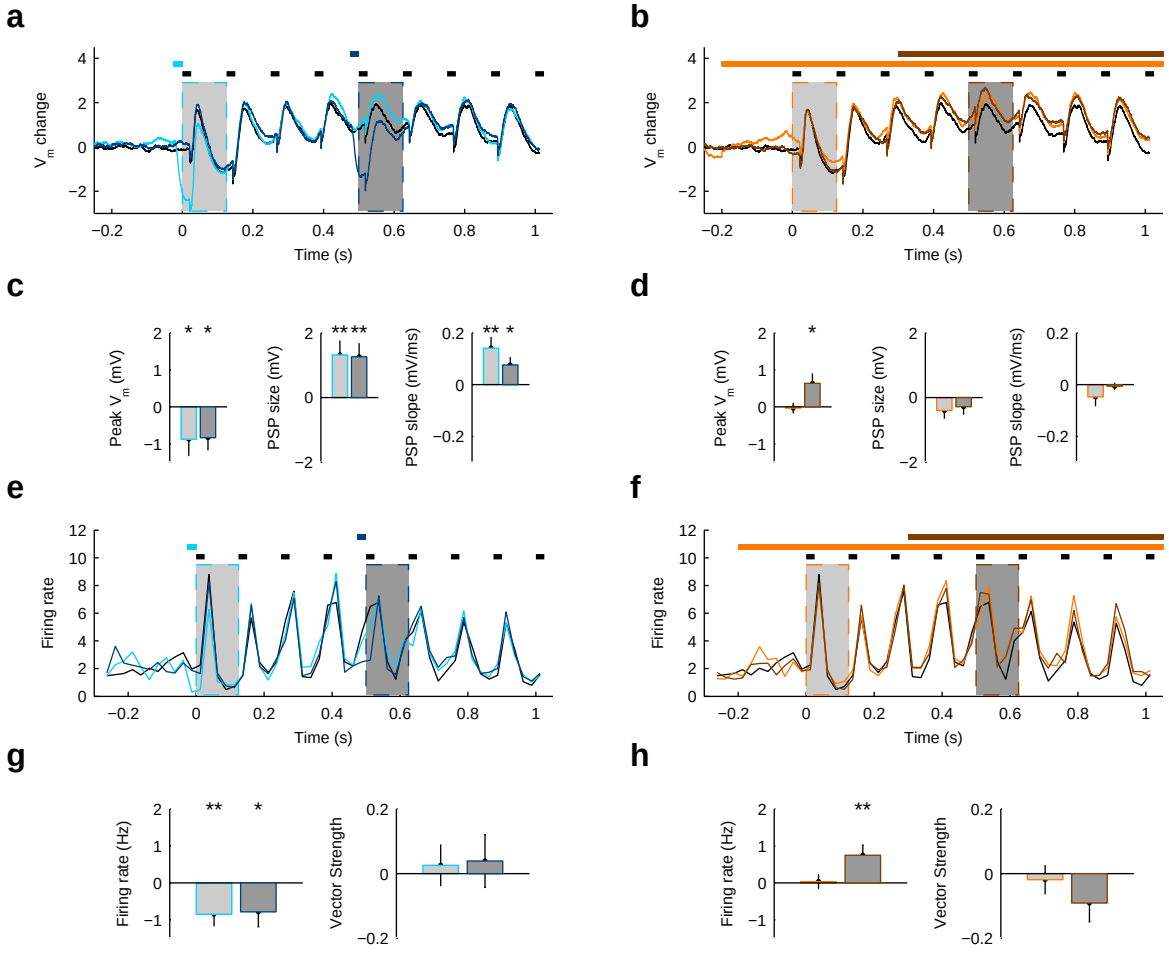

Figure 3. Differential impact of SOM cell activation and inactivation during early and late sensory stimuli.

(a) Average membrane potential time course during early (light blue) and late (dark blue) SOM activation in comparison to baseline (no light) condition (black). Timing of light and vibrissa stimulation is indicated by bars at the top. (c) Comparison of the impact of early and late activation on subthreshold measures. (e) Instantaneous firing rates during early (light blue) and late (dark blue) SOM activation in comparison to baseline (no light) condition (black). (g) Comparison of the impact of early and late activation on spiking measures. (b,d,f,h) Same as (a,c,e,g), but for inactivation. Asterisks denote $p < 0.05$, $p < 0.01$; error bars are mean ± SEM.

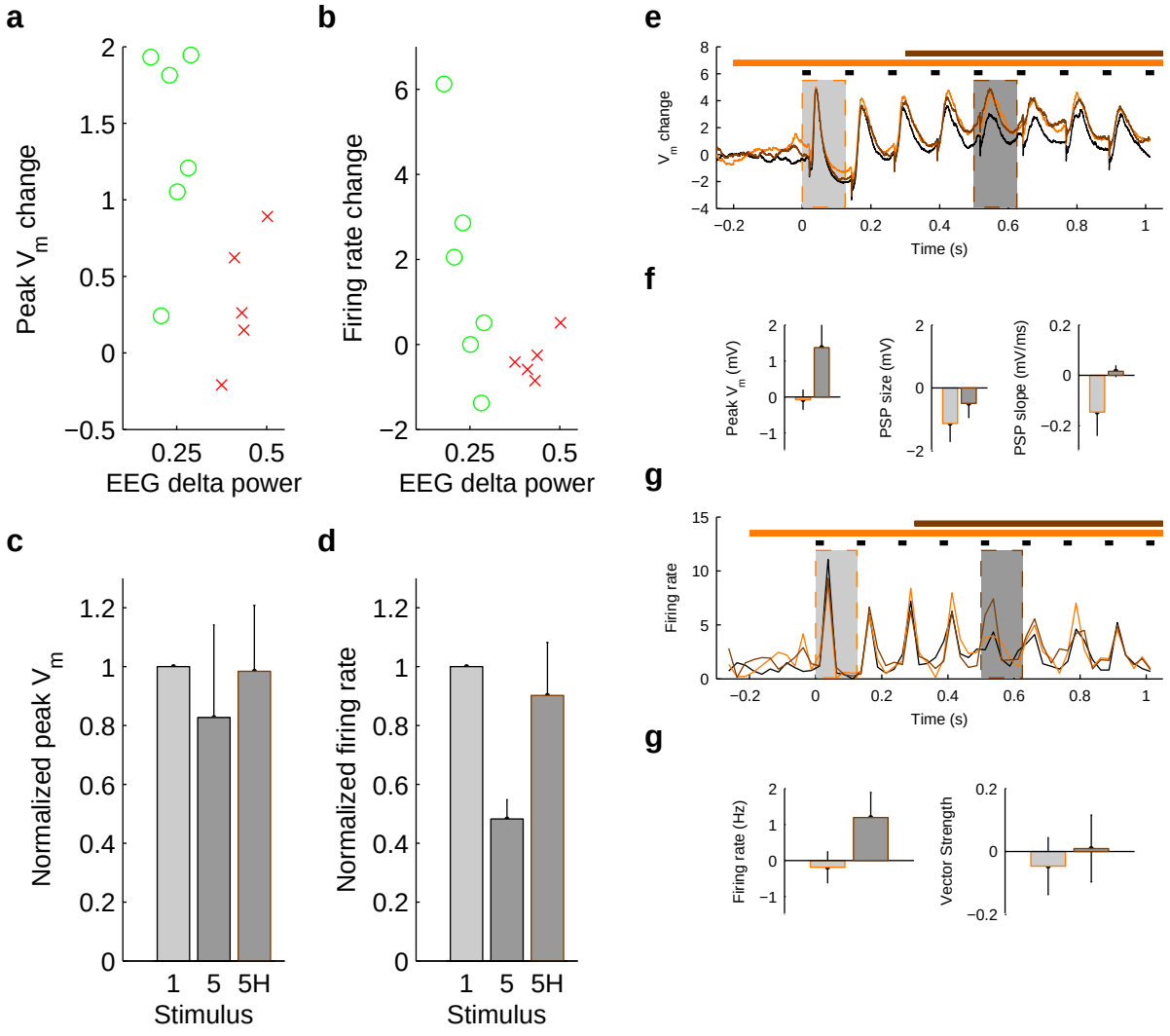

Figure 4. Impact of anesthesia depth on SOM cell inactivation.

(a) Relationship between anesthesia depth and magnitude of membrane potential change during late inactivation. (b) Same as (a), but for firing rate. (c) Effect of late inactivation during light anesthesia on the normalized peak membrane potential. (d) Same as (c), but for firing rate. (e-h) Same as Figure 3 (b,d,f,h), but only for the subset of runs during light anesthesia. Asterisks denote $p < 0.05$, $p < 0.01$; error bars are mean ± SEM.

Chapter 5:

Conclusion

In the previous chapters, I have presented correlational, causal and computational studies investigating the contribution of distinct interneuron types to neocortical dynamics on different timescales.

In chapter 2, we employed optogenetics in combination with intra- and extracellular electrophysiology to provide the first causal test of the involvement of parvalbumin-expressing interneurons in the generation of gamma oscillations *in vivo*. While there had been a number of *in vitro* and *in silico* studies on the generation of gamma, the necessary techniques had not been available to perform a conclusive study *in vivo* until the advent of optogenetics. By providing the possibility to target reversible activation on the time scale of milliseconds to a particular subset of neurons defined by their molecular properties, this new manipulation technique enables the manipulation of intact neural circuits without the need for genetic manipulations fundamentally altering the circuit that is under investigation. The ability to control activity on a millisecond time scale is particularly crucial for phenomena like gamma oscillations, which are intrinsically dynamic on the same time scale. Despite this powerful advance, results from optogenetic activation need to be interpreted carefully. While activation can be cell-type specific, it is not layer-specific when using bulk virus injections, necessitating a careful interpretation since its impact on (sensory) processing difficult since the evoked activity could have different effects across cortical layers. In addition, optogenetic activation acts on all cells expressing the opsin, not respecting the patterns of activity within a population on a cellular level. For example, a sensory stimulus often only strongly activate a small set of neurons that is tuned to the particular stimulus, while the whole population is activated by optogenetics, leading to a very different pattern of activity in the population. Furthermore, neurons often express correlations in their overall activity and their precise timing, both of which are most likely lost during optogenetic stimulation. In summary, while the advent of optogenetics signifies a prominent advance in technology, caution has to be exercised in the interpretation of the generated data.

In chapter 3, we augmented the *in vivo* data with *in silico* experiments. Despite the advances in recording techniques, it is still almost impossible to record intracellularly from more than one cell *in vivo*. Extracellular recordings employing arrays of electrodes can increase the number of recorded cells, but to understand the mechanism behind most neural phenomena, it is necessary to have information about their subthreshold activity. Because of the low yield associated with intracellular recordings *in vivo*, it would be helpful to enrich these small datasets with

information from other sources. Intracellular recordings *in vitro* can be helpful, however there are concerns about the imposed changes in network connectivity. During slicing, a large fraction of axons and dendrites are severed, leading to radical changes in conditions on a cellular and network level, including but not limited to a marked decrease in spontaneous activity. For a long time, the lack of sufficient computing power has precluded computational studies with a level of detail and size necessary to truly augment experimental data. Using general purpose graphics processing units (GPGPUs), we can now simulate networks with thousands of cells described by Hodgkin-Huxley dynamics and hundreds of thousands of detailed dynamic synapses less than 20 times slower than real-time, i.e. simulating one second of data takes less than 20 seconds to run. This represents an 80-100-fold increase in speed over traditional simulations run on a single CPU. Compared to intracellular *in vivo* recordings, we can generate data roughly 360 times faster. While this comparison is by definition flawed, running a model for one day compares favorably to running experiments for a year (and performing 10 intracellular *in vivo* recordings every day). Obviously, the caveat of any modeling study applies, in that the results from these simulations should only be viewed as predictions until they have been confirmed *in vivo*. However, *in silico* experiments not only provide a useful way to test several hypothesis for consistency quickly and help us formulate focused predictions that can then be more easily and rapidly tested *in vivo*, they also enable us to investigate more elusive concepts, such as synchrony, which are inherently impossible to study with single-cell recordings, and derive predictions that can actually be tested. In summary, rapid large-scale biophysically detailed *in silico* experiments provide the ability for high-throughput hypothesis testing and creation of focused testable predictions and thus help to utilize laborious *in vivo* recordings in an optimally efficient manner.

In chapter 4, we combined optogenetics with intra- and extracellular recordings again to investigate neural dynamics an order of magnitude slower than gamma oscillations. While the current opinion in the field largely dismissed the role of interneurons in sensory adaptation, recent *in vitro* evidence supported the hypothesis of a significant contribution from a distinct class of interneurons. Similar to the case of gamma oscillations, previous *in vitro* and *in vivo* studies had been correlative in nature, and the disregard for an interneuronal contribution likely arose from a combination of methodological and interpretative weaknesses. Interestingly, though, optogenetic activation would not be sufficient for a truly causal investigation of the role

of these neurons in this phenomenon. Artificially activating somatostatin-expressing interneurons provides information about what the impact of these cells on other cells, and thus sensory processing, potentially could be, but not necessarily what it actually is. To conclusively test their involvement in "normal" processing, the effects of their inactivation also need to be observed. Using halorhodopsin enables exactly the highly specific and temporally precise and reversible inactivation that is needed for such an endeavor, providing insight into the role of the studied circuit element by disabling it under different conditions. Because it does not indiscriminably activate cells, this method does not suffer from the artificiality problem encountered in optogenetic activation studies. However, the lack of laminar specificity requires careful interpretation of results obtained through inactivation, as well. In general, optogenetic manipulations constitute a significant technological advance, but careful interpretation of the results and further developments enabling the investigation and manipulation of a subset of cells based on their functional connectivity are necessary.

We have investigated two examples of neocortical dynamics operating on different time scales, showing that distinct interneuron types contribute to these different processes. Both gamma oscillations and adaptation are ubiquitous phenomena in neocortex and thus likely provide insight into the architecture and function of the canonical microcircuit, a general circuit motif that is replicated across neocortex. A microcircuit combining fast inhibition to enhance selectivity and slower inhibition to provide invariance by maintaining an optimal operating regime could be a powerful generic processing unit that can adapt to the statistics of its input, however a lot of work remains to be done to test this hypothesis and fully understand how sensory processing is similar and different across modalities.